

Novel oxide buffer approach for GaN integration on Si(111) platform through $\text{Sc}_2\text{O}_3/\text{Y}_2\text{O}_3$ bi-layer

Von der Fakultät für Mathematik, Naturwissenschaften und Informatik
der Brandenburgischen Technischen Universität Cottbus

zur Erlangung des akademischen Grades

Doktor der Naturwissenschaften
(Dr. rer. nat.)

genehmigte Dissertation

vorgelegt von

Master of Science Engineer

Lidia Tarnawska

geboren am 08. Mai 1985 in Wroclaw (Polen)

Gutachter: Prof. Dr. rer. nat. habil. Thomas Schroeder

Gutachter: Prof. Dr. ing. habil. Regina Paszkiewicz

Gutachter: Prof. Dr. Michael Lehmann

Tag der mündlichen Prüfung: 19. Dezember 2012

Acknowledgements

I would like to acknowledge the many people whose support made this thesis possible.

It is a pleasure to thank my supervisor Prof. Thomas Schroeder for continuous support, for his time and patient help in developing my research skills and knowledge.

I would like to express my deepest gratitude to Prof. Regina Paszkiewicz and Prof. Michael Lehmann for sharing their experience and creative discussions. I am also grateful to Dr. Peter Storck and Siltronic AG for financing the heteroepitaxy project I was involved in.

I would like to thank Dr. Peter Zaumseil for introducing me to the world of x-ray diffraction experiments, for his guidance and patient help; Hans Thieme for his support with molecular beam epitaxy; Dr. Markus Andreas Schubert for transmission electron microscopy measurements; Mrs. Gabriele Morgenstern for scanning electron microscopy characterization, Prof. Burkhard Dietrich for Raman measurements and fruitful discussions and Dr. Jarek Dabrowski for his theoretical calculations. Ab-initio atomistic calculations have been performed on JUROPA supercomputer in the Jülich Supercomputing Centre. Computing time has been granted by the John von Neumann-Institute for Computing, project hfo06 "Modeling of Nucleation and Growth Processes for Silicon-Compatible Microelectronics".

Many thanks to Dr. Grzegorz Lupina, Dr. Grzegorz Kozlowski, Dawid Kot, Gosia Sowinska, Oliver Skibitzki, Marvin Zöllner, Dr. Gunther Lippert, Dr. Christian Wenger, Dr. Christian Walczyk, Damian Walczyk, Canan Baristran Kaynak, Dr. Mindaugas Lukosius, Dr. Thomas Bertaud, Udo Kaletta, Dr. Gang Niu, Dr. Piotr Dudek and Yvonne Heier for their personal and scientific support, friendly atmosphere, and for being always open to listen and to help. Special thanks go to Dr. Alessandro Giussani, who has worked with me in the heteroepitaxy project during his PhD thesis at IHP.

I am also very indebted to the colleagues from the Wrocław University of Technology, namely, Dr. Mateusz Wosko, Dr. Adam Szyzka, Dr. Bogdan Paszkiewicz and Kornelia Indykiewicz for the collaboration on MOCVD GaN

growth and characterization; to Serdal Okur, Dr. Ümit Özgür and Prof. Hadis Morkoç from Virginia Commonwealth University for introduction to the photoluminescence and their kind help in the measurements; to Daniela Zengler from Technische Universität Berlin for sample characterization by transmission electron microscopy.

I thank my family and Grzegorz for all support at each step, for their love and patience that I have put to test during those years.

Abstract

Motivation: Preparation of GaN virtual substrates on large-scale Si wafers is intensively pursued as a cost-effective approach for high power/high frequency electronics (HEMT's etc.) and optoelectronic applications (LED, LASER). However, the growth of high quality GaN layers on Si is hampered by several difficulties mainly related to a large lattice mismatch (-17%) and a huge difference in the thermal expansion coefficient (56%). As a consequence, GaN epitaxial layers grown on Si substrates show a high number of defects (threading dislocations etc.), which severely deteriorate the overall quality of the GaN films. Additionally, due to the different thermal expansion coefficients of the substrate and the film, μm -thick GaN layers crack during post-growth cooling. To solve these integration problems, different semiconducting (e.g. AlN, GaAs, ZnO, HfN) and insulating (e.g. Al_2O_3 , MgO, LiGaO_2) buffer layers, separating the Si substrate from the GaN film, are applied.

Goal: In this thesis, a novel buffer approach for the integration of GaN on Si is proposed and investigated. The new approach employs $\text{Sc}_2\text{O}_3/\text{Y}_2\text{O}_3$ bi-layer templates as a step-graded buffer to reduce the lattice mismatch between GaN and the Si(111) substrate. According to the bulk crystal lattices, since the Y_2O_3 has an in-plane lattice misfit of -2% to Si, Sc_2O_3 -7% to Y_2O_3 , the lattice misfit between GaN and the substrate can be theoretically reduced by about 50% from -17% (GaN/Si) to -8% (GaN/ Sc_2O_3).

Experimental: The GaN/ $\text{Sc}_2\text{O}_3/\text{Y}_2\text{O}_3/\text{Si}(111)$ heterostructures are prepared in a multichamber molecular beam epitaxy system on 4 inch Si(111) wafers. In order to obtain complete information on the structural quality of the oxide buffer as well as the GaN layer, synchrotron- and laboratory-based x-ray diffraction, transmission electron microscopy and photoluminescence measurements are performed. The topography of the films is characterized by scanning electron microscopy and chemical interdiffusion is investigated by energy-dispersive x-ray spectroscopy. The nucleation processes of the GaN on Sc_2O_3 buffer are followed in-situ by reflection high energy electron diffraction and the interface chemistry is analyzed by means of x-ray photoelectron spectroscopy.

Results: It is found, that the $\text{Sc}_2\text{O}_3/\text{Y}_2\text{O}_3$ buffer approach provides a template of high structural quality for GaN overgrowth. The bi-layer buffer plays a lattice match mediator role between GaN and Si and acts as a barrier against impurity diffusion. GaN grown on $\text{Sc}_2\text{O}_3/\text{Y}_2\text{O}_3/\text{Si}(111)$ templates is single crystalline with a wurtzite structure and (0001) oriented. Due to the -8%

lattice mismatch between GaN and Sc_2O_3 , GaN growth proceeds by the nucleation of 3D islands. The size of the islands, coalescence time and the relaxation process depend on the GaN growth conditions and have a strong influence on the topography of closed layers, crystalline quality (defect density) as well as optical properties. The best GaN material parameters are obtained for the layers grown in Ga-rich regime when the Ga/N ratio is slightly higher than unity. The main three defects found in the μm -thick GaN layers are a) threading dislocation, with density in the order of 10^{10} cm^{-2} , b) stacking faults, resulting in cubic inclusions in the hexagonal matrix and c) inversion domain boundaries causing Ga-polar regions in the mainly N-polar film. A theoretical GaN/ Sc_2O_3 interface model is discussed to explain these experimental findings.

Despite the relatively large number of structural defects, photoluminescence shows sharp and strong donor-bound exciton transition and very low intensity yellow emission, which indicate that GaN layers grown on $\text{Sc}_2\text{O}_3/\text{Y}_2\text{O}_3/\text{Si}(111)$ are promising for future optoelectronic applications.

Outlook: Future growth strategies will focus on interface engineering approach to further reduce the lattice mismatch between GaN(0001) and Sc_2O_3 (111) surfaces, enable growth of unipolar GaN films and trigger the occurrence of an early 2D-like growth mode to avoid cubic GaN inclusions and guarantee low threading dislocation densities.

Zusammenfassung

Motivation: Die Herstellung von virtuellen GaN-Substraten auf grossflächigen Siliziumscheiben wird intensiv als kostengünstige Lösung in der Hochleistung-/Hochfrequenz-Elektronik (HEMTs, usw.) und für optoelektronische Anwendungen (LED, LASER) verfolgt. Jedoch wird das Wachstum von qualitativ hochwertigen GaN-Schichten auf Silizium-Substraten durch mehrere Schwierigkeiten, hauptsächlich verbunden mit einer grossen Gitterfehlpassung (-17%) und einem grossen Unterschied in den thermischen Ausdehnungskoeffizienten (56%), behindert. Infolgedessen zeigen die auf Silizium epitaxial aufgewachsenen GaN-Schichten eine hohe Anzahl an Defekten (Schraubenversetzungen, usw.), welche die Gesamtqualität der GaN-Filme stark verschlechtern. Zusätzlich entstehen auf Grund der unterschiedlichen thermischen Ausdehnungskoeffizienten des Substrats und des Films bei μm -dicken GaN Schichten Brüche während des Kühlens nach dem Wachstum. Um diese Integrationsprobleme zu lösen, werden unterschiedliche halbleitende (z.B. AlN, GaAs, ZnO, HfN) und isolierende (z.B. Al_2O_3 , MgO, LiGaO_2) Pufferschichten, welche das Siliziumsubstrat von der GaN-Schicht trennen, verwendet.

Ziel: In dieser Doktorarbeit wird ein neuartiger Pufferansatz für die Integration von GaN auf Silizium vorgeschlagen und untersucht. Der neue Ansatz beruht auf dem $\text{Sc}_2\text{O}_3/\text{Y}_2\text{O}_3$ -Zweischicht-System, das als gestufter Pufferansatz die Gitterfehlpassung zwischen GaN und Si(111) verringert. Gemäss den Kristallvolumengittern, wonach Y_2O_3 eine Gitterfehlpassung in der Ebene von -2% zu Silizium und Sc_2O_3 eine von -7% zu Y_2O_3 besitzt, kann theoretisch die Gitterfehlpassung zwischen dem Substrat und GaN um 50% von -17% (GaN/Si) auf -8% (GaN/ Sc_2O_3) reduziert werden.

Experimenteller Teil: Die GaN/ $\text{Sc}_2\text{O}_3/\text{Y}_2\text{O}_3/\text{Si}(111)$ -Heterostrukturen wurden in einer Mehrkammer-Molekularstrahlepitaxieanlage auf 4 Inch Si(111) Scheiben erstellt. Um vollständige Informationen über die strukturelle Qualität des Oxidpuffers sowie der GaN-Schicht zu erhalten, wurden Synchrotron- und Labor-basierte Röntgenbeugung, Transmissionselektronenmikroskopie und Photolumineszenzuntersuchungen durchgeführt. Die Topografie der Filme ist mittels Rasterelektronenmikroskopie charakterisiert und die chemische Interdiffusion ist durch Energiedispersive Röntgenspektroskopie untersucht worden. Die Keimbildungsprozesse von GaN auf dem Sc_2O_3 -Puffer sind in-situ durch Beugung hochenergetischer Elektronen in Reflektionsgeometrie und die Grenzflächenchemie ist mittels Röntgen-Photoelektronen-Spektroskopie analysiert worden.

Ergebnisse: Es wurde festgestellt, dass der $\text{Sc}_2\text{O}_3/\text{Y}_2\text{O}_3$ - Pufferansatz eine Vorlage mit hoher struktureller Qualität für das Aufwachsen von GaN bietet. Der zweischichtige Puffer spielt für Gitteranpassung zwischen GaN und Silizium eine Vermittlerrolle und wirkt als Barriere gegen die Diffusion von Verunreinigungen. GaN, gewachsen auf der $\text{Sc}_2\text{O}_3/\text{Y}_2\text{O}_3/\text{Si}(111)$ -Vorlage, ist einkristallin und besitzt eine (0001) orientierte Wurtzit-Struktur. Aufgrund der -8% Gitterfehlpassung zwischen GaN und Sc_2O_3 verläuft das Wachstum von GaN über die Keimbildung von dreidimensionalen Inseln. Die Grösse der Inseln, die Koaleszenzzeit und der Relaxationsprozess sind abhängig von den GaN Wachstumsbedingungen und haben starken Einfluss auf die Topographie der geschlossenen Schichten, auf die Kristallqualität (Defektdichte) ebenso wie auf die optischen Eigenschaften. Die besten Materialparameter für GaN sind im Ga-reichen Regime erzielt worden, wenn das Ga/N-Verhältnis geringfügig höher als eins ist. Die drei Hauptdefektarten, welche in den μm -dicken GaN-Schichten gefunden wurden, sind a) Schraubenversetzungen mit einer Dichte in der Grössenordnung von 10^{10} cm^{-2} , b) Stapelfehler, wodurch kubische Einschlüsse in der hexagonalen Matrix resultieren, und c) Inversionsdomänengrenzen, welche Ga-polare Regionen im hauptsächlich N-polaren Film verursachen. Ein theoretisches GaN/ Sc_2O_3 -Grenzflächenmodell wird diskutiert, um diese experimentellen Ergebnisse zu erklären. Trotz der relativ grossen Anzahl von strukturellen Defekten zeigt die Photolumineszenz einen scharfen und starken Donor-gebundenen Excitonübergang und eine sehr geringe Intensität an gelber Emission, was aufzeigt, dass GaN-Schichten, aufgewachsen auf $\text{Sc}_2\text{O}_3/\text{Y}_2\text{O}_3/\text{Si}(111)$, vielversprechend für zukünftige optoelektronische Anwendungen sind.

Ausblick: Zukünftige Wachstumsstrategien werden sich auf den Grenzflächenanpassungsansatz fokussieren, um die Gitterfehlpassung zwischen GaN (0001) und $\text{Sc}_2\text{O}_3(111)$ weiter zu verringern, was das Einsetzen eines frühen zweidimensionalen Wachstumsmodus auslöst, wodurch kubische GaN- Einschlüsse vermieden und geringe Schraubenversetzungsdichten garantiert werden können. Ferner muss die Massgeschneiderte Grenzfläche das Wachstum von unipolaren GaN bewirken, so dass Inversionsdomänengrenzen vollkommen unterdrückt werden.

Contents

1	Introduction	1
1.1	Fundamentals of GaN	1
1.1.1	GaN crystal structure and material properties	1
1.1.2	GaN applications	3
1.2	Bulk GaN	9
1.3	GaN integration on Si substrates	10
1.3.1	Choice of Si wafer orientation	12
1.3.2	Buffer layer technology - strain engineering	13
1.3.3	Selective area growth	17
1.4	Purpose of this thesis	19
1.4.1	IHP-Siltronic approach and goal of this study	19
1.4.2	Organisation of the thesis	22
2	Experimental background	23
2.1	Substrate preparation and layer growth	23
2.1.1	Substrate cleaning	23
2.1.2	Molecular Beam Epitaxy	24
2.2	Characterization techniques	31
2.2.1	X-ray diffraction	31
2.2.2	X-ray reflectivity	39
2.2.3	Reflection High Energy Electron Diffraction	41
2.2.4	X-ray Photoelectron Spectroscopy	43
2.2.5	Scanning Electron Microscopy	45
2.2.6	Transmission Electron Microscopy	46
2.2.7	Photoluminescence	47
3	Results	49
3.1	Growth characteristics of the oxide buffer	49
3.1.1	<i>In-situ</i> RHEED study	49

3.1.2	Crystalline properties	51
3.1.3	Strain state of the oxide bi-layer	54
3.1.4	Defect structure	56
3.1.5	Summary	58
3.2	Thin GaN on Sc ₂ O ₃ /Y ₂ O ₃ / buffer on Si(111)	59
3.2.1	Layer morphology and epitaxial relationship	59
3.2.2	Crystalline quality	62
3.2.3	Summary	67
3.3	Thick GaN on Sc ₂ O ₃ /Y ₂ O ₃ buffer on Si(111)	68
3.3.1	GaN growth diagram	68
3.3.2	Crystalline quality of μm - thick GaN films prepared un- der Ga-rich and N-rich conditions	71
3.3.3	Optical properties	78
3.3.4	Strain components in thick GaN layers	79
3.3.5	Summary	80
3.4	GaN/Sc ₂ O ₃ interface	82
3.4.1	Experimental results	82
3.4.2	Model of the GaN/Sc ₂ O ₃ interface	90
3.4.3	Discussion of the growth process	97
3.4.4	Summary	99
4	Summary and Outlook	101
4.1	Summary	101
4.1.1	Growth characteristics of Sc ₂ O ₃ /Y ₂ O ₃ buffers	103
4.1.2	GaN growth mechanism on Sc ₂ O ₃ /Y ₂ O ₃ buffers	103
4.1.3	Properties of μm -thick GaN on Sc ₂ O ₃ /Y ₂ O ₃ buffers	105
4.2	Outlook	107
4.2.1	Next MBE experiments	107
4.2.2	Future MOCVD experiments	110
5	Scientific visibility	112
5.1	Publications in peer-reviewed journals	112
5.2	Presentations at conferences	113
	Bibliography	113

Chapter 1

Introduction

1.1 Fundamentals of GaN

1.1.1 GaN crystal structure and material properties

Gallium Nitride (GaN) can crystallize¹ under ambient conditions either in a metastable zinc blende (ZB) or in a thermodynamically stable wurtzite (WZ) structure.² ZB has a cubic unit cell (space group $F\bar{4}3$) with a lattice constant a of 4.52 Å whereas the WZ structure has a hexagonal unit cell (space group $P6_3mc$) and thus two lattice constants: $c=5.1851$ Å and $a=3.1893$ Å. The difference between the ZB and WZ structures is only the stacking sequence. As shown in Fig. 1.1 the WZ structure has AaBbAaBbAaBb... stacking sequence along the $[0001]$ axis, while the ZB structure has AaBbCcAaBbCc... stacking sequence along the $[111]$ axis, where A(a), B(b), and C(c) denote three kinds of cation (anion) positions in the triangular lattice on the (0001) and (111) planes. Both, WZ and ZB structures have polar axes (lack of inversion symmetry). Therefore, a GaN surface has either Ga-polarity (Ga face up) or N-polarity (N face up).^{3,4} Bulk and surface properties depend significantly on whether the surface is terminated by N or Ga atoms. For example, the growth of Ga-face GaN has been found to be preferable for most device applications, since it usually promotes a two-dimensional growth mode with atomically smooth surfaces.⁵

A characteristic feature of semiconductors with the WZ structure is the existence of a nonzero volume electric dipole moment in the crystal, when there is no external strain or electric field, which results in spontaneous polarization in the materials (e.g. spontaneous polarization for Ga-face GaN is always neg-

¹The rock salt structure of GaN can not be produced by any epitaxial growth. It can be induced in III-nitrides under very high pressure¹

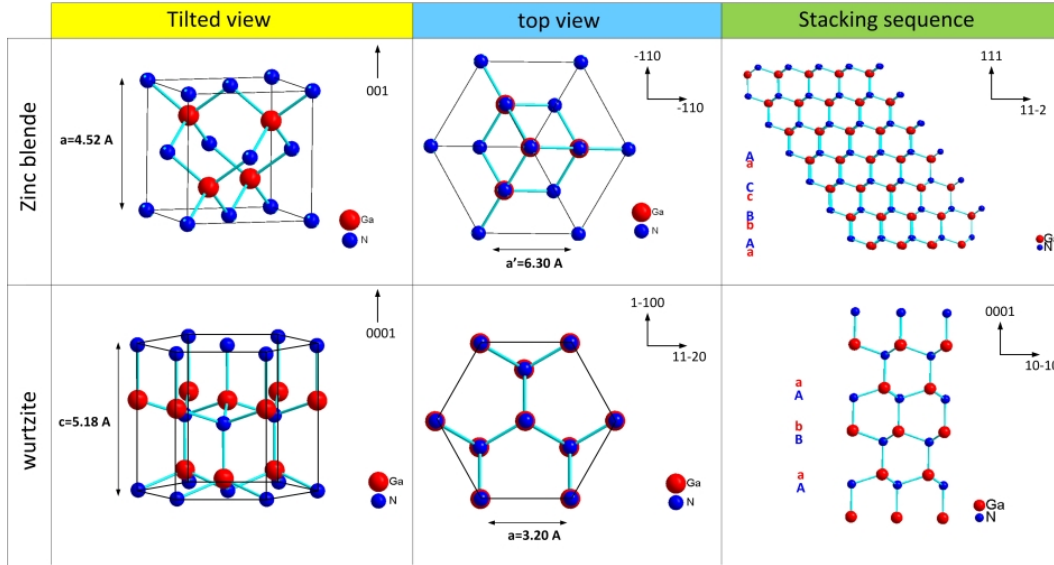


Figure 1.1: Wurtzite and zinc blende crystal structure of GaN: tilted, top view [along WZ-GaN(0001) and ZB-GaN(111)], and stacking sequence [along WZ-GaN($\bar{1}210$) and ZB-GaN($\bar{1}10$)].

ative i.e. directed toward the substrate). Spontaneous polarization can exist in a crystal which exhibits:

- non-centro-symmetric nature
- polar bonds
- lower than ideal c/a ratio (in case of GaN the c/a : ideal = 1.633, experimental = 1.626)

Furthermore, there is a nonzero piezoelectric module when the WZ GaN is stressed along (0001) direction, resulting in piezoelectric effects. These piezoelectric effects and the difference in spontaneous polarization between e.g. AlGaIn and GaN cause polarization charges and fields which are used in the AlGaIn/GaN- based High-electron-mobility transistor (HEMT).⁶ However, such electric fields have also a negative aspect. They produce a strong Quantum-Confined Stark Effect, modifying the electron and hole recombination dynamics and decreasing the radiative recombination rate in the GaN-based light emitting diodes.⁷

Physical properties of GaN make it an attractive semiconductor material for many electronic and optoelectronic applications.^{8,9} The most important physical characteristic of GaN are summarized in Tab. 1.1. Wide, direct energy

band gap of GaN makes this material suitable for short wavelength emitters such as light emitting diodes or laser diodes and detectors. Moreover, GaN forms solid solutions with aluminum nitride (AlN) and indium nitride (InN), enabling a wide range (0.8-6.2 eV) of energy band gaps (Fig. 1.2 a)). The large energy band gap of GaN also results in high electric breakdown fields, which enable the application of high supply voltages. Furthermore, it allows the material to withstand high operating temperatures. Another important advantage of GaN is its high thermal conductivity, that makes it a good choice for the realization of high power devices. Chemical stability of GaN at elevated temperatures combined with its hardness makes GaN an attractive material for protective coatings. On the other hand, chemical stability of GaN presents a technological challenge, since the conventional wet etching techniques used in semiconductor processing are not suitable for GaN device fabrication.

1.1.2 GaN applications

Optoelectronics

Light-emitting diodes (LEDs)

LEDs are p-n junction devices constructed using direct band gap semiconductors which convert electrical power to optical power when biased in the forward direction. They produce light through spontaneous emission of radiation whose wavelength is determined by the band gap of the semiconductor across which the carrier recombination takes place (Fig. 1.2 b)). A modern GaN-based LED

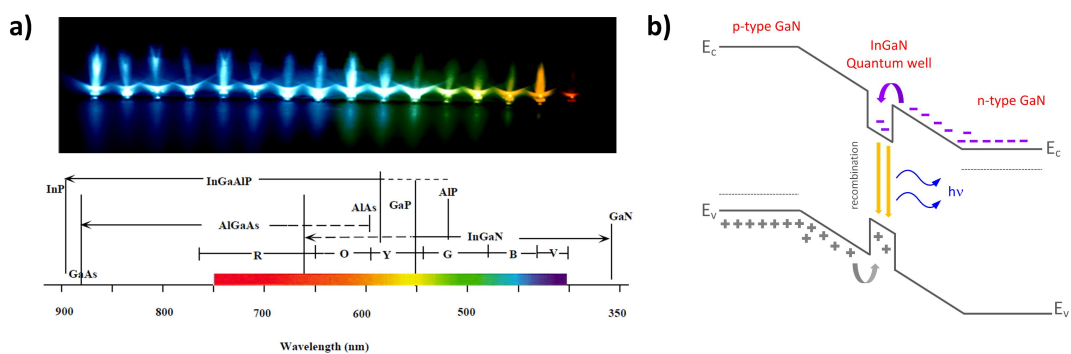


Figure 1.2: a) The LED materials and range of wavelength of the emission associated with them (Figure adapted from Ref. 15) b) Schematic band diagram of the GaN-based LED with one InGaN quantum well towards forward bias. The transformation of the electric power into light takes place in the thin active region (quantum well).

Table 1.1: Properties of GaN and AlN and the most common substrates for III-N epitaxy: Si, Al₂O₃, and SiC [Ref. 10].

Properties	Si		6H-SiC		Al ₂ O ₃		AlN		GaN	
	diamond	wurtzite	rhombohedral	wurtzite	wurtzite	wurtzite	cubic			
Crystal structure	diamond	wurtzite	rhombohedral	wurtzite	wurtzite	wurtzite	cubic			
Lattice constant [Å]	a=5.431	a=3.0806 c=10.053	a=4.765 c=12.98	a=3.11 c=4.979	a=3.189 c=5.185	a=4.52				
Band gap energy [eV]	1.12 indirect	3.0 indirect	8.8 indirect	6.2 direct	3.44 direct	3.30 direct				
Thermal expansion coefficient x10 ⁻⁶ [K ⁻¹]	$\alpha_a=2.616$	$\alpha_a=4.46$ $\alpha_c=4.16$	$\alpha_a=5.0$ $\alpha_c=9.03$	$\alpha_a=4.2$ $\alpha_c=5.3$	$\alpha_a=5.59$ $\alpha_c=3.2$	$\alpha_a=4.78$				
Thermal conductivity [W/cmK]	1.5	4.5	0.32	2.6	1.5	1.5				
Breakdown field 10 ⁶ [Vcm ⁻¹]	~ 0.3	~ 3	~ 10	~ 2	~ 5	~ 5				
Hole mobility [cm ² V ⁻¹ s ⁻¹]	450	90	20	14	200	350				
Electron mobility [cm ² V ⁻¹ s ⁻¹]	1500	400	380	300	1000	1000				
Maximum wafer size [inch]	12 [Ref.11]	2 [Ref.12]	10 [Ref.13]	2	2 [Ref.14]					

usually employs: one or more InGaN quantum well active region, with GaN cladding layers (Mg-doped p-GaN and Si-doped n-GaN region) usually grown on sapphire substrate.^{16,15}

A major limitation in the production of GaN-based LED on Si substrates is absorption of light emitted from the active region by the Si wafer. A potential solution for this problem is the insertion of high-reflectance distributed Bragg reflectors (DBR) between the substrate and the active region. This should increase light extraction by approximately a factor of two, thereby doubling luminous efficiency.^{17,18,19}

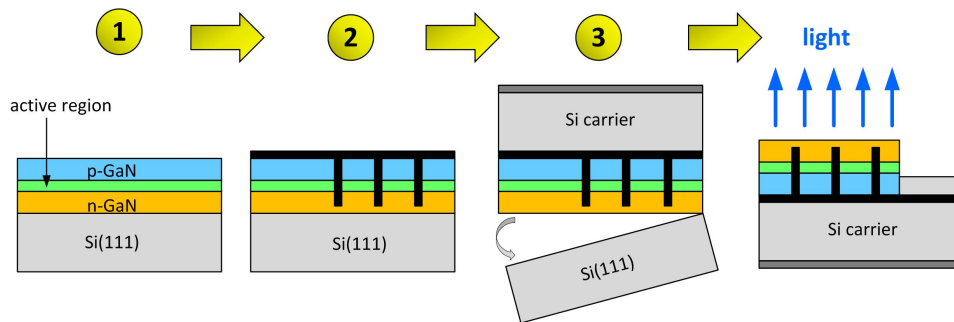


Figure 1.3: Fabrication process of GaN-based LED chips on Si wafers established by Osram Semiconductors Company.²⁰

An alternative approach was recently proposed by Osram Semiconductors GmbH. In this strategy the Si substrate which would otherwise absorb the emitted light, is removed after the growth of the LED structure.²⁰ The GaN-on-Si chips are fabricated using Osram's thin film UX:3 process, which involves (Fig. 1.3):

1. Growth of GaN epilayers on Si substrate
2. Mirror and contact formation
3. Transfer to Si carrier and substrate removal and
4. Final chip processing.

Using this technique and 6 inch Si substrates it is possible to fabricate 17.000 LED chips each with an area of 1 mm^2 on one wafer. The efficiency and brightness of these LEDs have already reached competitive market levels.

Among the major applications of LEDs are automotive exterior lighting, full color video displays, traffic signals, backlighting in e.g. cell phones and general room lighting.²¹

Laser diodes (LDs)

A LD is a laser where the active medium is a semiconductor similar to that found in a LED. However, to achieve gain and stimulated emission of radiation, the active region must be surrounded by an optical cavity.

LDs are already commercialized in optical disc data storage applications (HD-DVD and Blue-ray).^{22,23,24} In these applications, to enable larger storage density, the laser light has to be focused to a smaller size, which basically means a reduction in the wavelength of the laser. In consequence, the shorter wavelength of blue light (in comparison to red) enables realization of optical storage media with high data storage capacities. Other important GaN-based LD applications are: laser printing, projection displays, medical treatment (clinical diagnostic, treatment of skin conditions, sterilization), i-g-line microlithography and optical communication. For a comprehensive discussion of different LD architectures see for example Ref.15.

Photodetectors (PDs)

The p-n junction may also act as a PD and convert absorbed light into current. The principle of the photodetector is the photoelectric effect. When the energy of absorbed photons is large enough to rise the electrons to the conduction band from the valence band, holes in the valence band are left behind. In the photodetector, the electric field present, due to the built-in potential plus the applied voltage, separates electrons and holes causing current flow which is proportional to the photon flux.

The direct bandgap nitride semiconductors, ranging from 0.8-6.2 eV, are ideally suited for a large variety of detectors, especially in the ultraviolet (UV) range.²⁵ UV photodetection has drawn a great deal of attention in recent years, due to the rise of new requirements. Both civil and military industries demand better UV instrumentation, for applications such as engine control, solar UV radiation monitoring, UV astronomy, flame sensors, detection of missile plumes, and secure space-to-space communications. AlGaIn-based PDs are of high interest and their advantages include: high responsivity, low dark current, high bandwidth, and high detectivity. Moreover, wide-band gap materials are chemically, mechanically and thermally stable, which is an advantage. Beside p-n junction,²⁶ the possible structure types of photodetectors are: p-i-n,^{27,28} metal-semiconductor-metal (MSM)²⁹ and Schottky junction.^{15,30}

Table 1.2: Spontaneous (P_{sp}) polarization and piezoelectric constants (e_{33} and e_{31}) for III-V semiconductors. Piezoelectric polarization field is expressed as: $P_{pp}=e_{33}\epsilon_3+e_{31}(\epsilon_1+\epsilon_2)$, where $\epsilon_3=\frac{c-c_0}{c_0}$ and $\epsilon_1=\epsilon_2=\frac{a-a_0}{a_0}$

Material	$P_{sp}[\text{C}/\text{m}^2]$	$e_{33}[\text{C}/\text{m}^2]$	$e_{31}[\text{C}/\text{m}^2]$
GaN	-0.029	0.73	-0.49
AlN	-0.081	1.46	-0.60
InN	-0.032	0.97	-0.57
GaAs	-	-0.12	0.06
AlAs	-	-0.03	0.01

High power and high frequency electronics

The wide band gap, high break down fields, good transport properties and possibility to grow high quality heterostructures make the nitrides ideal candidates for high power and high temperature transistor applications. AlGaIn/GaN-based HEMT² has emerged as the most promising technology for microwave power amplification in satellite links and in base stations for wireless telecommunication applications.

The basis for HEMT operation is the two-dimensional electron gas (2 DEG) present at the AlGaIn/GaN interface formed due to existence of both spontaneous (P_{sp}) and a piezoelectric (P_{pp}) polarization field in both AlGaIn and GaN layers.^{6,31,32} Piezoelectric constant and P_{sp} increases from GaN to AlN (Tab. 1.2), so the total polarization of AlGaIn layer is larger than that of the GaN buffer film and therefore a positive polarization charge is present at the AlGaIn/GaN interface (for Ga-face structure). Electrons, which tend to compensate this positive charge, result in the formation of a 2 DEG in the triangular quantum well on the border of AlGaIn and GaN films (Fig. 1.4). The 2 DEG serves as a conductive channel in which electrons can move between source and drain electrodes at very high speed. The conductivity of this two dimensional channel is given by the equation:

$$\sigma = qn_s\mu \quad (1.1)$$

where q is the electron charge, n_s is the sheet carrier concentration of free electrons and μ is the mobility of the electrons. For the standard, undoped

²HEMT is also known as Modulation-Doped Field-Effect Transistor (MDFET), Two Dimensional Electron Gas FET (TEDFET), Selectively Doped Heterostructure Transistor (SDHT) or simply Heterojunction FET (HFET)

AlGa_N/Ga_N structure n_s values of about 10^{13} cm⁻² are achieved,³³ which is a factor of five greater than obtained in the AlGaAs/GaAs HEMT system.³⁴ High n_s value in combination with high μ (2000 cm²V⁻¹s⁻¹ at 300K) make GaN-based HEMT very attractive for high frequency switching applications. Beside the high frequency operation, the structure of GaN-based HEMT's allows also for achieving high output power, high linearity, and high efficiency.³⁵ Moreover, AlGa_N/Ga_N HEMT structures are widely used as a biosensor for

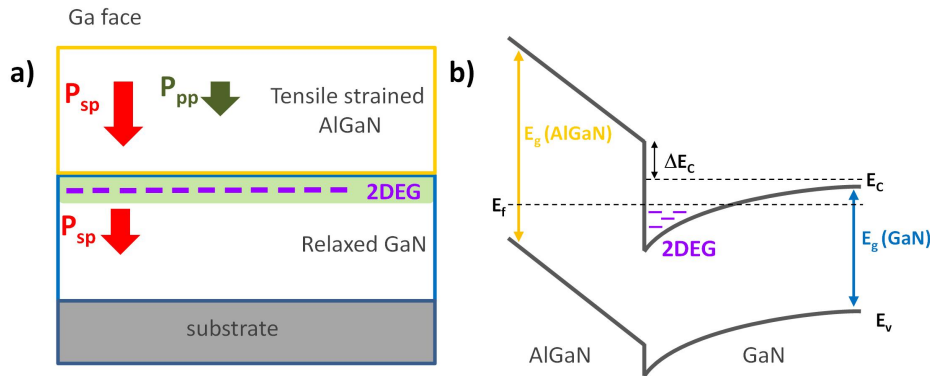


Figure 1.4: a) Schematic drawing of the HEMT structure with marked directions of the spontaneous polarization and piezoelectric polarization fields. For an AlGa_N/Ga_N HEMT epitaxial layer structure, the AlGa_N is under tensile strain and a positive polarization charge density is present at the AlGa_N/Ga_N heterojunction interface (for growth on the (0001) surface with Ga or Al face). This positive sheet charge attracts electrons at the interface and results in the formation of 2 DEG b) Schematic band diagram for AlGa_N/Ga_N interface.

detecting gases, ions, pH values, proteins and DNA.^{36,37} It is due to the fact, that the conducting 2 DEG channel of AlGa_N/Ga_N HEMT is very close to the surface and therefore extremely sensitive to absorption of analytes. The environmental perturbations of the AlGa_N surface result in a change in the electron density of the 2 DEG and hence a change in the source-drain current. For example, a flux of ions reverses the polarization of the AlGa_N and depletes the 2 DEG in the Ga_N resulting in decreased source-drain current.

Traditionally, high speed AlGa_N/Ga_N HEMTs have been mostly fabricated on insulating sapphire (α -Al₂O₃)³⁸ or semi-insulating silicon carbide (SiC) substrate.¹² Recently, significant advances have been made in improving performance of AlGa_N/Ga_N HEMTs grown on Si substrates. In most cases Si(111) orientation is chosen because of its pseudo-hexagonal symmetry favoring epitaxial growth of the Ga_N(0001) plane.^{39,40,41,42} However, a real breakthrough would be the possibility to combine the superior performance of

GaN devices with the cost effectiveness of the well established Si-based complementary metal oxide semiconductor (CMOS) technology on Si(001). An on-wafer integration of GaN-based device and Si(001) electronic through a fully Si-compatible process was demonstrated by T. Palacios *et al.*⁴³ To fabricate Si(001)-GaN-Si(001) virtual substrate, wafer bonding and etch-back techniques were used.

1.2 Bulk GaN

Developing a GaN bulk substrate is very challenging since it is impossible to use standard methods to grow a boule. The Czochralski and Birgman techniques employed for Si or GaAs manufacturing are not applicable due to the fact that the melting temperature (T^M) and the corresponding decomposition pressure at the melting point of GaN are very high (Tab.1.3). In order to

Table 1.3: Melting conditions of semiconductors.

Crystal	T^M (°C)	p^M (atm.)
Si	1400	<1
GaAs	1250	15
GaP	1465	30
GaN	2500	45000

achieve free standing GaN crystal many growth methods have been developed, including solution growth from Ga melt,^{44,45} and a variety of flux-assisted methods,^{46,47,48} in which the pressures range from atmospheric to as high as 20 kbar. Despite spectacular results and low dislocation density of grown crystals, these techniques suffer from relatively low dissolution of GaN in the melt, low controllability of the process, difficulties in implementing seeds, and a limited scalability (substrate diameter).

An alternative method is the ammonothermal growth developed and implemented by AMMONO company.^{49,50} In this technique, a GaN-containing feedstock is dissolved in supercritical ammonia solution in one zone of the high pressure autoclave. Then, it is transported through the solution by means of convection, and finally crystallized in the second zone, preferably on GaN seeds (Fig. 1.5). The typical pressures and temperatures applied in the process are 1-3 kbar and 500-600°C, respectively.

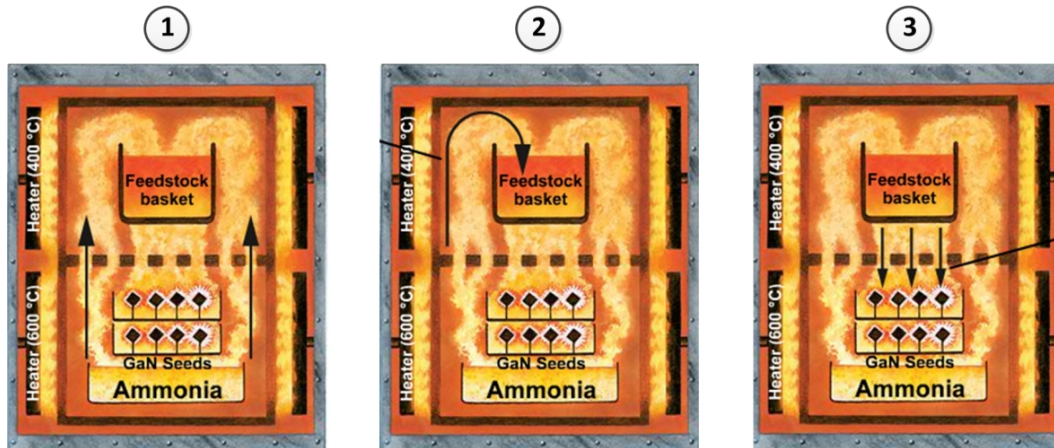


Figure 1.5: Ammonothermal GaN growth process. 1. At 500°C ammonia boils, forming a supercritical solution. Convection carries the solution to the cooler part of the autoclave. 2. The ammonia solvent attacks the GaN feedstock, firstly dissolving it and then transporting it to the GaN seeds. 3. There, GaN leaves the solution and grows on seeds enlarging them as solubility is lower for higher temperature. Figure adapted from Ref. 51.

Ammonothermal growth has several strengths: it is possible to grow high-dimension seeds with perfect crystalline quality, the process is reproducible, controllable, and scalable with the size of the autoclave. Moreover, as long-duration processes are possible, one can grow large crystals and slice them in arbitrary directions (c-, semi-polar or non-polar planes). Commercially available are 2 inch GaN wafers in the price range of 5000 dollars per piece.

1.3 GaN integration on Si substrates

The high cost of bulk GaN substrates is a major hurdle for the use of GaN in many applications. To reduce the cost one can also fabricate GaN virtual substrates on α -Al₂O₃ and SiC.^{52,53,54,55,56} However, even this solution is very expensive. As a result, α -Al₂O₃ and SiC substrate constitute a major fraction of the final GaN-based device, inhibiting the widespread adoption of GaN-based electronics and optoelectronics (for example LEDs in solid state lighting (2 inch GaN/Al₂O₃ template costs 500-1000 dollars)).

The attempts to grow GaN on Si substrates are driven mainly by two factors:

- *demand for large area virtual GaN substrates.*

Here, the engineering of readily available large diameter, low cost Si wafers offers potentially an excellent platform for the fabrication of GaN layers dedicated to LEDs applications. In this so-called **global integration** approach, (111) oriented Si wafers are commonly used as a substrate (the reasons for this choice will be discussed in section 1.2.1).

- *integration of GaN-based devices with Si-CMOS environment.*

In this approach, in contrast to the global integration scheme, a **local growth** of GaN films is mostly pursued. This potentially provides the opportunity to merge the strengths of the CMOS technology (low power digital processing) with the advantages of the GaN HEMT technologies (high power handling and high frequency operation) in mixed signal electronic applications. Since CMOS devices are fabricated on (001) oriented wafers, this type of the Si substrates is favored here also for the GaN growth.

Nowadays, GaN layers on Si substrate are usually prepared by heteroepitaxial growth by using different techniques such as Molecular Beam Epitaxy (MBE), Metal Organic Chemical Vapor deposition (MOCVD) and Hybrid Vapour Phase Epitaxy (HVPE).⁵⁷

Despite significant progress in the preparation of GaN on Si wafers, there are still many issues concerning the growth of GaN on Si. To the biggest challenges belong:

1. *Lattice mismatch*

causes a high-density of dislocations in the GaN layers, which may reduce significantly usable area and decreases material quality

2. *Thermal mismatch*

leads to large tensile strain during cooling from the growth temperature to room temperature, often resulting in wafer bowing, defects formation or even in cracked GaN layers

3. *Lack of semi-insulating Si substrates*

may lead to parasitic capacitance effects during high-frequency operation of GaN-based device. One of the most recent approaches is to use porous Si substrates to solve this issue. In this material, a large number of Si

atoms is removed from the Si crystal by an electrochemical reaction. In this way, honeycomb-like structure is created. Porous Si exhibits notably different structure and electrical characteristics compared to conventional Si. Resistivity on the order of $10^6 \Omega\text{cm}$ may be achieved. However, up to now GaN grown on porous Si exhibits a polycrystalline nature.⁵⁸

4. *Diffusion*

Si diffusion into GaN may lead to a high n-type background doping in GaN. On the other hand, Ga diffusion into Si may result in parasitic p-doping layer.

5. *Light absorption issues of the Si substrate*

light emitted in the active region of GaN-based LEDs is absorbed by Si which results in a low light extraction coefficient. Using high reflectance distributed Bragg reflector (DBR) is the cheapest way to solve this problem.^{17,18}

Among the growth challenges mentioned above the most severe problems are the large lattice and thermal mismatches between GaN and Si. Therefore, great efforts were made in the past to achieve high quality, crack-free thick GaN films grown on Si substrates. To overcome the mismatch problems many different approaches have been developed, among them: buffer layer technology, patterning and selective area growth as well as epitaxial lateral overgrowth.

1.3.1 Choice of Si wafer orientation

GaN crystal orientation, surface morphology, film polarity, optical and electrical properties strongly depend on the orientation of the Si substrate used for GaN growth.^{2,15}

Si has a diamond-like structure with the space group of $Fd\bar{3}m$, which belongs to the cubic crystal family (lattice constant $a=5.43\text{\AA}$). Single crystalline Si ingots are produced by the Czochralski (CZ) or the Float Zone (ZF) method.⁵⁹ When ingots are cut into wafers, the surface is aligned in one of several directions known as crystal orientations. The most common Si substrate orientations are: [001], [101] and [111] (Fig. 1.6).

As mentioned before, Si(001) is the favored substrate for the selective WZ GaN growth due to several reasons: it is the material widely used in the Si industry and desired for a possible integration of GaN devices with Si electronics. In addition, Si(001) is easy to etch by wet chemical etching, and easy to cleave.

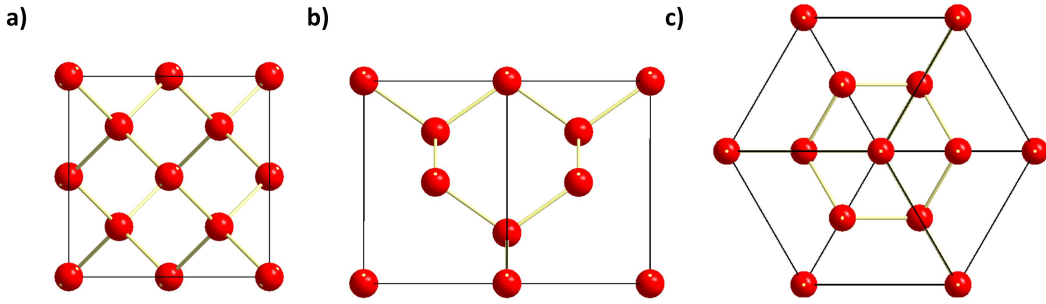


Figure 1.6: Top view of the a) Si(001) and b) Si(101) and c) Si(111) surface.

However, due to the fourfold symmetry of Si(001) surface, it is very problematic to grow single crystalline (0001) oriented GaN films on Si (001) substrate. In the global growth approach, the Si(111) plane is chosen for the growth of hexagonal GaN because of its pseudo-sixfold atomic arrangement (exact: threefold symmetry) at the Si surface. The large difference in the surface unit cell lattice parameters of GaN ($a=3.189 \text{ \AA}$) and Si ($a=3.840 \text{ \AA}$) yields a lattice parameter mismatch ($f = \frac{a_{\text{GaN}} - a_{\text{Si}}}{a_{\text{Si}}} = -17\%$), resulting in a high dislocation density of $\sim 10^{11} \text{ cm}^{-2}$. The in-plane thermal expansion coefficient (TEC) of GaN is $5.59 \times 10^{-6} \text{ K}^{-1}$ as compared to $2.61 \times 10^{-6} \text{ K}^{-1}$ for Si. Above a certain GaN layer thickness (critical thickness), this huge 56% TEC mismatch results in cracked layers (Fig. 1.7 a)), preventing device applications. Additionally, the meltback etching effect of Si by Ga leads to deterioration of the GaN layer and the Si substrate (Fig. 1.7 b) and c)).⁶⁰

There are two different approaches for cracks inhibition and dislocation density reduction.

The first technique is the strain engineering method, always based on an introduction of an additional buffer layer (one or more) between the GaN film and the Si(111) substrate to minimize the lattice mismatch or/and to compensate the tensile strain which occurs during cooling down after deposition.

The second method is to reduce the area on which epitaxy takes place so that cracks are not present in the selectively grown area. These two methods are briefly introduced in sections 1.3.2 and 1.3.3, respectively.

1.3.2 Buffer layer technology - strain engineering

Semiconductor technology requires epitaxial growth of an extremely high quality. Perfect crystal growth can only be achieved on a substrate that is identical with respect to the crystal structure, lattice constant and TEC. This is only

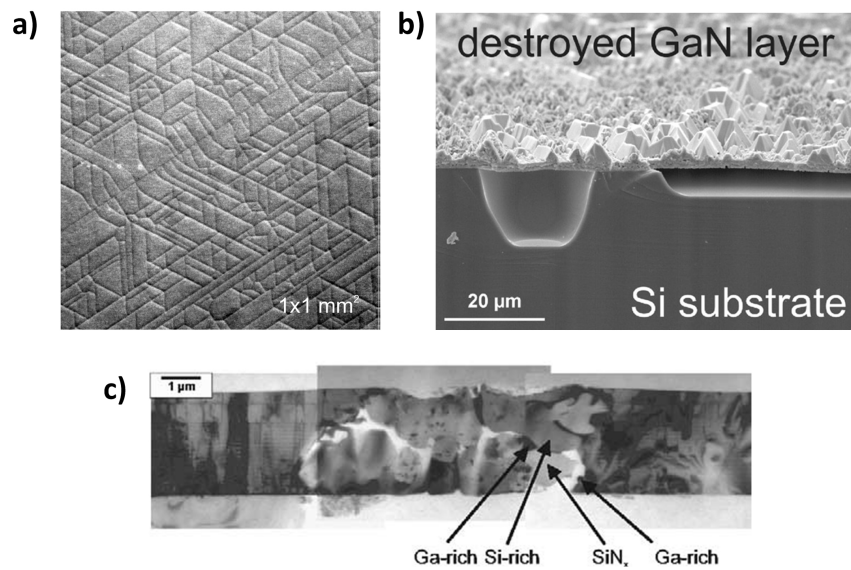


Figure 1.7: a) Cracks occur when the GaN layer thickness is above a critical thickness, b) Metal-back etching of Si by Ga,⁶¹ c) Ga-rich, Si-rich and SiN_x formation after GaN deposition directly on Si substrate.⁶⁰

guaranteed for homoepitaxy. Under those circumstances, layer-by-layer growth mode can be achieved resulting in a 2D-layer without dislocations.⁶² If a film is grown on a foreign substrate the above parameters should be matched as close as possible. Therefore, in order to obtain high quality GaN layers on a Si substrate, many types of buffer layers were investigated.

Additionally, the perfect buffer should also protect the Si substrate against nitridation (Si reacts very easily with ammonia and forms amorphous SiN_x, which passivates the surface and suppresses GaN growth) and avoid direct contact between Ga and Si due to the high reactivity of these two elements (Fig. 1.7).

Lattice mismatch

The simplest idea to accommodate the -17% lattice mismatch between GaN and Si(111) is to use a buffer layer which has a lattice constant close to the lattice constant of GaN. The best material candidates for this task are presented in Tab. 1.4. Among them AlN, SiC and oxidized AlAs are the most commonly used solutions.

A rather new buffer approach in the field of GaN heteroepitaxy on Si (111) is the use of oxide heterostructures such as: ZnO, MgO as well as γ - Al₂O₃.

An interesting idea is the use of single crystalline Al₂O₃ heterostructures grown

Table 1.4: List of the buffers used in WZ GaN(0001) growth on Si(111).

Material	structure	in-plane lattice constant a [Å]	Epitaxial mismatch with GaN [%]	
3C-SiC	zinc blende	4.36	3.5	Ref. 63
AlN	wurtzite	3.11	2.40	Ref. 64
AlAs	zinc blende	5.66	4	Ref. 65, 66
HfN	rock salt	4.52	0.35	Ref. 67
ScN	rock salt	4.50	0.10	Ref. 68
ZnO	wurtzite	3.25	2.00	Ref. 69
MgO	rock salt	4.21	6.5	Ref. 70
γ -Al ₂ O ₃	spinel	8.06	2.4	Ref. 71

on Si. This approach would immediately benefit from the developed knowledge of GaN growth on sapphire by simultaneously substituting sapphire substrates by cheap Si wafers.⁷¹ However, Al₂O₃ deposited on Si substrate does not crystallize in hexagonal sapphire (α -Al₂O₃) but in cubic spinel structure (γ -Al₂O₃). Moreover, γ -Al₂O₃ grown on Si(111) exhibits two types of domains (twinning), which may lead to the formation of additional defects in the overgrowing GaN layer.⁷²

Many efforts have been done to integrate GaN on ZnO.^{69,73,74} Due to a small lattice mismatch with GaN and wurtzite type structure, ZnO buffer would ensure a perfect template for GaN deposition. The serious disadvantage of this approach is the thermal decomposition of ZnO layers at temperatures above 600°C under H₂ and ammonia, what subsequently results in a poor nucleation of GaN.

The use of bixbyite oxide buffers, important for this thesis to grow GaN on Si(111), will be discussed in details in Section 1.4 and 3.1.

Thermal expansion coefficient mismatch

The idea behind thermal strain engineering is to use a buffer layer which introduces a compressive strain in GaN, and hence compensate the thermal tensile strain between GaN and Si. It was experimentally demonstrated that the AlN seed layer is an excellent candidate for this task.^{64,75} Additionally, when few monolayers of Al are deposited before AlN growth, the formation of SiN_x is suppressed and a rapid transition to 2D AlN growth mode is ensured. This rapid transition is essential for obtaining a high quality GaN on top of the

AlN buffer. In the ideal case, when AlN is used as a buffer, the strain of GaN on Si will change from tensile to compressive (in-plane lattice constant of AlN is smaller than the lattice constant of GaN). However, a single AlN seeding layer is usually of too low quality to induce large enough compression. Therefore, a multi-step process is used in which AlN and GaN layers are repetitively grown (Fig. 1.8 a)).⁷⁶ As a result, AlN films grown on GaN/AlN seeding layer on Si(111) are (partially) relaxed. The degree of the relaxation depends on the AlN thickness. When a thin GaN film is deposited on such a structure, it is under compressive strain which is the goal of this approach. This process can be applied several times and by using *AlN/GaN multilayers* the tensile thermal strain can be completely released and crack free 2.5 μm -thick GaN films can be achieved.⁷⁷ Moreover, the compression strain can force dislocation bending and by this enhance the probability of dislocation annihilation. Similarly, the

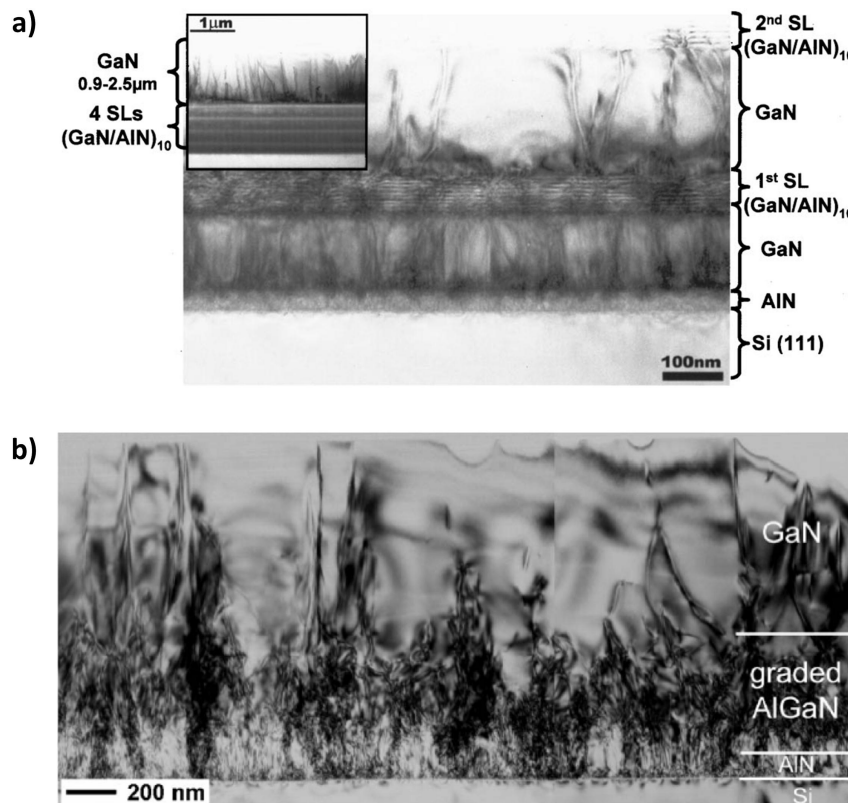


Figure 1.8: To compensate thermal tensile strain in the GaN/Si system a) AlN/GaN (3 nm/4 nm) strained layer superlattice⁷⁷ or b) $\text{Al}_x\text{Ga}_{1-x}\text{N}$ graded buffer layer can be used.

use of $\text{Al}_x\text{Ga}_{1-x}\text{N}$ graded buffer layer (with x gradually changed from 1 to 0) will induce compressive strain in the subsequently grown GaN (Fig. 1.8 b)).

In this way, the formation of cracks can be avoided to a large extent and the dislocation density can be reduced down to $2 \times 10^9 \text{ cm}^{-2}$ [Ref. 78, 79]. To reduce dislocation density even down to 10^7 cm^{-2} , additional masking layers have to be introduced (see epitaxial lateral overgrowth technique below).

Furthermore, when a combination of *AlGaN* graded buffer layer with a insertion of *AlN interlayers* is used, GaN layers without any cracks can be achieved with a layer thickness even above $7 \mu\text{m}$.⁸⁰

1.3.3 Selective area growth

Another way towards stress releasing is the deposition of GaN on Si substrates with a reduced growth area (SAG).^{81, 82, 83} This can be achieved by patterning of the Si surface (Fig. 1.9). For example, a square-patterned Si(111) can be prepared using a SiN mask and standard lithography techniques. In this it was shown that openings of $100 \mu\text{m} \times 100 \mu\text{m}$ can be overgrown with around $3.6 \mu\text{m}$ thick GaN film without any cracks.⁶⁰

Moreover, a combination of a patterning method and epitaxial lateral overgrowth technique seems to be very promising to further reduce the dislocation density.

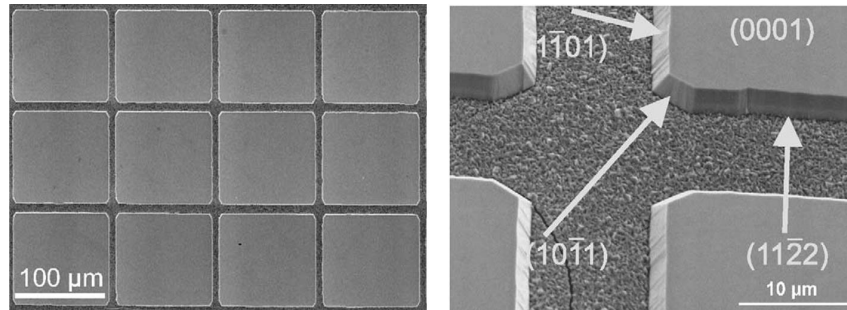


Figure 1.9: Crack-free GaN based LED structure on masked-patterned Si(111) $100 \mu\text{m} \times 100 \mu\text{m}$ regions. Cracks are present only in the masked area between openings.⁶⁰

Epitaxial lateral overgrowth

In the conventional GaN-epitaxial lateral overgrowth (ELO), GaN growth occurs by lateral homoepitaxy over the mask (predominantly SiN_x or SiO_x). The mask is used for defining the opening windows on a substrate where GaN growth has already been initiated.^{84, 85, 86} The basic concept of the ELO technique is shown in Fig. 1.10 a). It is a two stage process. During the initial GaN regrowth, the SAG is achieved in the windows without any nucleation on

the dielectric mask. By increasing the III-V ratio, the lateral growth rate is enhanced, and hence, the GaN growth over the masking area takes place. This finally leads to a full coalescence of the GaN wings. In the laterally grown regions only defects related with the wings coalescence are observed. Threading dislocation from the GaN template are blocked by the dielectric mask. On the other hand the microstructure of the GaN above the window reproduces the defect structure of the underlying template. In order to improve GaN quality in the opening area, the diameter of windows should be less than 100 nm.³ Another type of ELO process is the facet-controlled ELO (FACELO) (Fig. 1.10 b)). This technique is based on the control of GaN structures by changing growth conditions during ELO process e.g. GaN pyramids may be formed in the initial stage of the GaN growth. The facets of the pyramids play an important role in changing propagation direction of the dislocations in the laterally overgrown GaN.^{87,88}

In Pendeo epitaxy (from the Latin, to hang or be suspended) (PE), GaN pillars covered with a dielectric mask are used as a template for GaN growth. PE consists of three main steps (Fig. 1.10 c)):

1. initiation of lateral homoepitaxy from the sidewalls of the GaN pillar
2. vertical growth
3. lateral growth over the mask and wings coalescence

By applying PE, the dislocation density in the coalesced 140 μm -thick GaN film is reduced down to $6 \times 10^{-6} \text{ cm}^{-2}$.

Although, as mentioned above, ELO techniques have been proven to be very efficient to reduce the density of dislocations, they inherently suffer from the fact that the intermediate stages of the ELO (mainly mask fabrication) cause inhomogeneous impurity incorporation and stress distribution in the growing GaN layer. Therefore, many efforts have been dedicated to develop maskless and interruption-free overgrowth techniques. These techniques usually employ patterning of the Si substrates into parallel stripes^{89,90} or into holes⁹¹ (using photolithography and ion etching processes or high-dose N^+ ion implantation of Si substrate⁹²) and growth of GaN in vertical and lateral directions (Fig. 1.10 d)) Here, GaN growth starts both on the bottom of the grooves as well as on the top of the ridges. After increasing the III-V ratio the lateral growth rate

³The dislocation density in GaN grown on Si(111) is typically around 10^9 cm^{-2} . It means that the average distance between two dislocation lines is about 100 nm

is enhanced, and hence, the GaN layer growing from the top of the ridges can extend laterally over the grooves. As the lateral growth of the top GaN layer proceeds, the supply of the reactants to the bottom layer is gradually suppressed because the opening between two wings becomes narrower. After appropriate growth time, coalescence of the wings occurs. While the GaN on top of the Si ridge exhibits poor morphology, the quality of the laterally overgrown GaN on the wings is very high.

1.4 Purpose of this thesis

A new approach in the field of integration of alternative semiconductors on Si is the use of single crystalline oxide heterostructures grown on Si wafers.^{95,96,97,98} The principle advantage of oxide heterostructures as buffers is the high flexibility to tailor epitaxy parameters, i.e., the lattice constant, wetting behaviour etc., by exploiting isomorphism (solid solutions of mixed isomorphous oxides can be easily formed allowing for an extremely rich variety of lattice parameters in between the ones of the single oxides) and polymorphism (the same stoichiometric compound have different crystal lattice symmetries and parameters). In addition, metal oxides with adjustable lattice parameters can be easily deposited on Si substrate using epitaxial growth method.

1.4.1 IHP-Siltronic approach and goal of this study

The goal of this thesis is to evaluate the potential of the IHP-Siltronic patent⁹⁹ involving **global integration** of single crystalline GaN(0001) layers on Si(111) substrate using innovative metal oxide buffer films of bixbyite structure (space group $Ia-3$). Figure 1.11 shows the surface unit cell variation of different oxides included in the patent with respect to Si(111) and wurtzite GaN(0001). Among all the known bixbyite related oxide structures of the periodic system of elements, Mn_2O_3 is the crystal with the smallest lattice parameter. In consequence, the surface unit cell dimension of the cubic Mn_2O_3 (111) plane (lattice constant $a=3.33 \text{ \AA}$) match best the rather small values of the GaN(0001) basal plane (lattice constant $a=3.19 \text{ \AA}$). However, the use of Mn_2O_3 as a buffer may result in uncontrolled diffusion of Mn to the GaN layer. Mn-doped GaN material exhibits magnetic properties¹⁰⁰ which are used in spintronic but do not have an application in optoelectronic devices. Therefore, instead of Mn_2O_3 , the Sc_2O_3 (lattice constant $a=3.48 \text{ \AA}$) material was chosen as a buffer

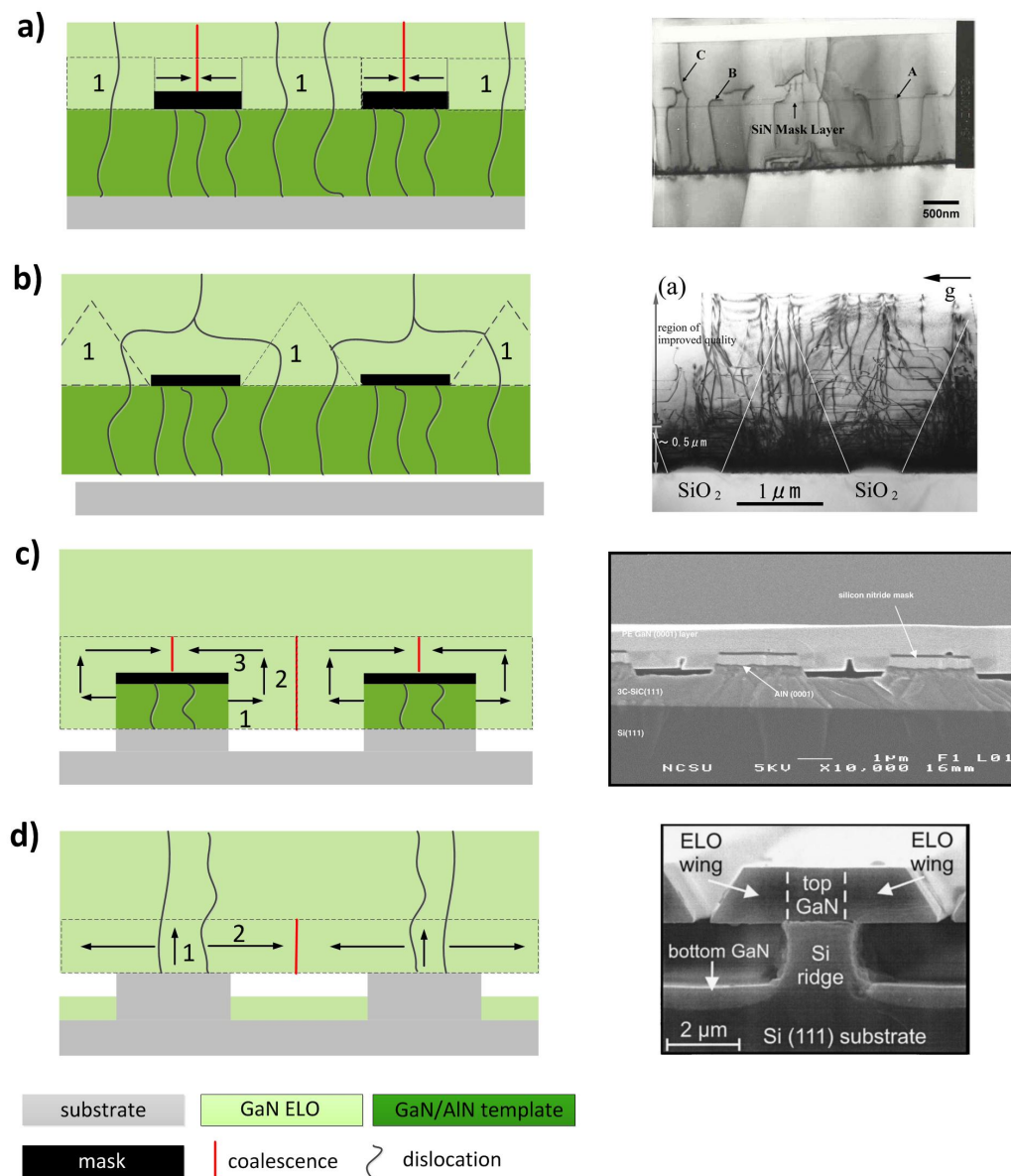


Figure 1.10: Review of ELO techniques: a schematic diagram (left) and examples of experimental results from the literature (right): a) Basic ELO process. The ELO GaN extends over the SiN mask through the opening. Thus, dislocations in the film under the mask cannot propagate into overgrown GaN layer.⁹³ b) FACELO process. During initial stage of the growth, GaN pyramids are formed. The facets of the pyramid plays an important role in changing the propagation direction of the dislocations in the laterally overgrown GaN c) PENDEO epitaxy.⁹⁴ d) Deposition of GaN on the grooved stripe structures on Si(111) substrate. The laterally grown GaN wings are defect-free.⁸⁹

for GaN growth on Si(111). First promising results concerning GaN epitaxy on AlN(0001)/Sc₂O₃(111)/ Si(111) supports were reported in Ref. 97. It was

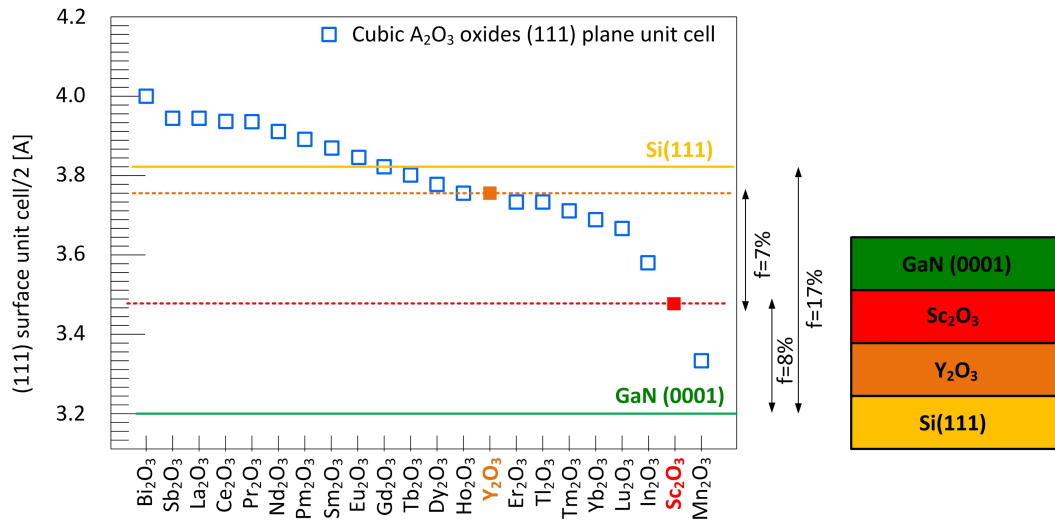


Figure 1.11: Fig. shows half of the (111) surface unit cell dimension of the cubic metal oxides included in the IHP-Siltronic patent. The (111) surface unit cell of Si (yellow solid line) and (0001) of GaN (green solid line) are marked in the figure. By applying $\text{Sc}_2\text{O}_3/\text{Y}_2\text{O}_3$ buffer the 17% lattice mismatch between GaN and Si can be theoretically reduced to the 8% (lattice mismatch between GaN and Sc_2O_3).

shown that single crystalline GaN(0001) layers on the oxide/Si(111) templates are possible to achieve. Interestingly, the oxide buffer was thermodynamically stable at the GaN deposition temperature and all interfaces remained sharp after growth. However, the large lattice mismatch between Sc_2O_3 and Si ($\sim 9\%$) results in high defect density in the Sc_2O_3 buffer which may degrade the properties of the GaN layer.

In order to improve the crystalline quality of the Sc_2O_3 layer and hence the quality of the overgrown GaN film an additional buffer between Sc_2O_3 and the Si substrate should be used. The idea of a bi-layer oxide buffer (or alternatively a compositionally graded buffer) approach is to reduce the defect density in the Sc_2O_3 and GaN epilayers by changing the lattice constant from Si to GaN in a more gradual and continuous way. A similar technique is already successfully applied in the SiGe epitaxy on Si wafers.¹⁰¹ Analysis of the bulk crystal lattices of available oxides included in the IHP-Siltronic patent shows that Y_2O_3 has an extraordinary small in-plane lattice misfit of $\sim -2\%$ to Si which enables growth of very good crystalline quality Y_2O_3 layers on Si, as it was previously demonstrated by a number of publications.^{102, 103, 104, 105} The lattice mismatch between Y_2O_3 and Sc_2O_3 is about -7% . Y_2O_3 appears thus as a good candidate to play the role of a lattice match mediator between the

Si substrate and the Sc_2O_3 buffer. Ideally, the new buffer for GaN growth on Si would be composed of a pure crystalline Y_2O_3 at the interface with Si and would gradually change in composition to achieve pure Sc_2O_3 at the interface with GaN.

The road to the challenging goal of the integration of 2D, single crystalline, and low defect density GaN layers on Si via Sc_2O_3 - Y_2O_3 buffers will begin with the preparation of buffers comprising discrete layers of single crystalline Sc_2O_3 and Y_2O_3 on Si(111) wafers. This will be followed by the optimization of the GaN growth conditions on such substrates. The realization of the GaN/ Sc_2O_3 / Y_2O_3 /Si(111) heterostructures and their characterization are the two main assignments of this thesis.

1.4.2 Organisation of the thesis

This dissertation includes the following chapters:

Chapter 2 presents the experimental instrumentations utilized to deposit and characterize the GaN/ Sc_2O_3 / Y_2O_3 /Si(111) heterostructures, with a brief discussion of the scientific basis of each employed technique.

Chapter 3 consists of the main part of the studies. Here, results of the structural characterization together with a detailed discussion are given. This chapter is divided into four sections:

Section 3.1 deals with the structural quality of the Sc_2O_3 / Y_2O_3 /Si(111) templates.

Section 3.2 presents the "proof-of-principle" study of thin GaN layers grown on Sc_2O_3 / Y_2O_3 /Si(111).

Section 3.3 presents and discusses the growth diagram of GaN on Sc_2O_3 / Y_2O_3 /Si(111) and reports about the crystalline and optical quality of thick GaN layers.

Section 3.4 deals with the initial growth stages of GaN layers on Sc_2O_3 by means of in-situ surface analysis techniques.

Chapter 4 summarizes the results obtained during the PhD thesis on the GaN/ Sc_2O_3 / Y_2O_3 /Si(111) heterostructure and poses an outlook for future experiments and analyses.

Chapter 2

Experimental background

2.1 Substrate preparation and layer growth

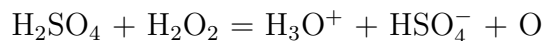
The substrates used in this thesis are single crystalline Si wafers, provided by Siltronic. They have a diameter of 4" (100 mm) and are 525+/- 15 μm thick. The wafers are produced by Czochralski pulling. The surface orientation is [111] +/- (0.5°). The doping is of p type, the dopant is Boron, resulting in a specific resistance of 5 – 15 Ω cm.

2.1.1 Substrate cleaning

Prior to the oxide layer deposition, Si substrates were cleaned according to the following procedure:¹⁰⁶

1. **10 min rinse in de-ionized water.**
2. **10 min Piranha etching.**

The Piranha solution is a mixture of sulphuric acid (H_2SO_4) and hydrogen peroxide (H_2O_2). The chemical reaction is the following:



The highly reactive atomic oxygen virtually "eats up" anything, especially Carbon contaminations, which have proven to be very resistant towards aqueous reactions at room temperature. The Piranha cleaning is applied to free the wafer of organic contaminations, however, it does not remove inorganic contaminations such as metals.

3. **1 min rinse in de-ionized water**, in order to remove from the wafer surface the very viscous liquid remained after the Piranha solution.

4. 1 min RCA cleaning.

The RCA cleaning method is used to free the Si wafer of the native SiO_2 and inorganic contaminations. It is a sequential chemical oxidation in a peroxide solution H_2O_2 followed by the oxide removal in a HF solution. In the cleaning process, contaminations like particles are embedded in the chemically formed SiO_2 and then stripped off by HF etching (Si itself cannot be etched by HF). The sequence of H_2O_2 and HF dipping is repeated several times to decrease the surface roughness. This leaves a clean, chemically stable Si surface that is passivated by Hydrogen.

5. 5 min rinse in de-ionized water.

6. **30 min exposition to ammonium fluoride (NH_4F)**, in order to further reduce surface roughness down to the atomic scale.

7. 5 min rinse in de-ionized water.

Cleaned H-passivated Si(111) wafers are introduced within four minutes into the load-lock chamber which is subsequently evacuated to high vacuum (HV) conditions (10^{-6} mbar). Once the HV conditions are established, the Si substrates are degassed at 200°C for 20 minutes. In this way, atmosphere contaminations (water etc.) absorbed during the transfer from the wet chemistry facility to the Molecular Beam epitaxy set-up are degassed. Subsequently, the wafers are transferred to the ultra HV (UHV) deposition chamber.

2.1.2 Molecular Beam Epitaxy

Molecular Beam Epitaxy (MBE) is a deposition technique for producing high quality epitaxial structures with monolayer control. The deposition is always performed under UHV conditions to avoid any possible contaminations during the epitaxial growth process. The material to be deposited (source material) is evaporated using either electron beam evaporation by electron guns (e-gun) or by thermal heating from a Knudsen cell (K-cell). The purity of the source materials is better than 99.99%. The crucibles/ K-cells are covered with a shutter to abruptly start and stop the deposition. Before the growth process starts, the materials in the sources are heated for a couple of minutes to ensure stable evaporation rate. The sample is placed in the molecular beam of the evaporated material and condensation on the sample surface forms the desired layer atom by atom. There are several parameters that determine the growth rate on the sample: the flux of the atomic or molecular beam determines the

number of atoms per time that arrive at the sample surface and the temperature of the sample influences the kinetics of the particles. Furthermore, to improve film homogeneity over the whole 4" Si (111) wafer surface the sample is rotated during the deposition process.

All deposition chambers are equipped with Reflection High Energy Electron Diffraction (RHEED) allowing to monitor in-situ the crystal quality of the growing layer.

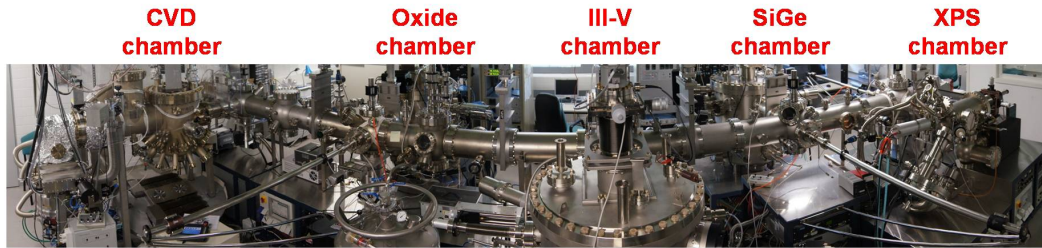


Figure 2.1: IHP MBE equipment consisting of the separated growth chambers.

The MBE system used in this thesis is a DCA 600 (Fig. 2.1). It consists of a load-lock, a buffer line for wafer transfer, and three MBE growth chambers, one for oxides, one for Si-Ge and one for III-V materials. In addition, a new RIBER CVD chamber dedicated to the graphene growth is connected to the system.

Oxide deposition

Prior to the oxide deposition, the H terminated wafer is heated in the oxide chamber up to 750°C to prepare a high quality (7×7) Si (111) surface. The source materials (stoichiometric Y₂O₃ and Sc₂O₃ powder materials) are evaporated using e-guns from a graphite crucible. Y₂O₃ and Sc₂O₃ layers are prepared at the substrate temperature of 625°C and 500°C, respectively. In both cases, the deposition rate is usually in the range of 0.003-0.03 nm/s. The background pressure in the growth chamber is 10⁻¹⁰ mbar, but typically drops to 10⁻⁶ mbar during growth, mainly due to oxygen outgassing from the source material. Pressure is measured by means of an ion gauge. After oxide deposition, the oxide/Si(111) heterostructures are transferred under UHV conditions to the III-V chamber.

GaN deposition

Before GaN deposition, the $\text{Sc}_2\text{O}_3/\text{Y}_2\text{O}_3/\text{Si}(111)$ wafers are annealed in the III-V chamber at 750°C for 30 minutes. For GaN layers growth, high purity Ga is thermally evaporated by a conventional K-cell and nitrogen gas is cracked by the radio frequency (RF) plasma source to activate nitrogen species (Oxford HD 25). Typically, the Ga cell temperatures are set to $900\text{-}1000^\circ\text{C}$. It depends on the GaN growth regime. RF nitrogen plasma source is operated at a power of 300 W and N_2 gas flow is regulated by the flow meter and is set to 0.5-2 sccm (standard cubic centimeters per minute). The substrate temperature during growth is 720°C .

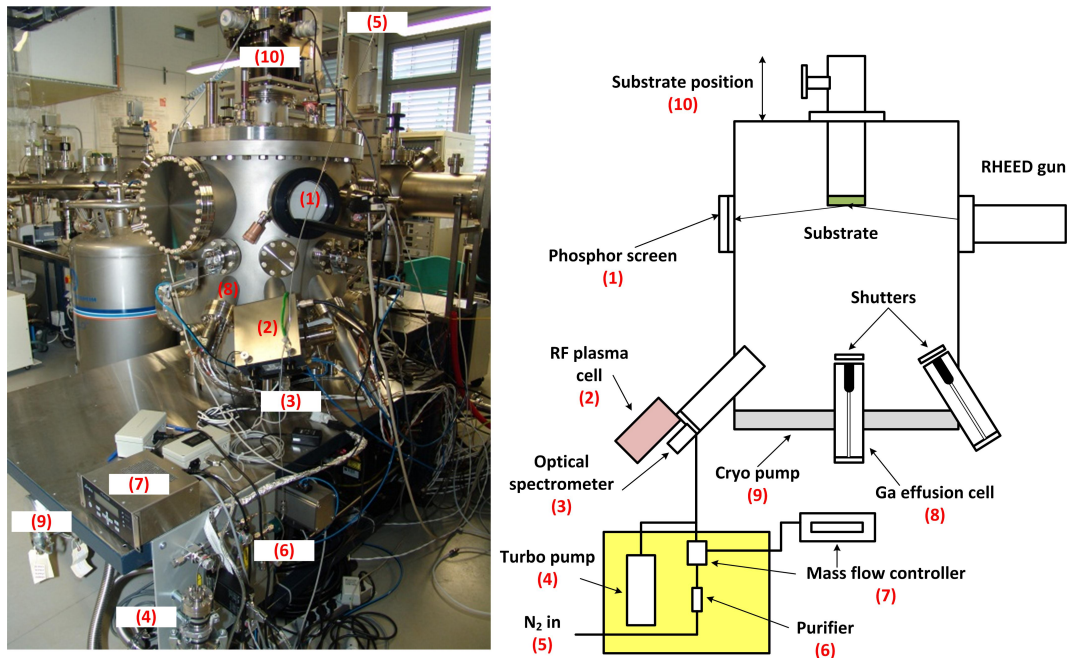


Figure 2.2: a) Picture and b) Schematic diagram of a RF MBE system used for GaN growth at IHP. 1 - Phosphor screen (part of RHEED), 2 - RF-plasma cell, 3 - Optical spectrometer (to measure nitrogen plasma brightness), 4 - Turbo pump, 5 - N_2 inlet, 6 - N_2 purifier, 7 - Mass flow controller (to measure flow of N_2), 8 - Ga effusion cell, 9 - Cryo pump, 10 - Manipulator to change substrate position.

Principles of GaN growth by MBE

During GaN deposition by MBE several processes compete with each other, namely: adsorption, desorption, surface diffusion, incorporation and decom-

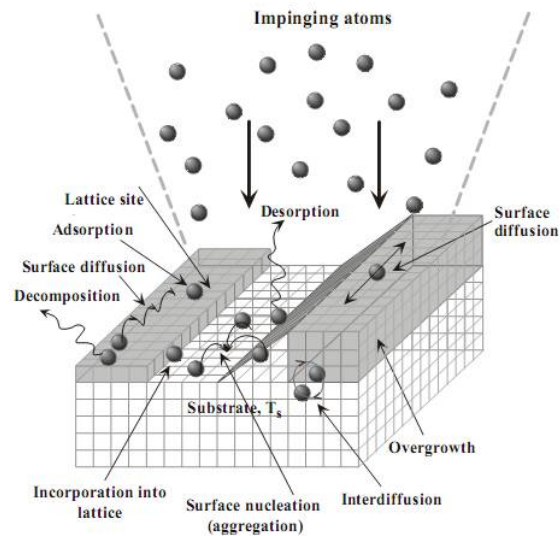


Figure 2.3: Surface processes during the MBE growth: adsorption, desorption, surface diffusion, lattice incorporation and decomposition. (Figure adapted from Ref. 2.)

position (Fig. 2.3).²

1. *Adsorption* is given by the atomic or molecular species which impinge on the substrate surface and stick by overcoming the activation barrier.
2. *Desorption* is a process in which a species that is not incorporated into the crystal lattice leaves the substrate by thermal re-evaporation.
3. During *surface diffusion* species diffuse on the substrate surface to find low energy crystal sites for incorporation.
4. During *incorporation* species bond to the substrate or epilayer by attaching to a dangling bond, vacancy, step edge, etc. There are three modes of growth/incorporation namely:¹⁰⁷
 - *Frank-van der Merve* (FM)- is a layer-by-layer growth mode. Each layer is fully completed before the next layer starts to grow, and it is a strictly two-dimensional (2D) growth mode.
 - *Volmer-Weber* (VW)- is an island growth mode. In this case, three-dimensional (3D) islands nucleate and grow directly on the substrate surface.

- *Stranski-Krastanov* (SK)- is a layer-plus-island growth mode and represents the intermediate case between the FM and VW growth modes. After the formation of a complete 2D layer of a few monolayer thickness (the exact value, the so called SK thickness, depends on the film strain and surface energies involved), the growth of a 3D layer (islands) takes place.
5. During *decomposition* atoms in the crystal lattice leave the surface after breaking their bonds. GaN decomposition rate under UHV conditions is nearly zero below a substrate temperature of 750°C , increases rapidly above 800°C , and reaches $1\ \mu\text{m}/\text{h}$ at 850°C . This means that it may be impossible to grow GaN at high temperatures¹⁰⁸ (Fig. 2.4).

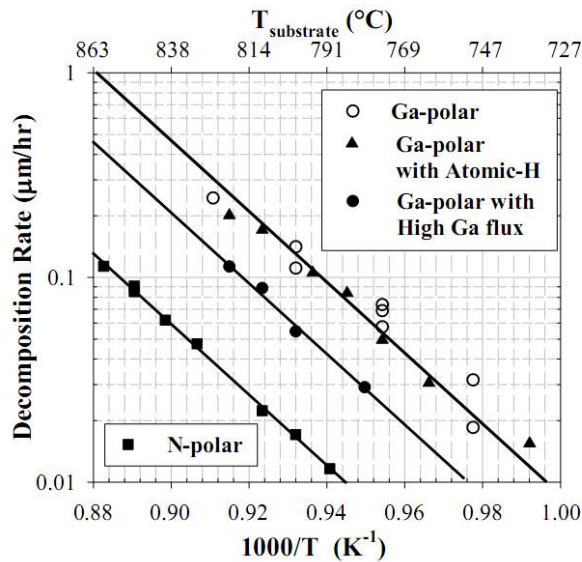


Figure 2.4: Thermal decomposition of GaN. Decomposition rate must be taken in to account when growth is performed at a high substrate temperature; and can be neglected when low temperatures are used.

GaN growth is a metastable process which is controlled by a competition between the forward reaction (Ga and N incorporate into the film and GaN epilayer forms) and the reverse reaction (GaN decomposition). The forward reaction depends on the arrival of Ga atoms (Ga flux, J_{Ga}) and activated nitrogen (N flux, (J_{N})) species on the surface, as well as the substrate temperature, while the reverse reaction is strongly affected mostly by the substrate temperature. Certainly, in order to grow GaN film, the rate of GaN formation must be larger than the rate of decomposition.

In general, GaN film deposition may be performed under two different conditions, namely: *Ga-rich* and *N-rich* condition.^{109,110,111,112}

- Under N-rich condition, GaN growth rate is limited by the amount of available Ga atoms, hence it increases monotonically with the J_{Ga} . This regime occurs for any substrate temperature when $J_{Ga}/J_N < 1$.
- In case of Ga-rich condition, the GaN growth rate is limited by the amount of available reactive nitrogen since excess Ga is present on the surface. The growth rate increases monotonically with increasing flux of reactive nitrogen species (J_N). This growth regime occurs for sufficiently low substrate temperature (where Ga desorption can be neglected) when $J_{Ga}/J_N > 1$. The excess Ga forms a steady-state 2-D Ga adlayer or accumulates on the surface, forming not desired 3-D droplets (when the Ga adlayer is thicker than 3 monolayers).

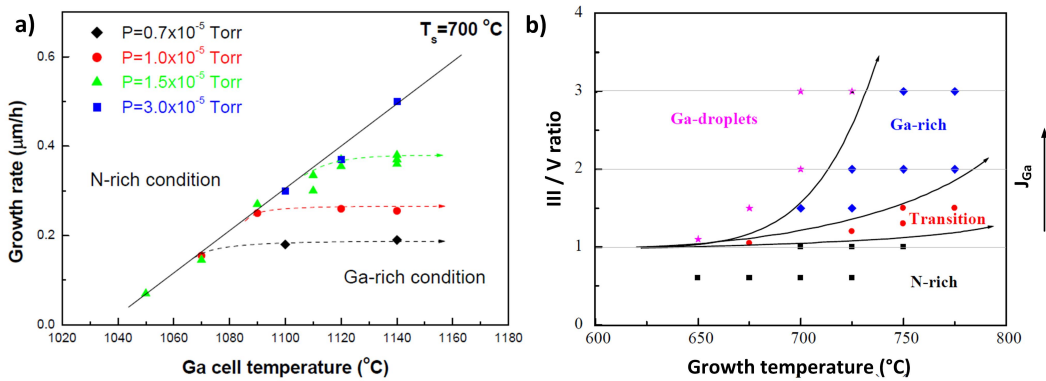


Figure 2.5: GaN growth diagrams: a) The growth rate versus Ga cell temperature for different system pressure at a substrate temperature of 700°C . The solid line indicates the stoichiometric condition b) Surface phase diagram for MBE GaN grown on GaN templates for fix N flux and different Ga flux (different Ga/N ratio). (Figure adapted from Ref. 2).

GaN growth regimes may be determined based on the calibration diagram. An example of such a graph is presented in Fig. 2.5 a). Here, the GaN growth rates (at a substrate temperature of 700°C) are plotted as a function of the Ga effusion cell temperatures (determines J_{Ga}) for different nitrogen pressures. When the Ga cell temperature (T_{Ga}) is low, the growth rate increases linearly with the T_{Ga} for the constant system pressure (determines J_N). This behavior indicates N-rich growth conditions. The growth rate saturates when T_{Ga} is

higher than a certain value. Above that temperature the growth rate remains constant, although the T_{Ga} increases, and the growth is under Ga-rich conditions. The Ga cell transition temperature from the N to Ga rich regimes varies with the system pressure, and is shown in the Figure by the solid line. This line indicates the stoichiometric condition with $J_{Ga}/J_N \sim 1$. On the left side of the solid line ($J_{Ga}/J_N < 1$) growth is in the N-rich regime whereas on the right side ($J_{Ga}/J_N > 1$) growth is in the Ga-rich regime.

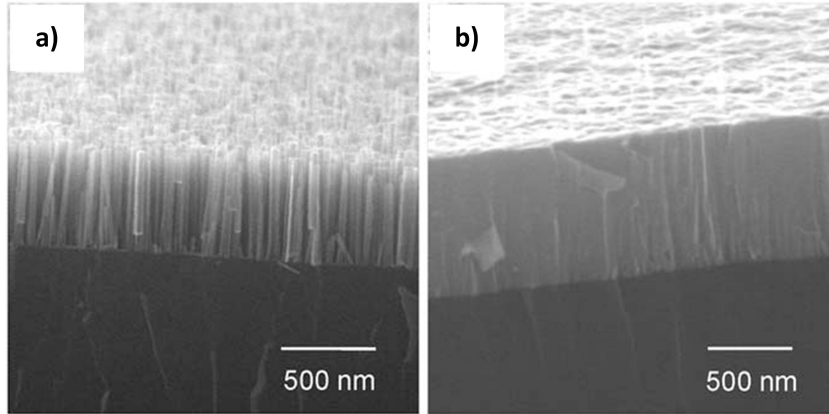


Figure 2.6: Tilted SEM image of GaN sample grown under a) N-rich condition and b) Ga-rich condition. (Figure adapted from Ref. 113)

GaN growth conditions have a strong impact on the GaN surface morphology, GaN crystal quality and optical properties. Fig. 2.5 b) shows the so-called GaN growth diagram. Here, four characteristic growth regimes can be determined:

1. *N-rich growth regime* (excess N covers the GaN surface): $J_{Ga}/J_N < 1$
GaN exhibits granular surface morphology, with a tilted columnar structure with a high density of stacking faults (Fig. 2.6 a)
2. *Transition growth regime* (stoichiometric condition) : $J_{Ga}/J_N \sim 1$
GaN surface morphology is characterized by inverted pyramids
3. *Ga-rich growth regime* (Ga adlayer covers the GaN surface): $J_{Ga}/J_N > 1$
GaN exhibits smooth surface morphology with characteristic spiral growth hillocks and some Ga droplets (Fig. 2.6 b)
4. *Ga droplet growth regime* (Ga droplets formation on top of Ga adlayer):
 $J_{Ga}/J_N \gg 1$

The optimum GaN film properties are usually achieved when the growth is performed on the boundary between the Ga-rich and Ga-droplet regime. Under

this growth condition, the GaN surface is covered by around 2.5 ML-thick Ga adlayer. The existence of a stable Ga surface bilayer has a strong impact on an adatom diffusion and ensure layer-by-layer growth mode (excess Ga acts as a surfactant).^{114,115,116} A very useful method for determining in-situ the GaN growth regimes is RHEED. Simplified, rough surface morphology (N-rich condition) results in a spotty RHEED pattern, whereas smooth surface (Ga-rich) exhibits a streaky pattern.¹⁰⁹

2.2 Characterization techniques

In the following sections, the main materials science characterization techniques used in this study are briefly reviewed.

2.2.1 X-ray diffraction

X-ray diffraction (XRD) is a non-destructive analytical technique, which reveals information about the crystallographic structure of materials.^{117,118} It is based on the elastic scattering (X-ray photons do not lose any energy) of electromagnetic wave with the energy in the range of 1 keV to 120 keV from the periodic electron density distribution of the matter. The interaction of X-ray with electrons in atoms may be described by *Thomson scattering* i.e. interaction of light with a free electron. In the classical description of the scattering process, an electron is forced to vibrate when placed in the electric field of an incidence X-ray beam. The vibrating electron acts as a electromagnetic wave source, and radiates like a dipole. The intensity of the scattering radiation at the distance R from the electron at an angle ϕ is given by the equation:

$$I_e = I_0 \frac{e^4}{m^2 c^4 R^2} \left(\frac{1 + \cos^2 \phi}{2} \right) \quad (2.1)$$

Here, I_0 and $(1 + \cos^2 \phi) / 2$ are called intensity and polarization factor for an unpolarized primary beam, respectively. It is noteworthy that the ratio $e^4 / m^2 c^4 \sim 8 \times 10^{-26} \text{ cm}^2$, so that the intensity of X-ray scattering from one electron is pretty much zero, and a X-ray signal is recorded only when the number of scattering objects is of the same order of magnitude as the *Loschmidts number* ($\sim 3 \times 10^{19} \text{ cm}^{-3}$) or, in case of ultra-thin films studies, only when high-brilliance synchrotron radiation sources are employed.

Scattering from crystal

In the previous section, the interaction of an X-ray with a free electron was briefly discussed. Since the interatomic distances are comparable with the wavelength of incoming light, a small crystal exposed to coherent X-rays gives rise to constructive and destructive interference of the scattered wave. In consequence, a diffraction pattern can be observed and further analysed. In order to properly describe this effect, two additional factors must be taken into account: the *structure factor* F and the *lattice factor* G .

At point P, the intensity of X-rays with the wavelength λ scattered from a cubic crystal with $N_i a_i (i = 1; 2; 3)$ edges along a_i crystal axes is written as

$$I = I_e F^2 G^2 \quad (2.2)$$

where

$$F = \sum_n f_n e^{i2\pi/\lambda \cdot (s-s_0) \cdot r_n} \quad (2.3)$$

$$G^2 = \frac{\sin^2[\pi/\lambda \cdot (s-s_0)N_1a_1]}{\sin^2[\pi/\lambda \cdot (s-s_0)a_1]} \cdot \frac{\sin^2[\pi/\lambda \cdot (s-s_0)N_2a_2]}{\sin^2[\pi/\lambda \cdot (s-s_0)a_2]} \cdot \frac{\sin^2[\pi/\lambda \cdot (s-s_0)N_3a_3]}{\sin^2[\pi/\lambda \cdot (s-s_0)a_3]} \quad (2.4)$$

Here, \mathbf{s}_0 and \mathbf{s} are the unit vectors defining the propagation direction of initial and scattered beam, respectively. Scattering from a small crystal is shown schematically in Fig. 2.7. In Eq. 2.3, f_n is the form factor of the n^{th} atom whereas r_n is the position of the n^{th} atom in the unit cell. Thus, the structure factor F corresponds to the atomic arrangement within a unit cell and can be used to determine the type of crystal structure.

From its definition, the lattice factor G corresponds to the periodicity of the crystal. The shape of the observed signal depends strongly on the number of coherently scattering unit cells N_i (Eq. 2.4). In general, peak height increases and its full width at FWHM decreases for higher N_i . Moreover, the intensity of the scattered X-ray is essentially zero except for the cases when the three coefficients of G are simultaneously close to their maxima. In other words, it is only satisfied when the three so-called Laue equation are satisfied:

$$\pi/\lambda(s-s_0)a_1 = h\pi$$

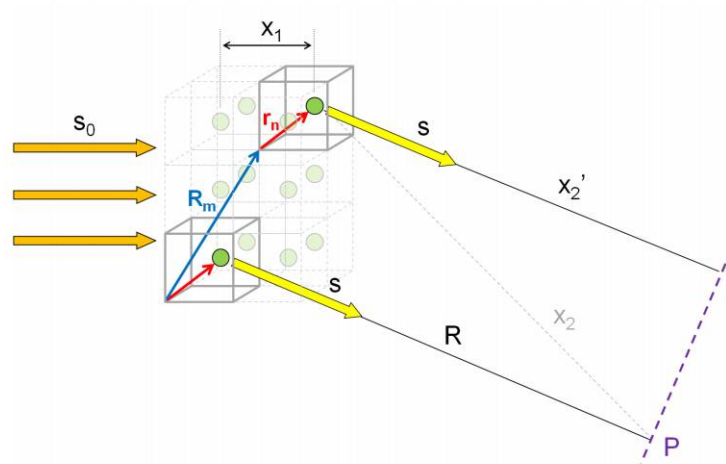


Figure 2.7: Schematic scattering of a parallel X-ray beam on a small crystal. R_m denotes the position of m^{th} unit cell whereas r_n corresponds to the position of n^{th} atom in a unit cell. The crystal is small enough to assume that the primary and the scattered beam are plane waves which leads to $(x_1+x_2)-(x_1+x_2')$.

$$\begin{aligned}\pi/\lambda(s - s_0)a_2 &= k\pi \\ \pi/\lambda(s - s_0)a_3 &= l\pi\end{aligned}\quad (2.5)$$

where h , k , and l are integer numbers which are known as the Miller indices and $\mathbf{s}-\mathbf{s}_0/\lambda=\mathbf{Q}$ where \mathbf{Q} is the impulse transfer vector.

The Laue condition is shown in a vector form in Fig. 2.8. The incident and diffracted wave vectors are indicated as $\mathbf{K}_0=\mathbf{s}_0/\lambda$ and $\mathbf{K}=\mathbf{s}/\lambda$. If no energy is gained or lost in the diffraction process then $K_0=K$. A Bragg peak is observed when the impulse transfer vector \mathbf{Q} (difference of the incoming and outgoing wave vector \mathbf{K}_0 and \mathbf{K}) is identical in magnitude and direction to the reciprocal lattice vector \mathbf{H}_{hkl} ($\mathbf{Q}=\mathbf{H}_{hkl}$).

As introduced in basic solid state physics, the lattice d -spacing in a single crystal has the following relation to the reciprocal lattice vector:

$$d_{hkl} = \frac{1}{H_{hkl}} \quad (2.6)$$

which, by using the relationship from Fig. 2.8:

$$\sin \theta = \frac{Q}{2 K_0} \quad (2.7)$$

allows to derive Bragg's law for X-ray diffraction from the Laue condition in vector form:

$$\frac{1}{d} = 2K_0 \sin \Theta$$

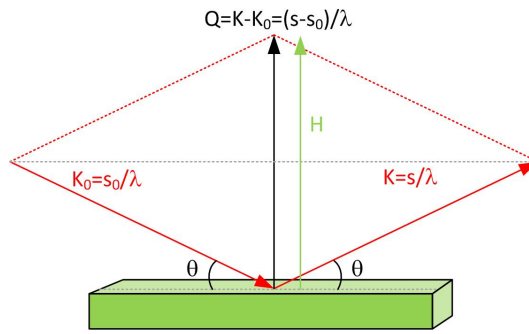


Figure 2.8: Relations involved in the vector presentation of the Laue condition. Diagram shows the Bragg law in vector form.

$$\begin{aligned} \frac{1}{d} &= 2 \frac{1}{\lambda} \sin \Theta \\ n\lambda &= 2d \sin \theta \end{aligned} \quad (2.8)$$

In this form, diffraction occurs when the path difference is equal to a multiple integer n of λ . The corresponding scattering geometry for the detection of a certain Bragg peak is fulfilled by setting the X-ray source, the detector and the sample position in the correct configuration.

More details about X-ray diffraction theory can be found in Ref. 117

X-ray experimental set-up

Laboratory-based X-ray diffraction was carried out using a Rigaku Smart-Lab diffractometer, equipped with a 9 kW rotating anode emitting Cu K_α radiation ($\lambda = 0.154$ nm). In the standard XRD arrangement, the sample is fixed in a horizontal position and source and detector are moved in ω - 2θ mode. It is possible to rotate the sample around an axis perpendicular to the sample surface (defined as an angle ϕ) and to tilt the sample by an angle χ around an axis defined by the beam direction for $2\theta=0^\circ$. Definitions of rotation angles used in XRD experiments are schematically shown in Fig. 2.9. In addition, XRD scans may be performed in two different resolution modes: low resolution (LR) and high resolution (HR). In the LR mode, a multilayer X-ray mirror in combination with slit systems is only used for beam collimation. The HR mode uses a twofold Ge (400) crystal behind the X-ray mirror to collimate and monochromatize the X-ray beam.

Moreover, high temperature XRD experiments (in temperature range: 27-900 $^\circ\text{C}$) may be done by mounting on the diffractometer an oven from Anton Paar. For higher resolution and sensitivity than feasible with laboratory based equip-

ment, synchrotron radiation XRD (SR-XRD) experiments in this study were carried out at the insertion device beamline ID32 at the European Synchrotron Radiation Facility (ESRF) in Grenoble.¹¹⁹

The different types of XRD experiments performed in this thesis, namely specular θ - 2θ scans, ω - scans, reciprocal space maps (RSMs), grazing-incident (GI) in-plane measurements, pole figures and χ -scans are explained in the following.

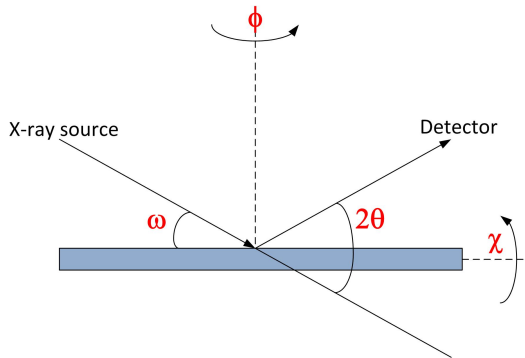


Figure 2.9: Definition of rotation angles in XRD experiments: ω angle between the sample surface and source, 2θ angle between incident X-rays and the detector, χ sample tilt, ϕ in-plane sample rotation angle.

Specular θ - 2θ and ω scan

For determining the vertical growth orientation of the heterostructure as well as the out-of-plane lattice constant, specular θ - 2θ ($\theta=\omega$) were employed. The diffraction spectrum is collected by rotating simultaneously both: the X-ray source and the detector by θ and keeping the sample fixed. In this case, the magnitude of \mathbf{Q} varies while maintaining its orientation parallel to the sample normal (Fig. 2.10 b). The resulting plot of intensity versus 2θ shows peaks for \mathbf{Q} values satisfying the diffraction condition of a certain net plane ($\mathbf{H}_{HKL} = \mathbf{Q}_{HKL}$). Peak position determines the out-of-plane lattice constant and can give indications about the strain in the epitaxial layer. Moreover, the FWHM of the Bragg peak is (in a rough approximation) inversely proportional to the thickness of the perfect crystalline layer (FWHM of the thick layer can be limited by defects on c-planes).

For determining the out-of plane mosaicity of the layer orientation, the ω scan (also called *rocking curve scan*) may be employed. In this case, the orientation of \mathbf{Q} rocks through the Bragg peak while maintaining its magnitude

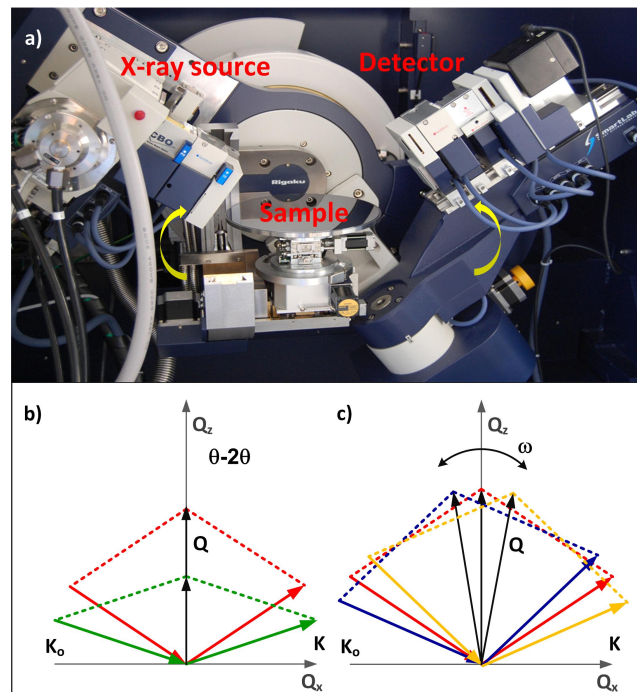


Figure 2.10: a) Rigaku SmartLab diffractometer during θ - 2θ measurement b) definition of symmetric: θ - 2θ scan and c) rocking curve scan ω .

(Fig. 2.10c). When diffraction intensity versus ω is plotted for various orders of the Bragg peaks, it is possible to derive from the FWHM the out-of-plane mosaicity (tilt angle of the crystal blocks) of the layer (Williamson-Hall analysis¹²⁰). In case of a perfect crystal without out-of plane mosaicity, the rocking curve FWHM does not vary with the order of the Bragg peak.

A combination of series θ - 2θ and ω scans is a so-called RSM measurement. It is performed such that the Bragg reflection under investigation is fully mapped in a confined area in \mathbf{Q} space. This means that the reflection is not monitored only by one rocking curve crossing it, but the whole area in its vicinity is included in the measurement. One way of mapping consists in performing subsequent rocking curves with increasing scattering angle 2θ in a range centered around $2\theta_0$. The power of RSMs is for example given by the fact that defect-related diffuse X-ray scattering can be analyzed.

χ scan

The strain state of the oxide layers can be analyzed by means of an XRD technique which identifies the presence of tetragonal distortions in heteroepi-

taxially grown cubic layers.¹²¹ This method is based on calculating a cubic unit cell lattice constants from differently tilted diffracting netplanes. The angle χ is the angle between the sample surface e.g. (001) and the tilted (hkl) netplane (Fig. 2.11 a)). Assuming an undistorted cubic lattice, a hypothetical cubic unit cell constant is calculated from the position of the Bragg peaks of the various tilted lattice planes. These values are plotted as a function of $\cos^2(\chi)$. For example, the out-of-plane Bragg planes ($\chi=0$) are plotted at $\cos^2(\chi)=1$, the in-plane Bragg planes ($\chi=1$) are plotted at $\cos^2(\chi)=0$. In case of bulk crystal the in-plane and of-plane lattice constant are equal and a horizontal line is achieved. If the layer is under in-plane tensile or compressive strain, the in-plane lattice constant is smaller or bigger than expected bulk value, respectively (Fig. 2.11 b)). It is noted that this technique allows to discriminate for cubic epilayer systems whether lattice constant variations are due to strain or intermixing effects.

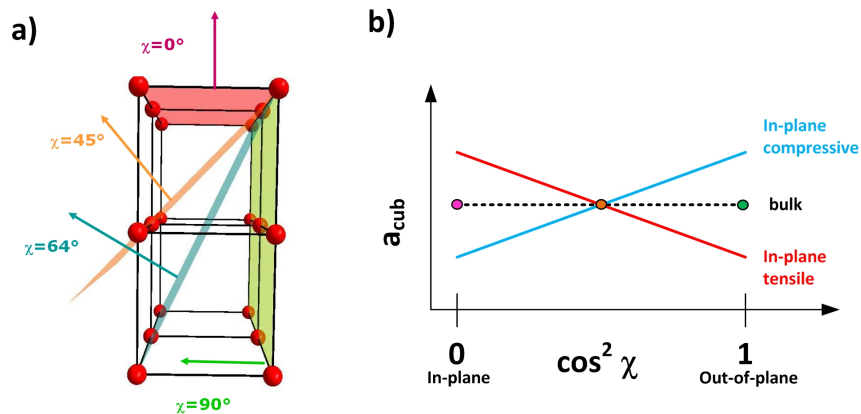


Figure 2.11: a) Sketch of differently tilted netplanes for Si(001) cubic structure b) Schematic illustration of the $\cos^2(\chi)$ plot for three different situations: fully relaxed, in-plan tensile and compressive strained layers.

Pole figure scan

A pole figure (PF) is measured at a fixed scattering 2θ angle (constant d spacing) and consists of a series of ϕ -scans (in-plane rotation around the center of the sample) at different tilt χ angles, as illustrated in Fig. 2.12. The power of this technique is thus to detect all possible orientations of a given lattice plane and detect for example microtwins.¹²²

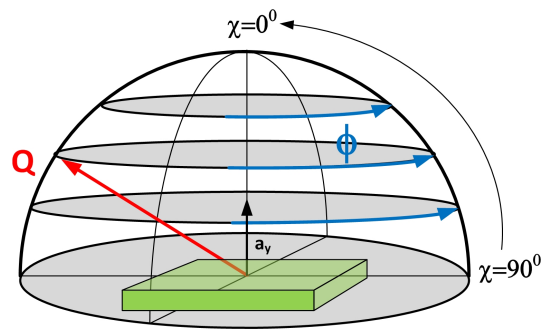


Figure 2.12: Course of the scattering vector Q during a pole figure measurement. (Figure adapted from Ref. 118)

Grazing incidence in-plane scan

In-plane scans are performed keeping the scattering vector Q perpendicular to the substrate normal. The X-rays impinge onto the specimen under grazing incident conditions with an angle α which typically varies between 0 and 0.6°. The diffraction pattern is obtained by rotating the sample by ϕ around its surface normal ([111] in case of Si(111) substrates), while the detector, lying just some tenths of degree (α) off the plane of the sample, simultaneously rotates by $2\theta - \chi - \phi$. Since the sample structure is always probed along Q in diffraction experiments, an in-plane scan probes the interplanar spacing of lattice planes perpendicular to the wafer surface. Figure 2.13 shows the geometry of a typical in-plane measurement.

The advantage of GI-XRD is its high surface sensitivity. In case of $\alpha < \alpha_c$, the substrate signal can be fully suppressed and by varying α , the epilayer structure can be non-destructively probed as a function of thickness.

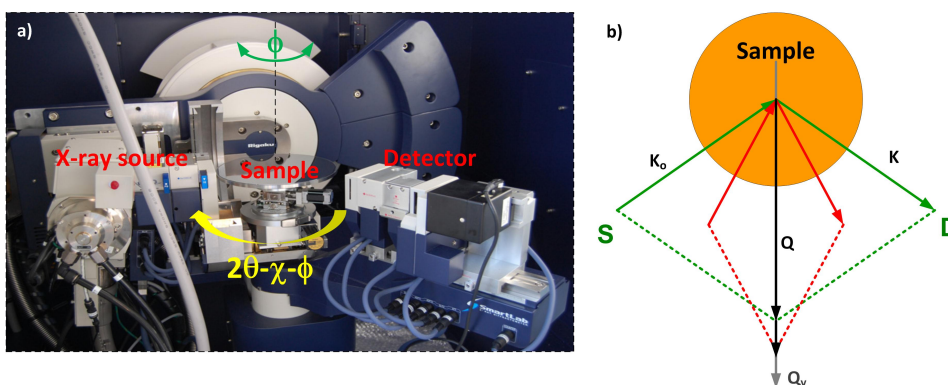


Figure 2.13: a) Rigaku SmartLab diffractometer during in-plane measurement b) definition of the in-plane scan.

Synchrotron Radiation Grazing Incidence X-ray diffraction

A part of the diffraction measurements was also performed at the insertion device beamline ID 32 at the European Synchrotron Radiation Facility (ESRF) in Grenoble. Synchrotron radiation (SR) is emitted by electrons travelling at velocities close to the speed of light along a circular orbit.¹²³ A facility for generating of SR consists of an electron accelerator, a storage ring, and so-called beamlines to which the experimental end-stations are attached.

SR offers many advantages over the conventional lab-based X-ray sources including:

- Experiments with varying energy (anomalous scattering etc.)
- High brilliance (higher sensitivity for weak signals)
- High resolution in energy, space and time

Grazing incidence XRD (GI-XRD) performed using SR is a powerful method to examine the growth of nanometer-scale thin film heterostructures. The X-ray penetration depth can be tuned (from micrometers to a few nanometers) by varying the angle of incidence to values below and above the critical angle for total reflection from the surface allowing for performing both bulk and surface sensitive measurements. In this way, the properties of very thin epitaxial layers can be selectively and non-destructively measured with a superior sensitivity and resolution.

2.2.2 X-ray reflectivity

X-ray reflectivity (XRR) is a non-destructive and non-contact method for a very precise thickness determination of layers and multilayer stacks (typically for laboratory-based X-ray set-ups in the range of about 2-500 nm). Additionally, it provides information about the surface and interface roughness and layer electron density.¹¹⁸ This method relies on a standard symmetric θ - 2θ measurement, but much smaller 2θ angles are used (usually in the range of 0-8°).

A XRR curve is generally presented as an intensity plot versus scattering angle 2θ . As an example, Fig. 2.14 a) depicts the XRR patterns from a bare Si substrate. Here, three different regions are clearly distinguishable: first one of increasing intensity, then an intensity plateau and finally a region of steeply

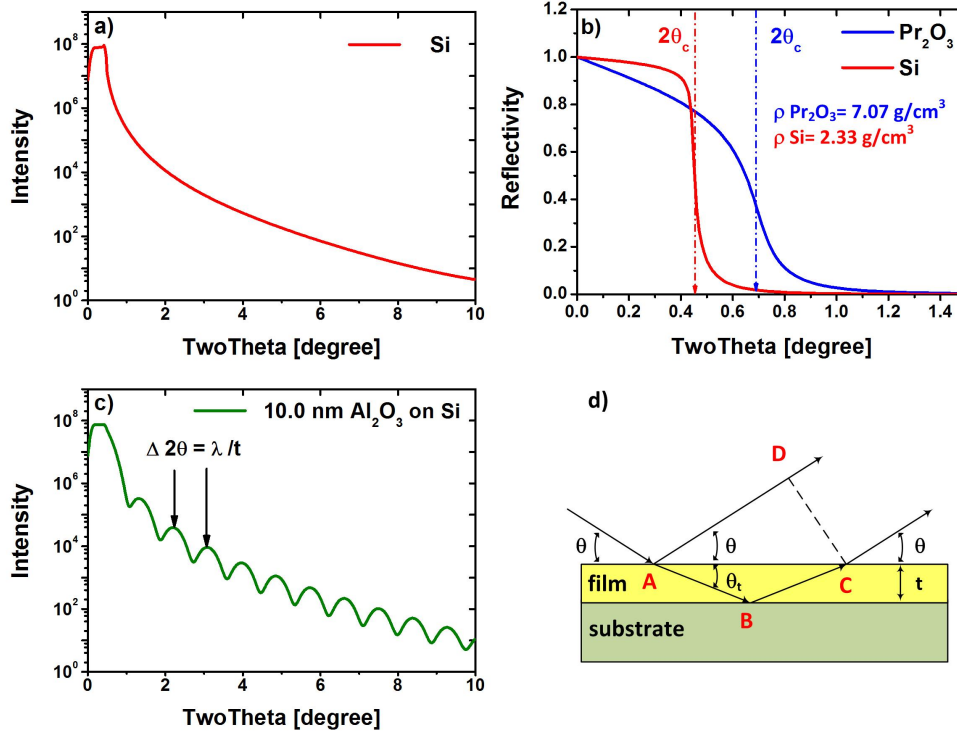


Figure 2.14: a) XRR scan from Si substrate b) XRR scan from two different materials: Si and Pr_2O_3 . The critical angle θ_c depends on the electron density c) XRR scan from $\text{Al}_2\text{O}_3/\text{Si}$ stack. Distance between two neighboring interference maxima contains information about oxide layer thickness d) Reflection of X-ray beam at the film surface and its interface with the substrate.

decreasing intensity over several orders of magnitude. The region of increasing intensity goes from an angle of incidence of almost 0° (configuration in which part of the beam is cut by the sample) to $\sim 0.2^\circ$ (whole photon flux impinge on the specimen). The plateau is caused by the total reflection of the primary beam, it is recorded for the angles up to the critical angle θ_c . θ_c depends on material: $\theta_c \uparrow$ when electron density $\rho \uparrow$ as shown in Fig. 2.14 b). Above the critical angle θ_c , the reflected intensity drops.

Recalling that for X-ray radiation the complex refractive index n has a real part smaller than 1 and can be written as: $n = 1 - \delta - i\beta$ and $\theta_c = \sqrt{2\delta}$ the XRR curve presented in Fig. 2.14 a) can be fitted using the following equation:

$$\frac{I_R}{I_0} = \left| \frac{\theta - \sqrt{\theta^2 - \theta_c^2 - 2i\beta}}{\theta + \sqrt{\theta^2 - \theta_c^2 - 2i\beta}} \right|^2 \quad (2.9)$$

Here, I_0 and I_R are called incident and reflected intensities, respectively. In

this way, δ and β can be estimated and, from those, the electron density ρ and attenuation length $1/\mu$ of the material, respectively.¹

Figure 2.14 c) shows the XRR scan for a 10 nm thick Al_2O_3 layer on a Si substrate. Noticable oscillations are so called Kiessig fringes. Oscillation maxima are observed whenever the phase difference Δ between the reflected and refracted beam, $\Delta = (\text{AB} + \text{BC})n - \text{AD}$, is a multiple of a wavelength λ (constructive interference, Fig. 2.14d). Careful analysis of Fig. 2.14 d) reveals that $\Delta = 2 \cdot t \cdot \sin \theta_t$, where t is the layer thickness and θ_t is the angle the transmitted wave forms with respect to the surface. The period of the interference fringes and the decay in the intensity are related to the thickness and roughness of the measured layer. From the analysis of the reflection using classical theory (Fresnel equation) one obtains the following expression for the film thickness t :

$$t \approx \frac{\lambda}{2\theta_{m+1} - 2\theta_m} \quad (2.10)$$

where $2\theta_{m+1} - 2\theta_m = \Delta 2\theta$ is the angular distance between two neighboring interference maxima. To obtain the thickness, a model is used to simulate the measured curve on the basis of the Fresnel equations. In the simulation of the spectra, the thickness of the layer, the surface roughness and the electron density are used as parameters, and fitted accordingly. Nowadays, most commonly recorded reflectivity curves are fitted with software. In this work, the program used for the evaluation of the XRR spectra is RCRefSim developed by P. Zaumseil.¹²⁴

XRR results are obtained using a Rigaku SmartLab diffractometer operating in parallel beam mode. The beam divergence in the scattering plane as low as 0.025° can be achieved by employing a mirror and a crystal collimator (Ge(400) two-fold channel-cut) at the X-ray source side. In addition, the smallest divergence slits should be used.

2.2.3 Reflection High Energy Electron Diffraction

Reflection High Energy Electron Diffraction (RHEED) is a technique for monitoring in situ the surface crystal structure and crystallographic orientation of thin films.^{125,126} In RHEED, a high energy electron beam (acceleration voltages $U=15.8$ kV) is directed onto the crystal surface under grazing inci-

¹electron density is expressed as: $\rho = \frac{\delta \cdot k^2}{2 \cdot \pi \cdot r_0}$ and attenuation length as $\frac{1}{\mu} = \frac{\lambda}{4 \cdot \pi \beta}$ where r_0 is the classical electron radius

dence. The angle of incidence ($\alpha \approx 2^\circ$) is arranged in such a way that the penetration depth is as small as possible and the influence of the surface on the resulting diffraction pattern is maximized. Due to the glancing incidence angle and the strong interaction of the electron and the atoms, only the top layer of the samples are probed (typical 2-3 monolayers). The crystal below the surface can be, in a first approximation, neglected. As the real space becomes a two dimensional mesh by this condition, the reciprocal space becomes a set of two dimensional rods oriented along the surface normal direction (z direction). Here, the concept of the Ewald sphere can be used to explain the diffraction pattern (Fig. 2.15).^{127,128} The origin of K space is placed at the physical spot on the sample's surface where the incidence electron beam arrives and from which the diffracted beams depart. The radius of the Ewald sphere is determined by the wavelength of the electron beam ($(2\pi/\lambda)$). As the wavelength of the electron beam is small, due to its high energy, the radius of the Ewald sphere is huge compared to the reciprocal lattice spacing. The reciprocal lattice rods intersecting the Ewald sphere will satisfy the diffraction condition (as discussed in the XRD part: $\mathbf{Q}_{hkl}=\mathbf{K}-\mathbf{K}_0=\mathbf{H}_{hkl}$, where $\mathbf{K}=\mathbf{K}_0$). As a result, the diffraction maxima are observed on the phosphorescent screen. Due to natural imperfections of the experiment (e.g. $\Delta \lambda$ of electron beam),

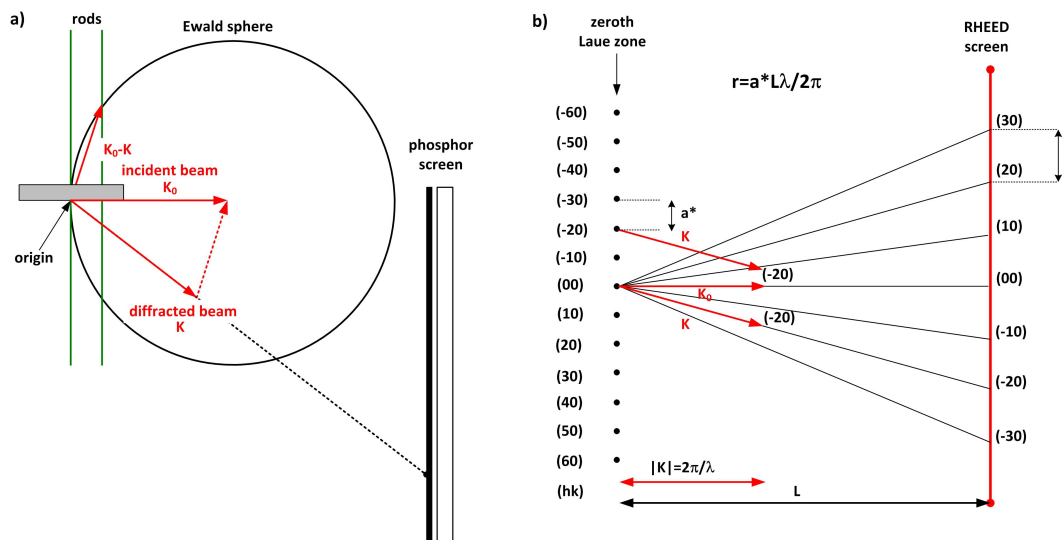


Figure 2.15: a) The Ewald sphere construction, shown in cross section in the plane of incidence. It is schematically demonstrated how a particular reciprocal lattice rod gives rise to a diffraction spot on the screen. The point of incidence of the beam is the origin of K space. b) The plan view showing the relation between the spacing of reciprocal lattice rods a^* and the spacing of observed RHEED streaks r .

the Ewald sphere is rather a spherical shell with a finite thickness. In addition, the rods of the reciprocal surface mesh exhibit a finite size due to limited long range order of the crystal surface. In consequence, the intersections of the finite crystal truncation rods on the surface mesh with the Ewald shell gives streaks (instead of sharp points) that are observable for atomically smooth single crystalline surfaces. The streak spacing corresponds to the lateral rod spacing for a particular azimuthal orientation of the sample with respect to incidence beam. Consequently, lattice constants can be easily derived from the analysis of the RHEED.

In addition, RHEED technique can be used to:

- calibrate the growth rate (periodic RHEED intensity oscillation corresponds to the monolayer deposition time)
- observe removal of oxides from the surface (e.g. clean Si(111) substrate results in Si(7x7) surface reconstruction after high temperature exposure)
- monitor arrangement of the surface atoms (GaN surface reconstruction provide information about the layer polarity)
- give a feedback on the surface morphology (transition from 2D layer to 3D island growth can be detected)
- provide information about growth kinetics
- determine the crystal structure (e.g. cubic and hexagonal structures can be easily distinguished), azimuthal alignment of the heterostructures and in-plane strain

The RHEED patterns presented in this study are measured with a Staib Instruments of the RHEED 30WSI type. Identical RHEED set-ups are installed in the oxide as well as in the GaN chamber of IHP's DCA MBE equipment.

2.2.4 X-ray Photoelectron Spectroscopy

X-ray Photoelectron Spectroscopy (XPS), also called Electron Spectroscopy for Chemical Analysis (ESCA), is the most widely used surface analysis technique to provide both quantitative atomic concentration and chemical state information of the detected elements.^{129, 130, 131}

The physics behind XPS is based on the photoelectric effect i.e. the ejection of an electron from a core level of an atom by an X-ray photon of energy $h\nu$

(Fig. 2.16 a)). In this process, an incidence photon transfers its entire energy to the bound electron, and element identification is provided by the measurement of the kinetic energy of the electrons that escape from the sample by the energy analyzer. To calculate the binding energy (BE) of the electrons from the measured kinetic energy (KE), the Einstein equation¹³² can be used:

$$BE = h\nu - KE - \phi \quad (2.11)$$

where ϕ is the spectrometer work function and $h\nu=1253.6$ eV in case of Mg K_{α} radiation. The XPS spectrum (intensity as a function of BE) will reproduce the chemical structure of surface accurately, since all the electrons with $BE < h\nu - \phi$ will be detected in the spectrum.

The BE of the photoelectrons is related to the atomic and molecular environ-

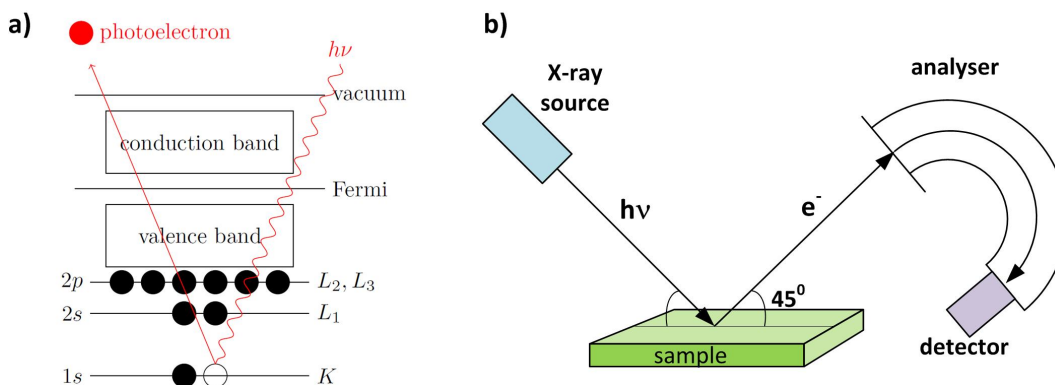


Figure 2.16: a) Sketch of the XPS process, showing ejection of electron from a core level of an atom by X-ray photon b) The principle of a XPS experiment.

ment from which they originated. Thus, accurate measurement of the energetic peak position of the elements gives information not only about elements in a thin film but also about the chemical state of these elements. The number of detected electrons is a measure for the elemental concentration. In order to obtain quantitative results, peak shape and intensity is fitted with a software (e.g. CasaXPS) and further analyzed according to the theory of quantitative XPS.

XPS is a surface sensitive method, due to the short inelastic mean free path (IMFP) of the photoelectrons.¹³³ IMFP is a measure of the average distance travelled by an electron through a solid before it is inelastically scattered. The created photoelectrons can travel a distance, characterized by the sampling depth ($\sim 3 \times \text{IMFP}$) in the matrix, of only few nm, before being completely absorbed and appear no longer in the XPS spectra.

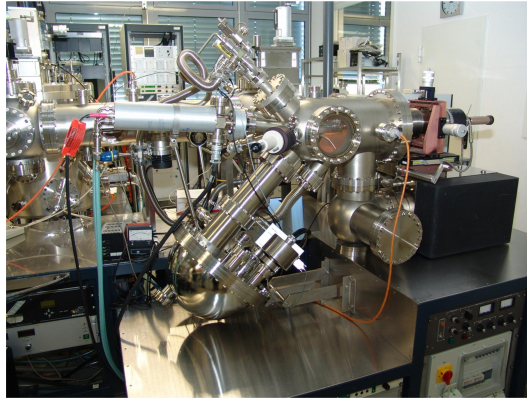


Figure 2.17: Photograph of the XPS tool integrated into the MBE facility. The emitted photoelectrons are collected by a Scienta Phoibos 100 hemispherical energy analyzer.

2.2.5 Scanning Electron Microscopy

In a Scanning Electron Microscopy (SEM), the sample is scanned with a highly focused electron beam with high energy. The energy ranges from 100 eV to several 100 keV. As a result of the electron irradiation, several phenomena occur in the sample. For instance, elastically and inelastically scattered electrons, called back-scattered electrons (BSE) and secondary electrons (SE), respectively, and X-rays are emitted from the surface and can be detected by suited detectors (Fig. 2.18 a)). Different materials generate different SE yields and, consequently, different contrast in a SEM image. Hence, the thickness of a layer can be determined when a cross-section analysis is performed. Moreover, for a fixed material the SE yield varies also as a function of the surface morphology. Therefore, the presence of irregularities with size down to few nm on the surface (e.g. surface roughness, defects etc.) can be detected. In order to determine the distribution of different elements in the sample, the BSE signal should be measured. This is due to the fact that the BSE signal is strongly related to the atomic number (Z) of the specimen.

Finally, characteristic X-rays are emitted when the electron beam removes an inner shell electron from the sample, causing a higher energy electron to fill the hole and release energy. These characteristic X-rays fluorescence signals are used to identify the composition and measure the abundance of elements in the sample down to the atomic % level. The technique is called energy dispersive X-ray (EDX) spectroscopy. More details about SEM theory can be found in Ref. 134. The instrument available at the IHP laboratories is a Hitachi S-4500 operating in HV (Fig. 2.18 b)).

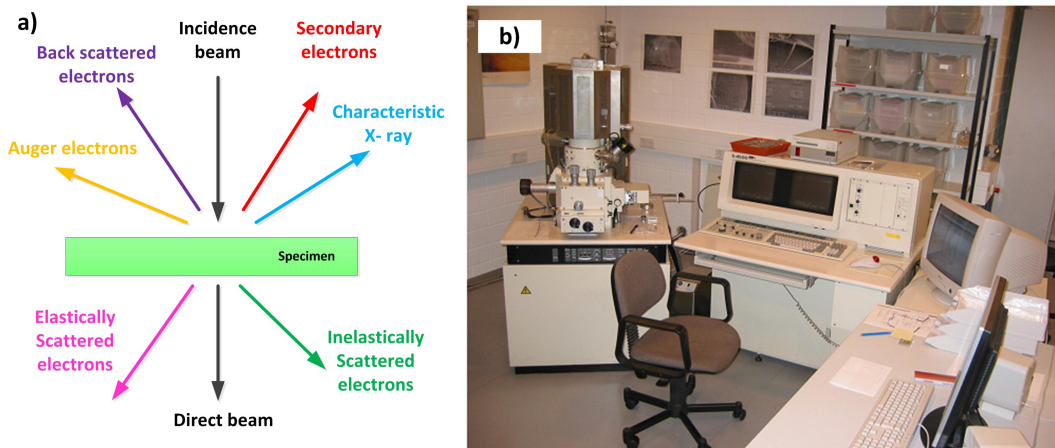


Figure 2.18: a) Signals originating from a specimen exposed to a high energy electron beam b) Photograph of the Hitachi S-4500 scanning electron microscope available at the IHP laboratories.

2.2.6 Transmission Electron Microscopy

Transmission electron microscopy (TEM) is the prominent method in material science for the imaging of the crystal morphology, the crystal phases, as well as dislocations and defects, as it allows for high resolution atomic lattice imaging.¹³⁵ However, to study the sample in transmission by electron beams, the sample must be prepared in form of thin lamella, only a few nanometers thick. Similar to SEM, in TEM a high energy electron beam (energy in the range from 20 to 300 keV) is focused on the sample. The electrons exiting the material are either backward (described in previous section) or forward scattered (Fig. 2.18 a)). The forward scattered beam is made of electrons which are not scattered, or are scattered inelastically or elastically. The first group consists of electrons that did not interact with the specimen. Their transmission decreases as the sample thickness increases. As a result, thicker regions correspond to darker images whereas thinner regions correspond to brighter images. Similar rule holds for materials of different density. Inelastically scattered electrons can be investigated by so-called electron energy loss spectroscopy (EELS). The elastically scattered electrons conserve their energy and momentum and give rise to the contrast in TEM images. Provided that the specimen is crystalline, those electrons are diffracted by the crystal lattice and form, similar to XRD, a diffraction pattern used further to analyse the material structure.

A microscope combining the principles used by both TEM and SEM is usually referred to as scanning transmission electron microscopy (STEM).

The TEM images presented in this thesis were obtained using either a Philips CM 300 (300 keV) or a Philips CM 200 (200 keV) microscope. In some cases, a FEI Tecnai Osiris microscope was used (STEM).

2.2.7 Photoluminescence

Photoluminescence (PL) spectroscopy is a contactless, non-destructive method which provides information about the optoelectronic properties of the probed material.¹³⁶ PL is based on the emission of light by a semiconductor sample when it is photo-excited by means of monochromatic light with well-know energy. In this process, absorbed light (with energy greater than the bandgap) creates the electron-hole pairs. Electrons are excited to the conduction band

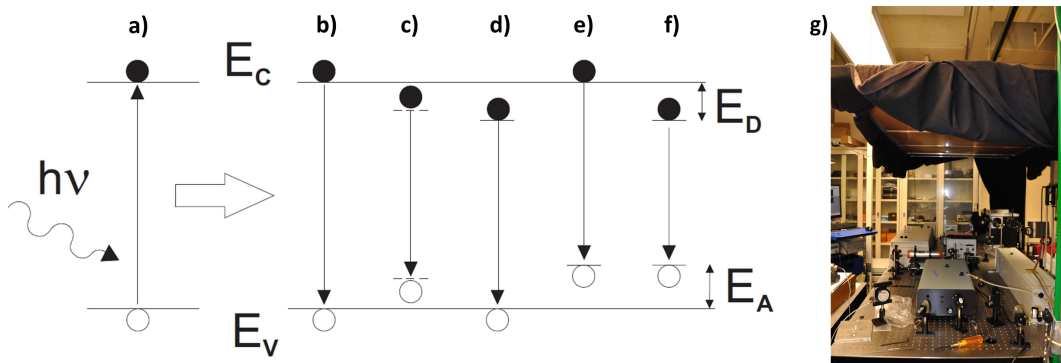


Figure 2.19: a) Generation of the electron-hole pair after the absorption of a photon $h\nu$. Radiative transitions: b) band-to band recombination c) excitonic recombination d) donor to valence band recombination e) conduction band to acceptor recombination f) donor-acceptor recombination g) Photoluminescence spectroscopy laboratory at Virginia Commonwealth University.

or to energy states within the bandgap (different energy states are produced by different defects and impurities which are incorporated into the lattice).¹³⁷ Photons, produced as a result of the various recombinations of electrons and holes, are emitted from the sample and afterwards analyzed. The most commonly observed PL transitions are schematically shown in Fig.2.19. PL is mainly used for:

- **Band gap determination:** the spectral distribution of PL from a semiconductor can be analysed to determine the electronic band gap. Near-band edge PL peak position provides also information about the strain

in the layer. This is the result of the fact that the strain changes lattice spacing and the size of the band gap.

- **Impurity levels and defect detection:** the PL spectrum at low sample temperatures often reveals spectral peaks associated with impurities contained within the host material. The high sensitivity of this technique provides the potential to identify extremely low concentrations of intentional and unintentional impurities that can strongly affect material quality and device performance.
- **Recombination mechanisms:** the quantity of PL emitted from a material is directly related to the relative amount of radiative and non-radiative recombination rates. Non-radiative rates are typically associated with impurities and thus, this technique can qualitatively monitor changes in material quality as a function of growth conditions. To measure radiative recombination rates, time-resolved PL (TRPL) is usually used.

PL measurements were performed at Virginia Commonwealth University in Richmond (Fig. 2.19 g)). Near band edge PL was measured using above band gap excitation (325 nm with a power at the sample of 25 mW) from a Helium-Cadmium laser (He-Cd). For temperature dependent PL measurements, samples were attached to a copper sample holder and placed inside a closed-cycle He refrigerator with a temperature variation from 10 to 320 K. A temperature controller enabled to stabilize the temperature to within 0.1 K.

Chapter 3

Results

3.1 Growth characteristics of the oxide buffer

3.1.1 *In-situ* RHEED study

Structural characteristics of the $\text{Sc}_2\text{O}_3/\text{Y}_2\text{O}_3$ films grown on Si substrates were investigated *in-situ* using RHEED. Deposition of the first buffer layer, Y_2O_3 , was always performed on clean atomically flat, (111) oriented Si wafers. The typical RHEED pattern of the starting Si(111) surface taken along $\{\bar{1}10\}$ azimuth is shown in Fig. 3.1 a). During Y_2O_3 growth the RHEED pattern changes gradually from the (7×7) reconstructed Si(111) surface to the streaky pattern characteristic for the growth of flat, single crystalline oxide layers. Figures 3.1 b) and c) display RHEED images of the (111) surface of the $\text{Y}_2\text{O}_3/\text{Si}(111)$ system recorded with the electron beam aligned along $\{\bar{1}10\}$ and $\{11\bar{2}\}$ direction, respectively. The weak substreaks highlighted by the white lines correspond to a (4×4) overstructure of the Y_2O_3 surface unit cell with respect to the Si surface unit cell. This is true because the surface of (111) oriented bixbyite oxide structure like Y_2O_3 is about four times bigger than the Si(111) surface unit mesh dimension, as discussed in detail, for example in Ref. 138. The recorded rod distance X_1 and X_2 in the reciprocal space is inversely proportional to d spacing in the $\{11\bar{2}\}$ and $\{\bar{1}10\}$ direction, respectively. The obtained $1/X_1$ distance of about 3.25 \AA corresponds to three times Y_2O_3 d_{448} . This is also the distance between two oxygen (yttrium) atoms in the Y_2O_3 crystal in $\{11\bar{2}\}$ direction, as shown in Fig. 3.1 d). Similarly, $1/X_2$ of about 1.87 \AA defines the interval between two oxygen (yttrium) atoms in Y_2O_3 crystal in the $\{\bar{1}10\}$ direction (Fig. 3.1 e)). The calculated d spacing values correspond well to bulk values and Y_2O_3 is thus fully relaxed.

Due to the fact that Y_2O_3 and Sc_2O_3 have the same crystal structure, the

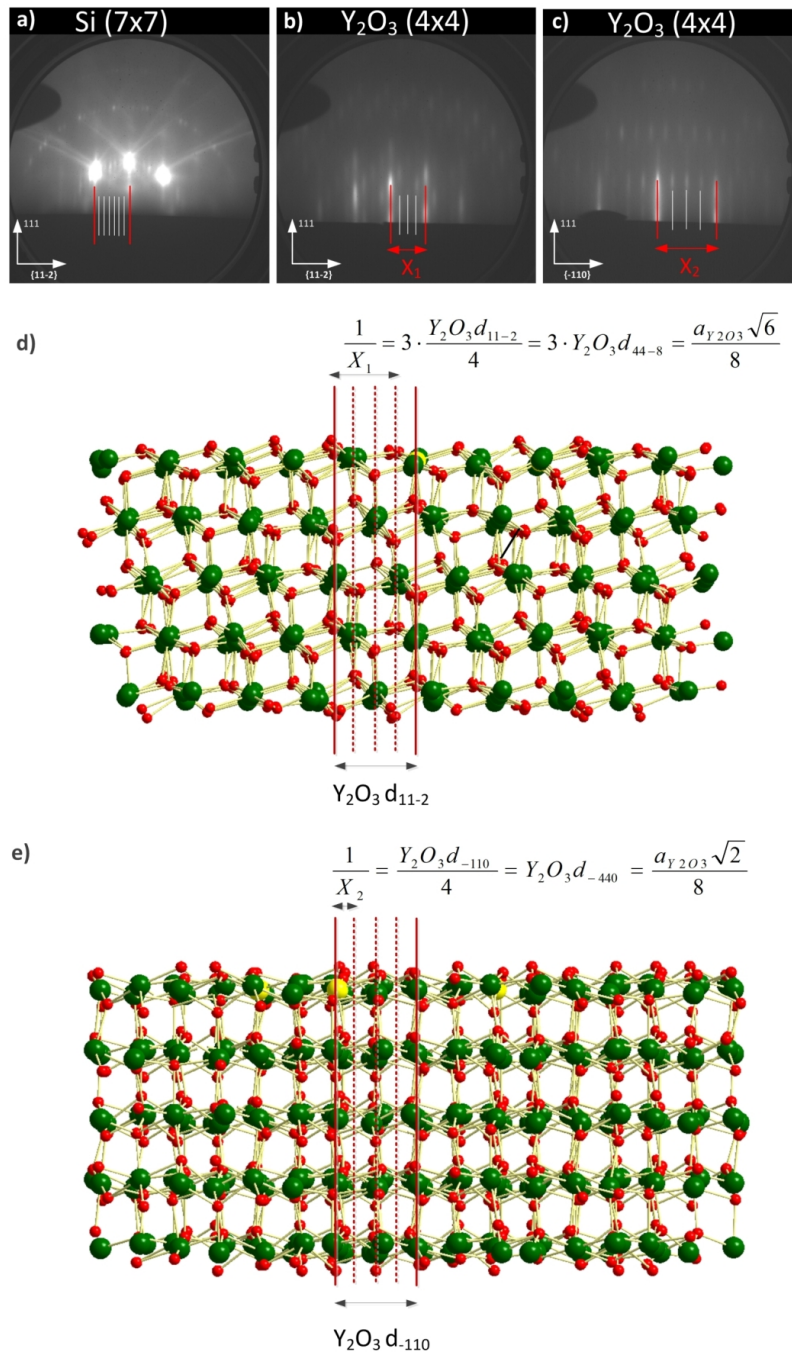


Figure 3.1: RHEED images of the a) Si surface taken along $\{\bar{1}10\}$ and Y_2O_3 surface taken along b) $\{\bar{1}10\}$ and c) $\{11\bar{2}\}$. Rod distance X_1 and X_2 are inversely proportional to the real d spacing in d) $\{11\bar{2}\}$ and e) $\{\bar{1}10\}$ direction, respectively.

RHEED pattern of the Sc_2O_3 layer grown on $\text{Y}_2\text{O}_3/\text{Si}(111)$ is similar to the RHEED pattern obtained for Y_2O_3 (Figs. 3.1 b) and c)). The only difference is the rod distance X_1 and X_2 which is the result of different lattice parameter of Sc_2O_3 ($a=9.85 \text{ \AA}$) and Y_2O_3 ($a=10.60 \text{ \AA}$). The obtained $1/X_1$ and $1/X_2$ values of 3.02 \AA and 1.74 \AA stand for the fully relaxed Sc_2O_3 layer on $\text{Y}_2\text{O}_3/\text{Si}(111)$ templates.

Additionally, based on the RHEED observations the epitaxial relationship of the heterostructure can be determined:

$$\text{Sc}_2\text{O}_3(111),\{\bar{1}1\bar{2}\} \parallel \text{Y}_2\text{O}_3(111),\{\bar{1}1\bar{2}\} \parallel \text{Si}(111),\{\bar{1}1\bar{2}\}$$

which is in a good agreement with the XRD studies presented below.

3.1.2 Crystalline properties

Vertical growth orientation

In order to determine the growth orientation of the $\text{Sc}_2\text{O}_3/\text{Y}_2\text{O}_3/\text{Si}(111)$ structure, a specular θ - 2θ XRD scan over an angular 2θ range from 20° to 80° was performed (Fig. 3.2 a)). Bragg peaks originating from the oxides and the Si substrate are indicated by the dashed lines. (111) diffraction peaks of different order n are clearly seen for Si substrate ($n=1, 2$) as well as for the Y_2O_3 and Sc_2O_3 layers ($n=2, 4$). No additional reflections originating from the oxide buffer are detected which indicates that Y_2O_3 and Sc_2O_3 layers are single crystalline. In agreement with the RHEED study, the epitaxial relationship along the growth orientation is:

$$\text{Sc}_2\text{O}_3(111)/\text{Y}_2\text{O}_3(111)/\text{Si}(111)$$

In this particular case, the Y_2O_3 and Sc_2O_3 layer thicknesses are 8 nm and 6 nm, respectively. Based on the $\text{Y}_2\text{O}_3(444)$ ($2\theta=60.3^\circ$) and $\text{Sc}_2\text{O}_3(444)$ ($2\theta=65.6^\circ$) Bragg peak positions the unit cell parameters were calculated using the following equation:

$$d = \frac{\lambda}{2 \cdot \sin \theta} \quad (3.1)$$

and for a cubic crystal structure:

$$a = d \cdot \sqrt{h^2 + k^2 + l^2} \quad (3.2)$$

where, $\lambda=1.54 \text{ \AA}$ is the wavelength of the X-ray source, θ is the Bragg angle and h, k, l are the Miller indices. The unit cell parameters for Y_2O_3 and Sc_2O_3

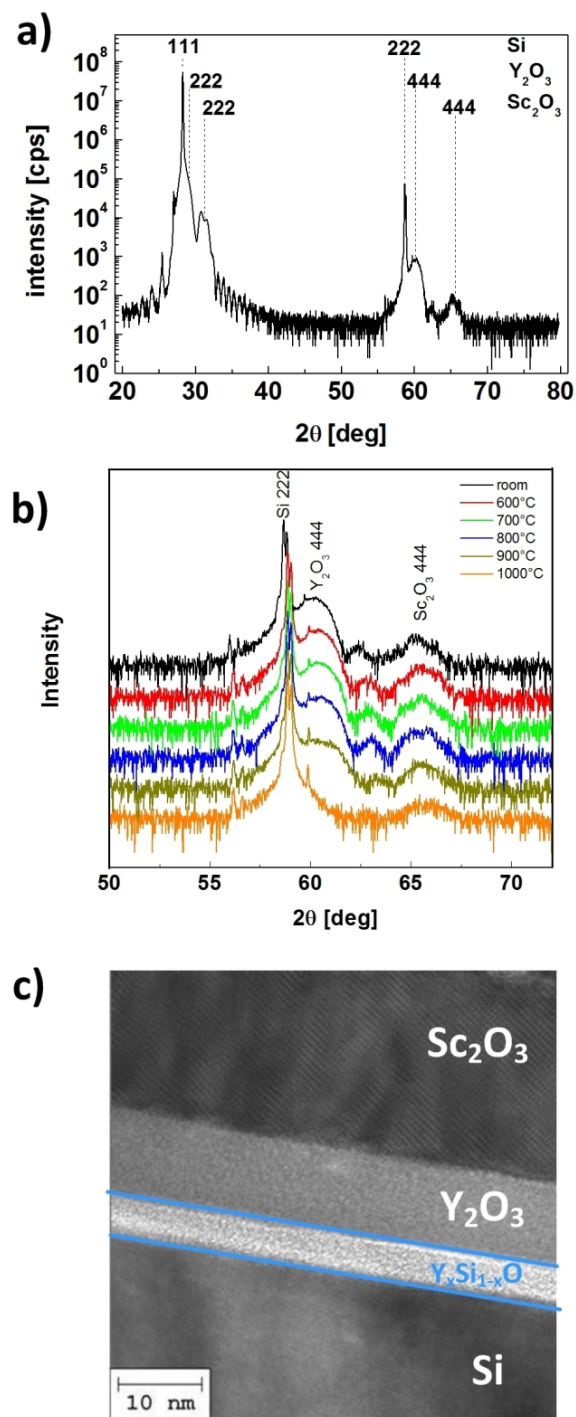


Figure 3.2: a) Long range XRD specular θ - 2θ scan and b) thermal stability experiments on a $Sc_2O_3/Y_2O_3/Si(111)$ heterostructure. XRD measurements were performed in the parallel beam configuration of the diffractometer. 5° soller slits were used on the X-ray source and the detector site. c) TEM cross-section of a $Sc_2O_3/Y_2O_3/Si(111)$ heterostructure annealed in 1 bar N_2 at 1000°C for 30 min.

obtained in this way are 10.60 Å and 9.85 Å, respectively, and agree with a fully relaxed cubic lattice.

Thermal stability of the oxide buffer

The thermal stability of the $\text{Sc}_2\text{O}_3/\text{Y}_2\text{O}_3/\text{Si}(111)$ heterostructure was investigated by means of XRD specular θ - 2θ measurements. Samples were treated in a furnace in 1 bar nitrogen for 30 min at temperatures ranging from 600 to 1000°C. As can be seen from Fig. 3.2 b), the $\text{Sc}_2\text{O}_3(444)$ reflection is present up to 1000°C, whereas the $\text{Y}_2\text{O}_3(444)$ Bragg peak remains visible only up to 900°C. At 1000°C the Y_2O_3 film gets amorphous, probably because of the interaction with the Si substrate to form $\text{Y}_x\text{Si}_{1-x}\text{O}$ (TEM cross section in Fig. 3.2 c))[Ref. 139]. It is thus concluded that the oxide heterostructure is stable at least up to 900°C. This temperature is sufficiently high to enable GaN overgrowth of the oxide buffer by MBE.

Stacking configuration and in-plane alignment

The out-of plane Phi (Φ) scans shown in Fig. 3.3 were carried out across $\text{Si}\{\bar{1}11\}$, $\text{Y}_2\text{O}_3\{\bar{2}22\}$, and $\text{Sc}_2\text{O}_3\{\bar{2}22\}$ reflections to determine the stacking configuration of the heterostructure. These measurements were accomplished by fixing the diffraction angle 2θ and the inclination angle χ to the desired reflection and performing in-plane 360°scans around the $\text{Si}[111]$ surface normal. The threefold off-plane symmetry of the $\text{Si}(111)$ and cubic (111) oxide films is evident from the observed 120°spacing between Si and oxides reflections, respectively. Furthermore, the 60°offset between $\text{Si}\{\bar{1}11\}$, $\text{Y}_2\text{O}_3\{\bar{2}22\}$ and $\text{Sc}_2\text{O}_3\{\bar{2}22\}$ Bragg peaks indicate that the oxides grow epitaxially on $\text{Si}(111)$ with a type-B orientation.¹⁴⁰ Here, it is recalled that type-A denotes a (111)-oriented fcc-like epilayer, whose (111) planes exhibit the same stacking vector as the $\text{Si}(111)$ substrate. On the contrary, type-B refers to the case in which a stacking fault at the epilayer/ $\text{Si}(111)$ interface rotates the stacking vector in the growing film by 180°around the $\text{Si}(111)$ surface normal. In addition, based on the Φ scan the epitaxial in-plane alignment of the heterostructure is determined to be:

$$\text{Sc}_2\text{O}_3[2\bar{1}\bar{1}]||\text{Y}_2\text{O}_3[2\bar{1}\bar{1}]||\text{Si}[\bar{2}11]$$

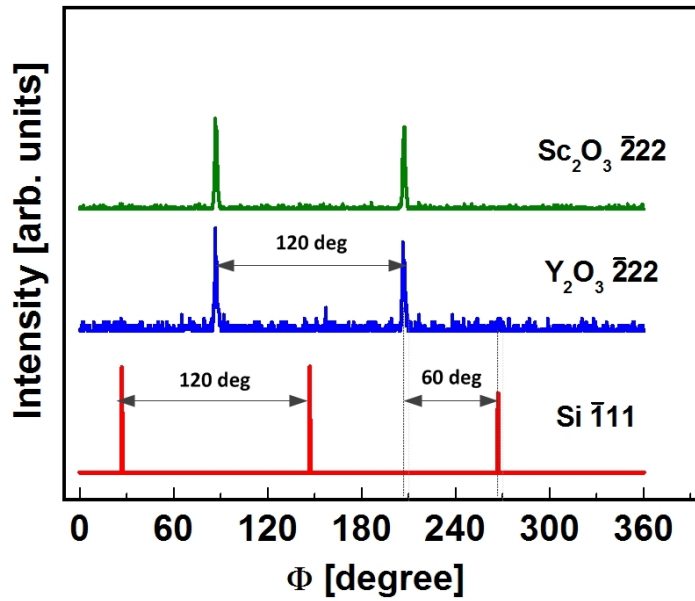


Figure 3.3: Φ scans across $\text{Sc}_2\text{O}_3\{\bar{2}22\}$ ($\chi=70.5^\circ$, $2\theta=31.5^\circ$), $\text{Y}_2\text{O}_3\{\bar{2}22\}$ ($\chi=70.5^\circ$, $2\theta=29.1^\circ$), and $\text{Si}\{\bar{1}11\}$ ($\chi=70.5^\circ$, $2\theta=28.4^\circ$) reflections.

It is noted that this XRD result corresponds to the RHEED study presented above.

3.1.3 Strain state of the oxide bi-layer

The strain state of the oxide bi-layer was investigated by means of an XRD technique which identifies the presence of tetragonal distortions in the heteroepitaxially grown cubic layers. This method, the so-called χ scan, was introduced in the Experimental part of this thesis. Figure 3.4 shows the results of such analysis for the $\text{Sc}_2\text{O}_3/\text{Y}_2\text{O}_3$ buffer layer system. The in-plane a_{\parallel} and out-of-plane a_{\perp} lattice parameters can be extracted by intercepting the linear regression of such experimental points at $\cos^2(\chi)=0$ and 1, respectively. The Si, $1/2$ Y_2O_3 , and $1/2$ Sc_2O_3 cubic bulk lattice constant values are marked by black, blue and orange horizontal solid lines, respectively. It can be seen that the a_{\parallel} and a_{\perp} lattice parameters for 6 nm thick Y_2O_3 layer are within experimental error of the same value and very close to the bulk lattice constant. Similar behaviour is observed for the 20 nm thick Sc_2O_3 . This implicates that the Y_2O_3 and Sc_2O_3 films are fully relaxed within experimental error. The lack of strain in especially the Sc_2O_3 layer indicates two results:

- Firstly, the fully relaxed Sc_2O_3 film on $\text{Y}_2\text{O}_3/\text{Si}(111)$ support achieves

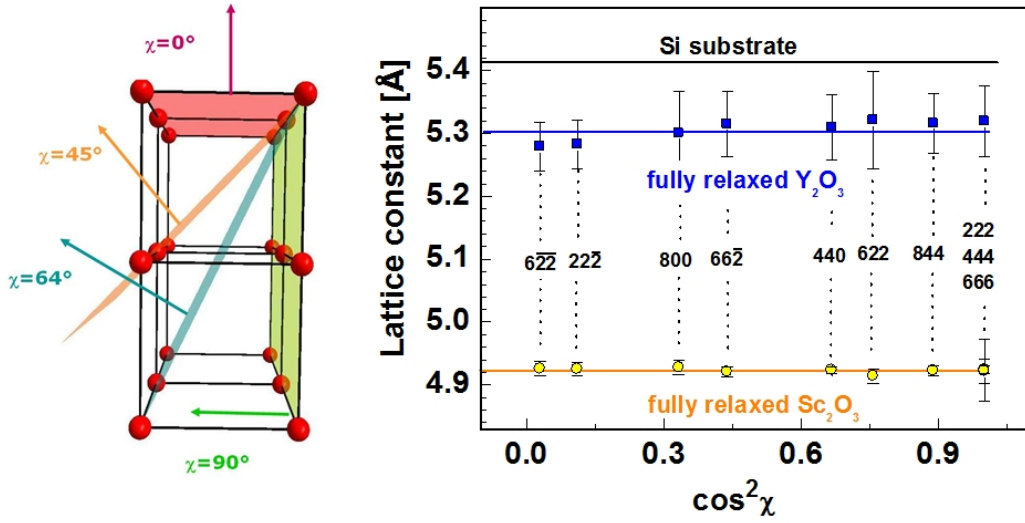


Figure 3.4: Experimentally determined Y_2O_3 and Sc_2O_3 strain characteristics as a function of $\cos^2 \chi$. The Si, Y_2O_3 , and Sc_2O_3 bulk lattice constant values are marked by horizontal solid lines (for better comparison, lattice constants of Y_2O_3 and Sc_2O_3 are divided by two).

its bulk unit cell constant so that the lattice misfit between GaN and Sc_2O_3 is reduced to the smallest possible value.

- Secondly, the theoretical lattice mismatch of -7% between the oxide layers has to be relaxed by the formation of a network of misfit dislocations (MD) at the oxide/oxide interface.

The formation mechanism of MDs at the $\text{Sc}_2\text{O}_3/\text{Y}_2\text{O}_3$ interface is illustrated by the TEM image shown in Fig. 3.5. To accommodate the difference in the lattice constants between Y_2O_3 and Sc_2O_3 , for every 10 Y_2O_3 atomic planes 11 atomic planes of the smaller Sc_2O_3 lattice are formed in the $\langle 11\bar{1} \rangle$ direction during growth. The additional Sc_2O_3 plane becomes the centre of the edge dislocation. The vernier period of dislocation p is about 2.5 nm which is in good agreement with theoretical calculations for a fully relaxed $\text{Sc}_2\text{O}_3/\text{Y}_2\text{O}_3$ heterostructure $p = (a_{\text{Y}_2\text{O}_3} \cdot a_{\text{Sc}_2\text{O}_3}) / (a_{\text{Y}_2\text{O}_3} - a_{\text{Sc}_2\text{O}_3})$.¹⁰⁷

The TEM cross section confirms also that the buffer oxides are type-B with respect to the Si substrate (as it was previously derived from the Φ scans in Fig. 3.3). This can be seen from the stacking faults at the $\text{Y}_2\text{O}_3/\text{Si}(111)$ boundary (green arrows), as explained in more detail in Ref. 141. Finally, based on the TEM image shown in Fig. 3.5 it is concluded that no interface

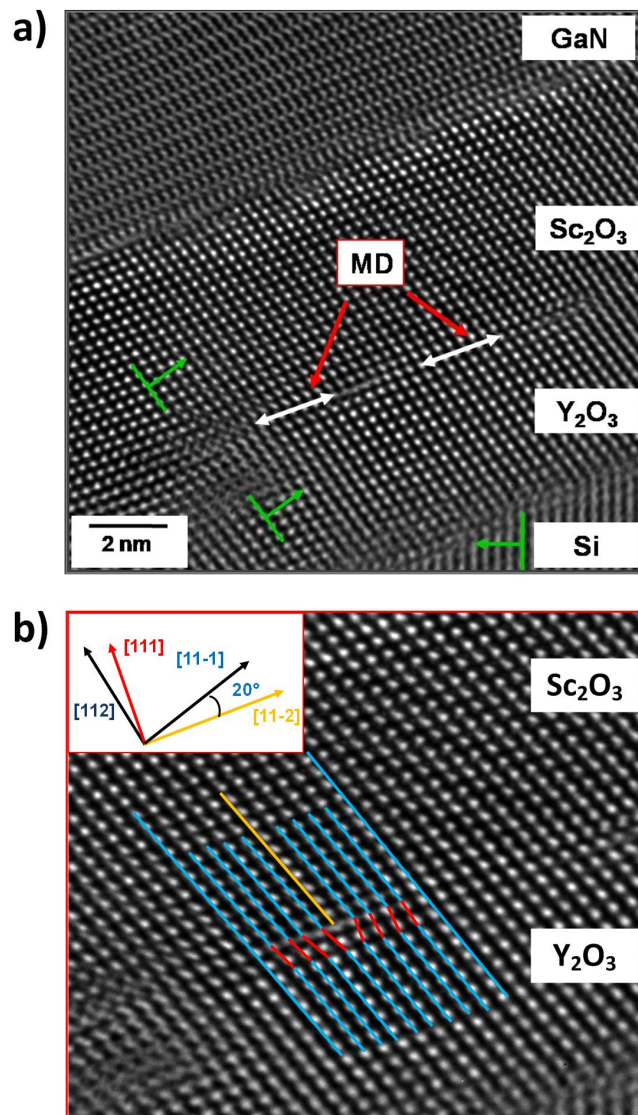


Figure 3.5: TEM cross-section of the as-grown Sc₂O₃(111)/Y₂O₃(111)/Si(111) heterostructure, viewed along an $\langle\bar{1}10\rangle$ azimuth. a) Misfit dislocations (MDs) at the interface between Sc₂O₃/Y₂O₃; b) Edge dislocation structure.

reactions took place between Si and Y₂O₃ and between both buffer oxide layers.

3.1.4 Defect structure

In the oxide heterostructures previously studied within the Siltronic-IHP project, a high number of structural defects across the oxide $\{\bar{1}11\}$ netplanes was observed.¹⁴² An example is given by cubic Pr₂O₃ on Si(111). The RSM of the Pr₂O₃($\bar{2}22$) Bragg peak highlights the presence of a streak of diffuse scatter-

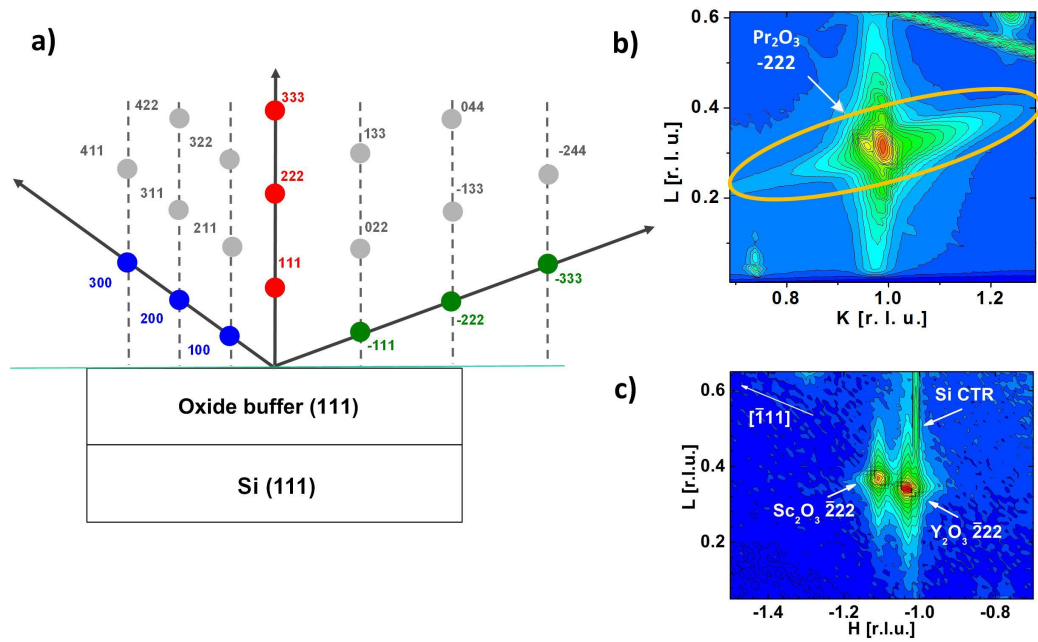


Figure 3.6: Synchrotron-based XRD measurements a) Sketch of the oxide Bragg peak distribution; RSMs around the $(\bar{2}22)$ Bragg peaks of b) cubic $\text{Pr}_2\text{O}_3(111)/\text{Si}(111)$ and c) $\text{Sc}_2\text{O}_3(111)/\text{Y}_2\text{O}_3(111)/\text{Si}(111)$ heterostructures for comparison.

ing along a $\langle\bar{1}11\rangle$ direction (Fig. 3.6 b)). Such a streak is not expected for an ideally perfect material and originates from the interruption of the long-range order of crystallinity across the oxide $\{\bar{1}11\}$ netplanes due to defects. These defects were identified by combined XRD and TEM as microtwins and stacking faults.¹²² A similar experiment was carried out for a 20 nm $\text{Sc}_2\text{O}_3(111)/35$ nm $\text{Y}_2\text{O}_3(111)/\text{Si}(111)$ heterostructure and the result is given by the plot in Fig 3.6 c). From the comparison with the cubic $\text{Pr}_2\text{O}_3(2\bar{2}2)$ RSM, it can be stated that no diffuse scattering streaks are present in the $\text{Sc}_2\text{O}_3/\text{Y}_2\text{O}_3$ bi-layer. This means that, the density of extended defects in the $\{\bar{1}11\}$ slip planes of the oxide thin film structure (e.g. stacking faults) is below the detection limit even of modern 3rd generation synchrotron highly sensitive XRD studies. This study demonstrates that the novel engineered $\text{Sc}_2\text{O}_3/\text{Y}_2\text{O}_3$ buffer approach on $\text{Si}(111)$ provides a template of high structural quality for GaN overgrowth.

3.1.5 Summary

In summary, single crystalline (111) oriented $\text{Sc}_2\text{O}_3/\text{Y}_2\text{O}_3$ buffers were obtained on Si(111) substrates. The Y_2O_3 and Sc_2O_3 films are of type-B stacking orientation with respect to the Si(111) substrate and are fully relaxed for layer thicknesses above 10 nm. The 7% lattice mismatch between the oxides is compensated by edge dislocations formed by insertion of additional {111} planes in the Sc_2O_3 thin film. Diffuse x-ray scattering studies using a 3rd generation synchrotron source prove that densities of extended structural defects of preferred {111} orientation in the Sc_2O_3 layer are below the detection limit. In conclusion, the novel engineered $\text{Sc}_2\text{O}_3/\text{Y}_2\text{O}_3$ buffer approach results in fully relaxed Sc_2O_3 films of high structural quality for GaN overgrowth. Additionally, thermal stability tests shows that the oxide buffer is stable at least up to 900°C which is sufficiently high for the "proof of principle" MBE GaN growth experiments.

3.2 Thin GaN on Sc₂O₃/Y₂O₃/ buffer on Si(111)

Thin GaN layers described in this section were grown on Sc₂O₃/Y₂O₃/Si(111) templates under the following conditions: 650 °C substrate temperature, 910 °C Ga K-cell temperature, 10⁻⁵ mbar chamber pressure, 250 W power of the RF plasma source. The growth was monitored *in-situ* by RHEED and the resulting layers were characterized *ex-situ* by XRR, XRD, SR-XRD, and TEM.

3.2.1 Layer morphology and epitaxial relationship

XRR and specular θ - 2θ XRD

Figure 3.7 shows XRR and XRD scans performed in the specular θ - 2θ geometry on the GaN/Sc₂O₃/Y₂O₃/Si(111) heterostructure. XRR oscillations (Fig. 3.7 a)) for the selected sample can be very well fitted using a three layer model (GaN/Sc₂O₃/Y₂O₃) without any transition regions. This result indicates that the GaN film is closed and of only limited roughness. Extracted layer thicknesses and relative electron densities are indicated in the inset to Fig. 3.7 a) (dashed lines denote Y₂O₃, Sc₂O₃ and GaN bulk densities). For this particular sample, the obtained Y₂O₃, Sc₂O₃ and GaN layer thicknesses are 5, 25 and 30 nm, respectively. The GaN surface roughness is about 1.5 nm.

To determine the growth orientation of the heterostack, a specular θ - 2θ XRD scan over an angular 2θ range from 20° to 130° was performed (Fig. 3.7 b)). Peak positions are indicated by the dashed lines. (111) diffraction peaks of different order n are clearly seen for the Si substrate ($n = 1, 2, 3$) and for the Y₂O₃ and Sc₂O₃ layers ($n = 2, 4, 6$). In addition, all detected GaN reflections can be assigned to (000 n ; $n = 2, 4, 6$) Bragg peaks of the hexagonal phase of GaN. This proves that the hexagonal phase of GaN can be grown on the Sc₂O₃/Y₂O₃ buffer and the extracted epitaxial relationship along the growth direction is:

$$\text{GaN}(0001)/\text{Sc}_2\text{O}_3(111)/\text{Y}_2\text{O}_3(111)/\text{Si}(111)$$

The unit cell parameters, calculated from the Y₂O₃(444) and Sc₂O₃(444) peak positions, agree with fully relaxed cubic lattices and are 10.64 Å and 9.85 Å, respectively. The GaN lattice parameter c extracted from the GaN(0004) reflection is 5.18 Å, a value slightly smaller than the bulk one (5.19 Å). This behaviour is possibly caused by an in-plane tensile strain in the GaN film, as discussed in more detail below.

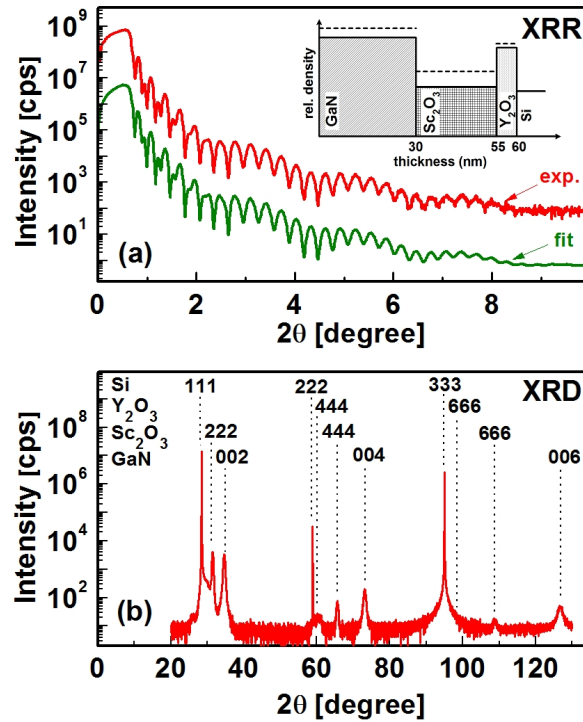


Figure 3.7: a) Measured (top) and fitted (bottom) XRR curves (displaced on purpose for better visibility) and b) specular θ - 2θ XRD scan of the GaN/ Sc_2O_3 / Y_2O_3 /Si(111) system.

In-plane XRD

The azimuthal orientation of the GaN(0001)/ Sc_2O_3 (111)/ Y_2O_3 (111)/Si(111) heterostructure was studied by SR-GIXRD in-plane measurements performed at $L=0.03$ r.l.u. (reciprocal lattice unit). At the employed X-ray beam energy of 15 keV, the critical angle α_c for the total reflection from GaN surface is 0.18° . The incident angle α_i of the X-ray onto the specimen surface was varied from 0.2° (bulk sensitive: $\alpha_i > \alpha_c$) to 0.1° (surface sensitive: $\alpha_i < \alpha_c$). Figure 3.8 shows the scans along the K-axis (corresponding to Si[$\bar{2}11$]) with K ranging from 0.5 to 6.2 r.l.u. The top curve, obtained with an incident angle of 0.2° , gives information about the entire heterostructure. The allowed Si($\bar{4}22$) and Si($\bar{8}44$) Bragg peaks from Si(111) substrate are expected at $K=3$ r.l.u. and $K=6$ r.l.u., respectively. Due to the fact that the Y_2O_3 layer is 5 nm thin, only one weak Y_2O_3 ($\bar{8}44$) reflection is detected at $K=3.081$ r.l.u. This weak and rather broad signal does not allow a further precise discussion of the in-plane

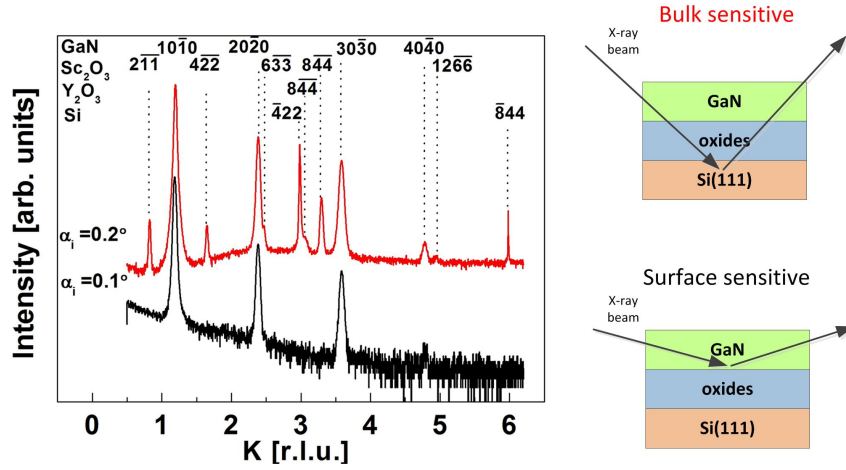


Figure 3.8: GI-XRD measurements ($L=0.03$) at $\alpha_i=0.1^\circ$ and $\alpha_i=0.2^\circ$ along the Si $[2\bar{1}1]$ direction.

Y₂O₃ lattice parameter constant. In addition, five Sc₂O₃ reflections are detected at $K=0.83, 1.66, 2.49, 3.32,$ and 4.98 r.l.u. These peaks are attributed to the Sc₂O₃ ($2\bar{1}1$), ($4\bar{2}2$), ($6\bar{3}3$), ($8\bar{4}4$), and ($12\bar{6}6$) Bragg peaks, respectively. The lattice constant calculated from the high order Sc₂O₃($8\bar{4}4$) peak position is 9.50\AA and agrees with the fully relaxed cubic lattice. Diffraction signals of the GaN layer are found at $K=1.19, 2.38, 3.57,$ and 4.76 r.l.u. and are attributed to the GaN($10\bar{1}0$), ($20\bar{2}0$), ($30\bar{3}0$), and ($40\bar{4}0$) Bragg peaks, respectively. Furthermore, the bulk sensitive scan nicely demonstrates the role of the oxide buffer as lattice mismatch mediator: its Y₂O₃($8\bar{4}4$) and Sc₂O₃($8\bar{4}4$) Bragg peaks are situated between Si($4\bar{2}2$) and GaN($30\bar{3}0$) diffraction signals. Based on these results the following conclusions can be drawn:

- It is seen from the position of the Si($4\bar{2}2$) and Y₂O₃($8\bar{4}4$) Bragg peaks that the Y₂O₃ lattice value is by about -2% smaller than twice the Si lattice constant.
- As seen by the Y₂O₃($8\bar{4}4$) and Sc₂O₃($8\bar{4}4$) Bragg peaks, the oxide films match each other on the basis of a (1x1) coincidence but the Sc₂O₃ lattice is by about -7% smaller.
- In addition, it can be deduced from the Sc₂O₃($8\bar{4}4$) and GaN($30\bar{3}0$) peak positions that $1/3 d$ GaN¹⁰⁻¹⁰ is by about -8% smaller than $1/4 d$ Sc₂O₃²⁻¹⁻¹.

The epitaxial in-plane alignment of the heterostructure is characterized by the relationship: GaN $[10\bar{1}0] \parallel$ Sc₂O₃ $[2\bar{1}1] \parallel$ Y₂O₃ $[2\bar{1}1] \parallel$ Si $[\bar{2}11]$

A second in-plane scan was performed along the K direction in the surface sensitive mode at $\alpha_i=0.1^\circ$ (bottom curve in Fig. 2.13). Based on the fact that the diffraction signals from Si and buffer oxides are fully suppressed and only four GaN reflections are visible, it is clearly demonstrated that the epitaxial GaN forms a closed layer on a global scale.

3.2.2 Crystalline quality

Results presented in this section were obtained for 30 nm-thick GaN films grown on a fully relaxed oxide buffer on Si(111) substrates.

Reciprocal space maps

Figure 3.9 shows a RSM for the GaN(0001)/Sc₂O₃(111) /Y₂O₃(111)/Si(111) heterostructure in the H-L plane. The sketch in the top part of Fig. 3.9 represents all expected reflections in the L range from 0.0 to 0.85 r.l.u. and H range from -0.75 to -2.7 r.l.u., according to the epitaxial out-of-plane and in-plane relationships derived from the studies presented in Figs. 3.7 and 3.8. In this H-L region of reciprocal space, a bulk sensitive mesh scan with α_i 0.4° was performed. The detected Si, Y₂O₃, Sc₂O₃ and GaN peak positions are in very good agreement with those theoretically predicted. Moreover, no additional reflections are observed, which could indicate the presence of misoriented grains (e.g. inclusion of cubic GaN) or possible mixed phases (due to, e.g. interface reactions). However, the diffuse scattering around the GaN Bragg peaks clearly indicates the presence of defects causing tilt and twist of the GaN lattice.

Williamson-Hall analysis

Information regarding the quality of the heterostructure can be extracted from the RSMs shown in Fig. 3.10 a) and c). Note that the RSM is obtained by taking a series of ω scans at successive $\omega-2\theta$ values and presenting the results as a map. In order to plot such a map, the angles from radial and angular scans are converted into reciprocal lattice units. Figure 3.10 a) shows the RSM of the out-of-plane Si(111), Y₂O₃(222), Sc₂O₃(222) and GaN(0002) reflections. The coordinates Q_z and Q_x can be expressed as

$$Q_z = \frac{2 \sin \theta + \sin(2\theta - \omega)}{\lambda} \quad (3.3)$$

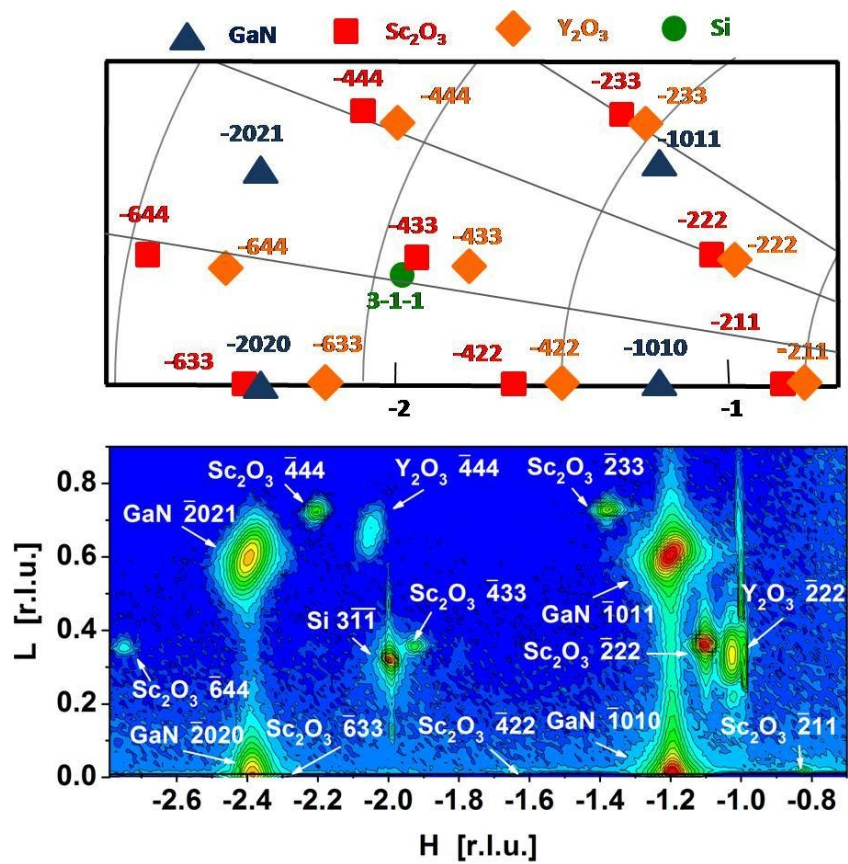


Figure 3.9: Out-of plane H-L mesh scan with L and H ranging from -0.75 to -2.7 and 0 to 0.85 r.l.u., respectively.

$$Q_x = \frac{\cos(2\theta - \omega) - \cos \omega}{\lambda} \quad (3.4)$$

and point in the Si[111] and Si[2 $\bar{1}\bar{1}$] directions in real space, respectively. It is noted that the Y₂O₃(222) Bragg peak is too weak to be analyzed and it is not further discussed.

The Sc₂O₃(222) and GaN(0002) peaks show an anisotropic shape with smaller and bigger FWHM values in the Q_z and Q_x directions, respectively. The broadening of the peaks in the Q_z and Q_x directions can be caused by a vertical strain variation and out-of plane lattice tilt, respectively. In addition, to gain deeper insights in the structural perfection of the Sc₂O₃ and GaN films, a Williamson Hall (W-H) analysis was performed.¹²⁰ For this analysis, besides the RSM in Fig. 3.10 a), radial and angular scans were measured for the investigation of higher order reflections. The out-of-plane results of this method are presented in Fig. 3.10 b). Here, the FWHM values ΔQ_z and ΔQ_x for Sc₂O₃(222), (444), (666) and GaN(0002), (0004), (0006) are plotted as a function of peak position Q_z in reciprocal space. Linear regressions for each of the four data sets were performed. Based on the W-H analysis performed in Q_z and Q_x direction the following layer characteristics can be obtained:

- **z-analysis**

1. Domain size in the Q_z direction
(the intercept resulting from fitting the ΔQ_z data is inversely proportional to the domain sizes D_z)
2. Average vertical strain variation
(from the slope of the linear fits of ΔQ_z)

- **x-analysis**

1. Domain size in the Q_x direction
(the intercept resulting from fitting the ΔQ_x data is inversely proportional to the domain sizes D_x)
2. Tilt of the mosaic blocks
(from the slope of the linear fits of ΔQ_x)

The Sc₂O₃ and GaN domain sizes calculated from the FWHM analysis of the Q_z values are 27 and 30 nm, respectively. These values are close to the GaN and Sc₂O₃ layer thicknesses measured by XRR. A small average vertical strain variation of about 0.26% in the Sc₂O₃ and 0.28% in the GaN layer from the

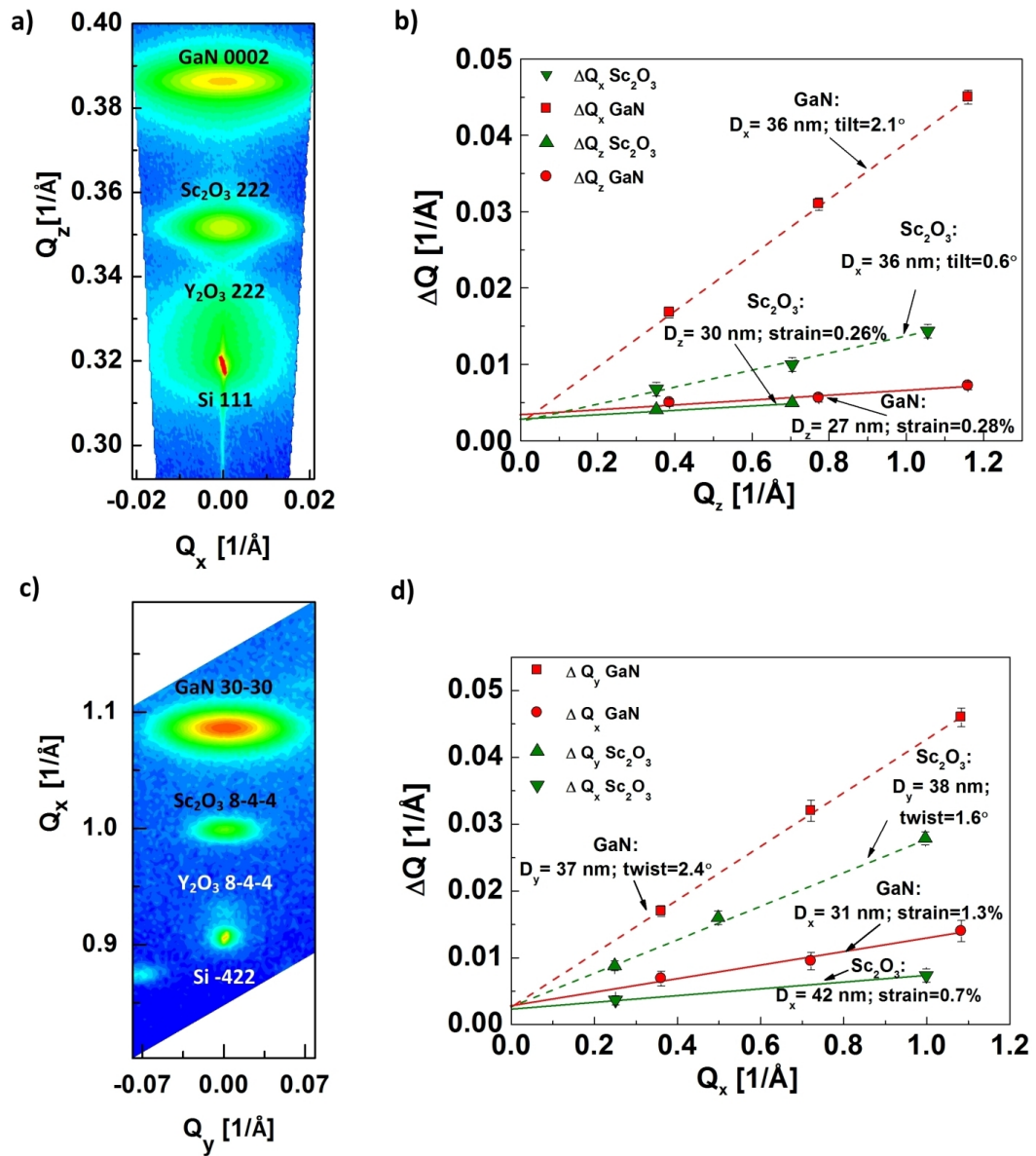


Figure 3.10: RSMs a) out-of-plane Si[111], and c) in-plane Si[2 $\bar{1}\bar{1}$] directions. Williamson-Hall analysis of the GaN and Sc₂O₃ reflections b) out-of-plane and d) in-plane study.

slope of the ΔQ_z values is detected. It is worth noting that strain variation is a manifestation of the microstrain (broadening of the x-ray peaks) which is a distinctly different phenomenon from the peak shift caused by residual strain.¹⁴³ The Sc_2O_3 and GaN domain sizes in the Q_x direction are 36 nm for both layers. From the slope of the ΔQ_x values, the GaN lattice tilt is found to be 2.1° , which is about three times higher than the lattice tilt in the Sc_2O_3 buffer layer (0.6°). The extracted tilt angle of about 2.1° is probably a manifestation of a relatively high screw dislocation (running along the c-axis) content in the GaN film.^{144,145}

The RSM of the in-plane $\text{Si}(4\bar{2}\bar{2})$, $\text{Y}_2\text{O}_3(\bar{8}44)$, $\text{Sc}_2\text{O}_3(\bar{8}44)$ and $\text{GaN}(30\bar{3}0)$ reflections is shown in Fig. 3.10 c). Here, the Q_x and Q_y can be expressed as:

$$Q_x = \frac{2 \sin \theta + \sin(2\theta - \omega)}{\lambda} \quad (3.5)$$

$$Q_y = \frac{\cos(2\theta - \omega) - \cos \omega}{\lambda} \quad (3.6)$$

and correspond to the $\text{Si}[2\bar{1}\bar{1}]$ and $\text{Si}[\bar{1}\bar{1}0]$ directions for the real space, respectively. Similarly to the RSM shown in Fig. 3.10 a), the $\text{Sc}_2\text{O}_3(\bar{8}44)$ and $\text{GaN}(30\bar{3}0)$ peaks exhibit an anisotropic shape with FWHMs higher in the Q_y than in the Q_x direction. In the present case, the broadening of the peaks in the Q_x and Q_y directions can be a manifestation of an in-plane strain variation and in-plane lattice twist, respectively. The Williamson-Hall analysis for the in-plane scans is shown in Fig. 3.10 d). In this case, the ΔQ_x and ΔQ_y values for $\text{Sc}_2\text{O}_3(\bar{2}11)$, $(\bar{4}22)$, $(\bar{8}44)$ and $\text{GaN}(10\bar{1}0)$, $(20\bar{2}0)$, $(30\bar{3}0)$ peaks were measured. Based on these measurements the following layer characteristics can be obtained:

- **x-analysis**

1. Domain size in the Q_x direction
(the intercept resulting from fitting the ΔQ_x data is inversely proportional to the domain sizes D_x)
2. Average in-plane strain variation
(from the slope of the linear fits of ΔQ_x)

- **y-analysis**

1. Domain size in the Q_y direction
(the intercept resulting from fitting the ΔQ_y data is inversely proportional to the domain sizes D_y)

2. Twist of the mosaic blocks
(from the slope of the linear fits of ΔQ_y)

The Sc₂O₃ domain sizes in the Q_x and Q_y directions are found to be 42 nm and 38 nm, respectively. The corresponding values for GaN are 31 nm and 37 nm, respectively. For the Sc₂O₃ layer, the in-plane strain variation and the twist angle amount to 0.7% and 1.6°, respectively. For the GaN layer the in-plane strain variation is 1.3%, and the twist amounts to 2.4°. The twist angle of about 2.4° is probably a manifestation of a relatively high edge dislocation (running along c-axis with the in-plane Burger vector) content in the GaN film. Based on the above Williamson-Hall analysis, it is concluded that the thin GaN layer is characterized by larger strain variations and higher values of lattice tilt and twist in comparison with the Sc₂O₃ buffer layer.

3.2.3 Summary

In summary, single crystalline 30 nm-thick GaN films were successfully grown on Si(111) by using Sc₂O₃/Y₂O₃ bi-layer buffer. GaN layers of this thickness are closed on the global scale and of limited roughness. Specular θ - 2θ XRD scans reveal that the vertical growth orientation of the heterostructure is:

$$\text{GaN}(0001)/\text{Sc}_2\text{O}_3(111)/\text{Y}_2\text{O}_3(111)/\text{Si}(111).$$

The in-plane orientation is given by:

$$\text{GaN}[10\bar{1}0] \parallel \text{Sc}_2\text{O}_3[2\bar{1}\bar{1}] \parallel \text{Y}_2\text{O}_3[2\bar{1}\bar{1}] \parallel \text{Si}[\bar{2}11].$$

By the in-plane XRD scan it is proved that the oxide buffer plays a lattice mismatch mediator role between GaN and Si. The lattice misfit between GaN and the substrate can be reduced from 17% to 8% what is the mismatch between GaN and Sc₂O₃. Based on in-plane and out-of-plane XRD scans, it is concluded that 30 nm GaN layers grown on Sc₂O₃/Y₂O₃ buffers are under tensile strain, probably due to difference in thermal expansion coefficients of the materials composing the heterostructure.

Williamson-Hall analysis of thin GaN films revealed that the tilt and twist values are higher than for the Sc₂O₃ oxide buffer. The relatively high tilt and twist angles of the GaN mosaic blocks can be associated with the high content of dislocations which are running along c-axis and have the Burgers vector parallel to the [0001] and $\langle 11\bar{2}0 \rangle$ direction, respectively.

3.3 Thick GaN on Sc₂O₃/Y₂O₃ buffer on Si(111)

3.3.1 GaN growth diagram

Proof-of principle study described in the previous section demonstrates that it is possible to achieve thin single crystalline hexagonal GaN films on Si(111) substrates via Sc₂O₃/Y₂O₃ buffer layers. However, 30 nm-thick GaN films are too thin for any electronic and optoelectronic applications. Therefore, the next steps in the GaN project were dedicated to the deposition of μm -thick layers with as low as possible dislocation density. As discussed in the Introduction, the final layer quality strongly depends on the growth conditions. In order to find a proper deposition parameters, the GaN growth diagram was prepared (Fig. 3.11). Here, the GaN growth rates (V_{rate}) are plotted as a function of the Ga K-cell temperature (T_{Ga}). The first set of samples was grown at the substrate temperature (T_{sub}), N_{flow} , power of RF plasma source of 720°C, 0.4 sccm and 300W, respectively. It is seen by the RHEED and SEM study (Fig. 3.11 b)) that the variation of T_{Ga} over 50°C results in a dramatic change of the GaN film morphology:

- at $T_{Ga}=910^\circ\text{C}$ (A), closed GaN films are obtained. The spotty RHEED pattern implies that the GaN surface is very rough. Indeed, GaN layers deposited in ***N-rich regime*** are characterized by closely-packed nanocolumns.
- at $T_{Ga}= 918\text{-}930^\circ\text{C}$ (B- C), a smooth transition from a spotty to streaky RHEED pattern is observed. Here, the GaN layer is composed of coalesced blocks.

This regime is the so-called ***transition regime*** when the Ga/N ratio is close to unity.

- at $T_{Ga}=940^\circ\text{C}$ (D)), GaN islands with a smooth surface are formed. Deep valleys visible in the SEM image are probably filled with Ga. Under ***Ga-rich*** condition, this excess of Ga should form a steady-state layer on the smooth GaN film.
- at $T_{Ga}=960^\circ\text{C}$ (E), ***Ga droplets*** formation on the GaN surface is observed.

Theoretically, when the growth is performed in the Ga-rich/Ga-droplet regime, the GaN layer area between Ga droplets should be closed and smooth. However, due to a poor wetting behaviour of Sc₂O₃ by GaN, it was not possible to

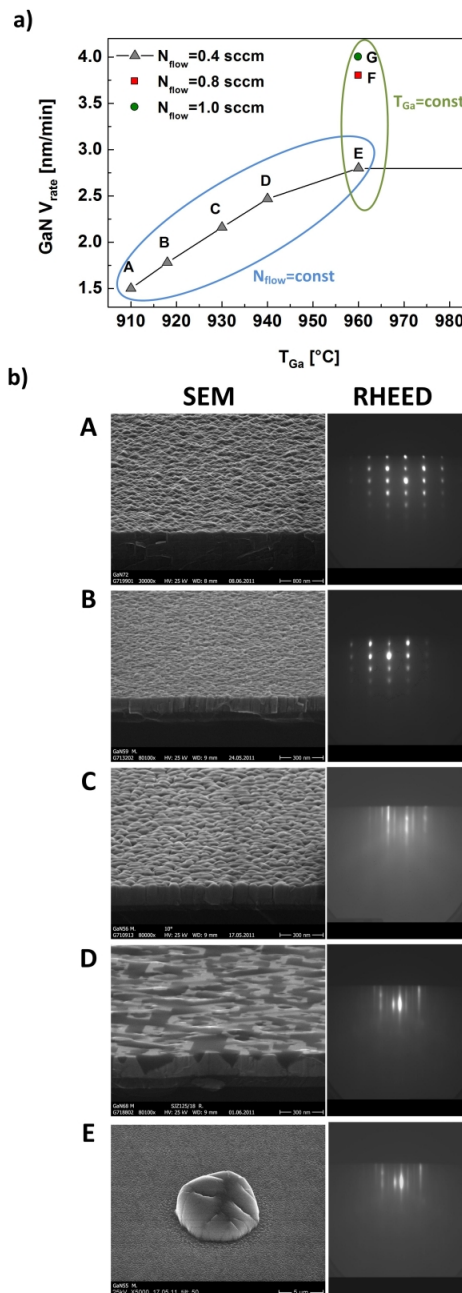


Figure 3.11: a) GaN growth diagram ($T_{sub} = 720^\circ\text{C}$). First set of samples (A, B, C, D, E) was prepared at constant $N_{flow} = 0.4$ sccm and T_{Ga} varied between 910 and 980°C. Second set (E, F, G) was grown at constant $T_{Ga} = 960^\circ\text{C}$ and N_{flow} varied between 0.4 and 1.0 sccm. b) SEM images and the corresponding RHEED patterns obtained for the first set of GaN calibration samples.

obtain 2D films for this growth parameters.

Second set of samples was grown at the parameters T_{sub} , T_{Ga} , power of RF plasma source of 720°C , 960°C and 300W , respectively. N_{flow} was varied between 0.4 and 1 sccm. In this way, the growth smoothly changed from the Ga-droplet (E) to the Ga-rich (G) regime. However, the GaN layer morphology does not change significantly. SEM images for these experiments are shown in Fig. 3.12.

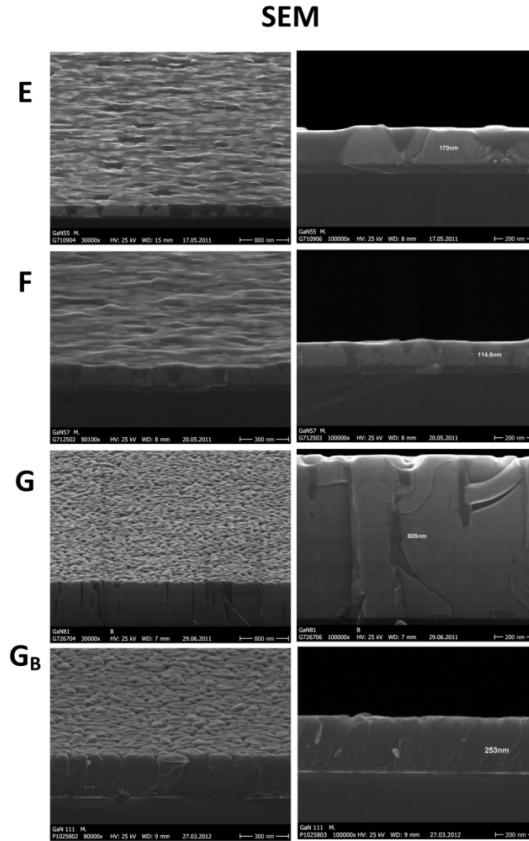


Figure 3.12: SEM of the second set of calibration samples. The GaN layers were grown at constant T_{Ga} of 960°C and N_{flow} varied between 0.4 and 1.0 sccm.

The optimum GaN film properties are usually achieved when the growth is performed on the boundary between the Ga-rich and Ga-droplet regime, when the Ga/N ratio is higher than unity. The calculated Ga/N ratios for samples E, F, G are presented in Tab. 3.1. When the ratio is equal 1.5 (E), dense Ga droplets are visible on the GaN surface. Widely spaced Ga droplets are formed when the Ga/N ratio is 1.1 . A GaN layer without any droplets is achieved when this ratio is equal to 1 (G).

The GaN layer morphology does not change when a lower T_{sub} is used. This can be seen for sample G_B which was deposited at similar growth conditions as sample G, but at lower T_{sub} of 650°C. For sample G_B the obtained G^a/N ratio is also equal to 1 (the same desorption rate for T_{sub} 720°C and 650°C), GaN layer is free of droplets and is composed of coalesced blocks. To learn more

Table 3.1: G^a/N ratio for the second set of calibration samples.

sample	T_{sub} [°C]	T_{Ga} [°C]	N_{flow} [sccm]	G^a/N	remarks
E	720	960	0.4	1.5	dense droplets on the GaN layer
F	720	960	0.8	1.1	widely spaced droplets on GaN layer
G	720	960	1.0	1.0	layer without droplets
G_B	650	960	1.0	1.0	layer without droplets

about the quality of GaN layers prepared under various conditions, two sets of thick GaN samples were grown and further characterized. First set was grown in the N-rich regime (like sample A) and the second set in the Ga-rich regime (like sample G). These samples were analyzed ex-situ by XRD, PL, and EDX in a STEM mode. For STEM images a high angle annual dark field (HAADF) detector was used. The results of these investigations are summarized in the following section.

3.3.2 Crystalline quality of μm - thick GaN films prepared under Ga-rich and N-rich conditions

Threading dislocation density

High resolution XRD analysis for a 800 nm film grown in the Ga-rich regime is displayed in Fig. 3.13. The sample structure is illustrated by a high resolution TEM image in Fig. 3.13 a). The specular $\theta-2\theta$ scan (Fig. 3.13 b)) reveals the vertical growth orientation of GaN(0001)/Sc₂O₃(111)/Y₂O₃(111)/Si(111). Threading screw dislocation (TSD) and threading edge dislocation (TED) densities were estimated by measuring the GaN(0004) (Fig. 3.13 c)) and (10 $\bar{1}$ 0) (Fig. 3.13 d)) rocking curves, respectively. Initial evaluation of the GaN crystalline perfection is obtained from the FWHM of the rocking curves which is 0.39° for the GaN(0004) and 0.55° for the GaN(10 $\bar{1}$ 0) peak. More detailed analysis was accomplished by fitting the diffraction peaks.¹⁴⁶ Best fits are dis-

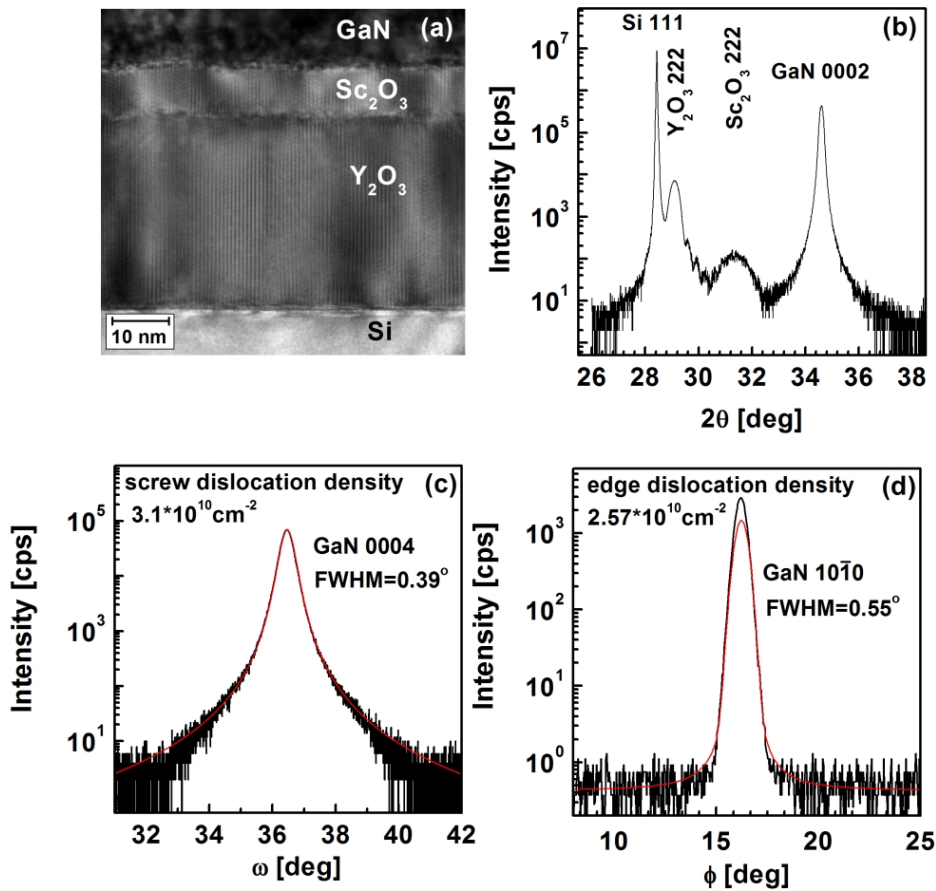


Figure 3.13: a) TEM cross section of the GaN/Sc₂O₃/Y₂O₃/Si(111) heterostructure; viewed along the $\langle 11\bar{2} \rangle$ azimuth; b) specular $\theta-2\theta$ scan; rocking curve scan over c) GaN(0004) and d) GaN(10 $\bar{1}$ 0) reflection. Fitting curves are shown by the red lines.

played as red curves in Figs. 3.13 c) and d) and reveal TSD and TED densities of 3.1×10^{10} and $2.6 \times 10^{10} \text{ cm}^{-2}$, respectively. Similar analysis performed for the 900 nm sample grown in the N-rich regime gives TSD density of 9.1×10^{10} and TED density of $3.3 \times 10^{11} \text{ cm}^{-2}$.

The crystalline quality of the GaN layers grown on Sc₂O₃/Y₂O₃/Si(111) is dependent on the GaN layer thickness and post deposition rapid thermal annealing (RTA). This behavior is similar to that observed for growth on sapphire.¹⁴⁷ Figure 3.14 summarizes the influence of the GaN layer thickness and RTA (N₂ ambient) on the FWHM of the GaN(0004)(Fig. 3.14 a)) and (10 $\bar{1}$ 0) (Fig. 3.14 b)) peaks. For samples grown in the N-rich regime the FWHM of the GaN(0004) peak (Fig. 3.14 a)) decreases from 1.5° for a 150 nm film to 0.7° for a 900 nm layer. This reduction results probably from a gradual annihilation of

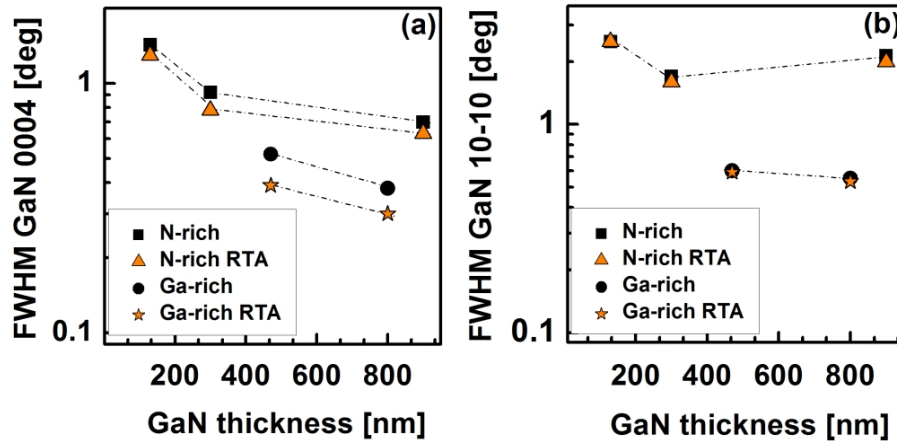


Figure 3.14: FWHM of GaN a) (0004) and b) $(10\bar{1}0)$ peaks as a function of thickness and growth conditions.

TSDs with increasing thickness. Further GaN(0004) width reduction by about 12% independent of the GaN thickness can be achieved by RTA at 900°C. Similar trends are observed for samples grown in the Ga-rich regime; the FWHM decreases from 0.5° for a 450 nm sample to 0.4° for a 800 nm layer. Also in this case, the GaN(0004) peak narrows after RTA by about 23%. Changes in the FWHM of the GaN $(10\bar{1}0)$ reflection are shown in Fig. 3.14 b). Samples grown under N-rich conditions show FWHM of 2.5° at 150 nm decreasing to 1.8° at 900 nm. Samples grown in the Ga-rich regime show FWHM of 0.6° at 450 nm and 0.5° at 800 nm. Figure 3.14 gives thus evidence that Ga-rich growth condition result in smaller FWHMs of both GaN(0004) and $(10\bar{1}0)$ rocking curves, implying better crystalline quality in comparison with N-rich conditions. Additionally, post deposition RTA has a significant influence on the GaN(0004) peak width for samples grown in both regimes. In contrast, the same RTA treatment has a negligible impact on the FWHM of the GaN $(10\bar{1}0)$ reflection.

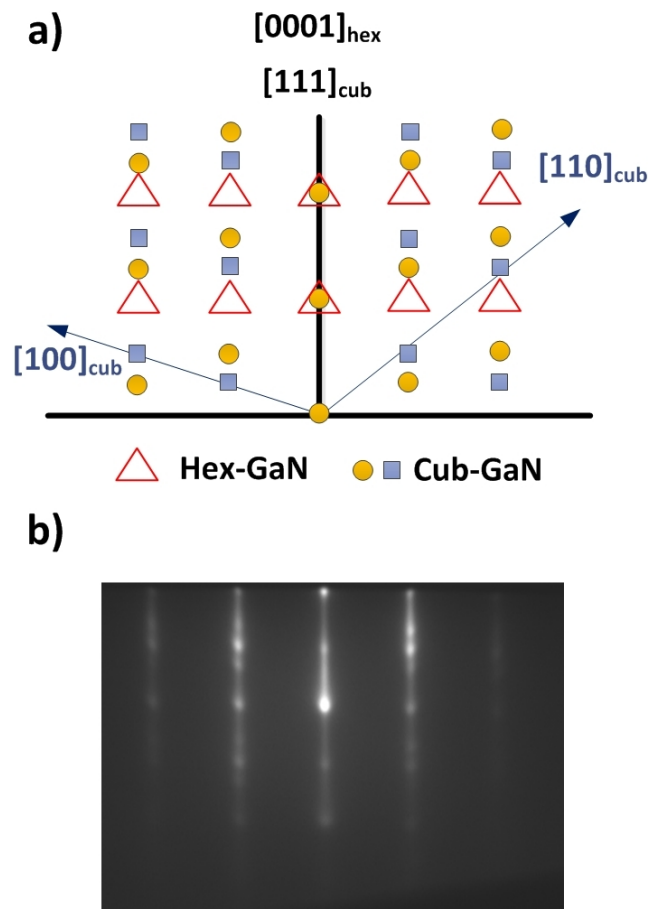


Figure 3.15: a) Schematic RHEED pattern for cub- and hex-GaN. Position of diffraction spots from cub-GaN indicates that the cub-phase is twinned b) RHEED pattern obtained after 5 min of the GaN deposition.

Cubic GaN inclusions

In situ RHEED study of the initial GaN growth stage reveals the co-existence of (111) oriented cubic (cub-GaN) and (0001) oriented hexagonal (hex-GaN) domains (Fig. 3.15).

As growth proceeds, the intensity of the RHEED pattern associated with the cub-GaN gradually decreases and disappears when the GaN film thickness reaches about 20 – 30 nm. To investigate the relation between the cub-GaN and the hex-GaN phases as a function of GaN thickness, ex-situ XRD pole figure studies were performed ($2\theta=70^\circ$).¹⁴⁴ An example is shown in Fig. 3.16 a) for a 900 nm GaN layer grown on $\text{Sc}_2\text{O}_3/\text{Y}_2\text{O}_3/\text{Si}(111)$ under N-rich conditions. The presence of the diffraction spots originating from Si and the buffer

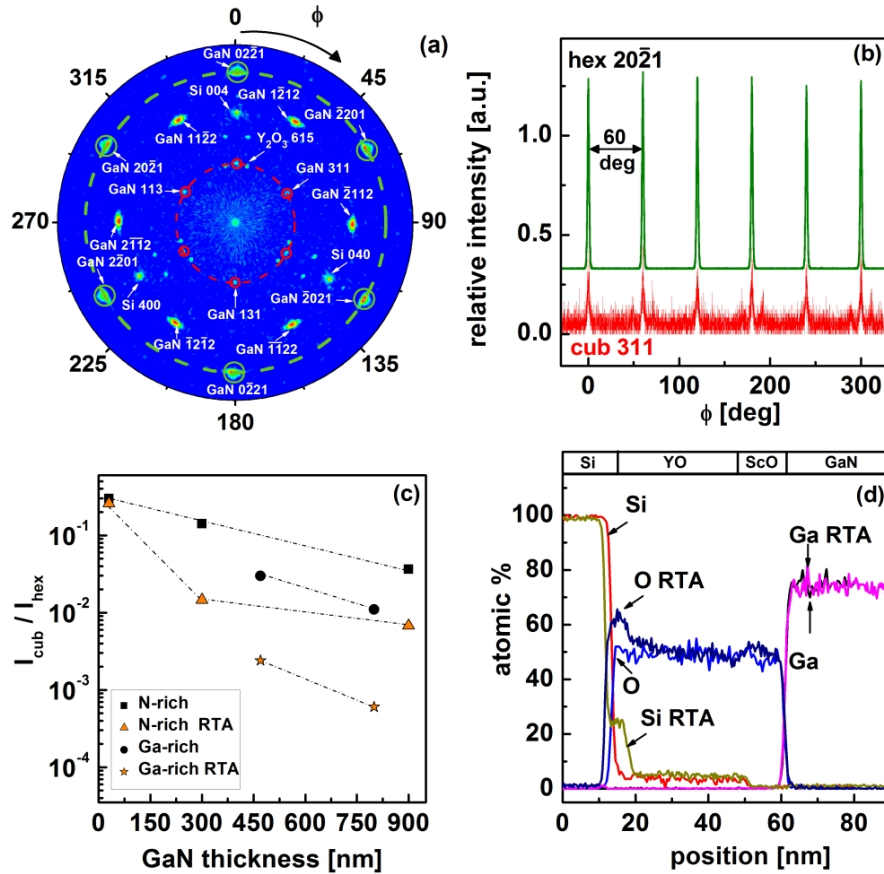


Figure 3.16: a) Pole figure ($2\theta=70^\circ$) of 900 nm GaN grown in N-rich regime on $\text{Sc}_2\text{O}_3/\text{Y}_2\text{O}_3/\text{Si}(111)$; b) Φ scan across hex-GaN $\{20\bar{2}1\}$ at $\chi=75^\circ$ and cub-GaN $\{311\}$ at $\chi=29^\circ$; c) cub-GaN(311)/hex-GaN(20-21) intensity ratio as a function of thickness; d) EDX profile of the heterostructure.

(labeled in Fig. 3.16 a)) indicates that the complete GaN layer is measured. The appearance of the hex-GaN{20 $\bar{2}$ 1} and cub-GaN{311} reflections at χ angles of 75° (green circle) and 29° (red circle) proves the presence of both hex and cub phases in the film. For clarity, ϕ scans along the green and red circles are extracted and plotted in Fig. 3.16 b). It is seen that the intensity of the hex-GaN{20 $\bar{2}$ 1} reflections is about three times higher than that of the cub-GaN{311}. In addition, the six GaN(311) peaks indicate twinned GaN cubic inclusions.¹⁴⁸ Figure 3.16 c) compares the intensity ratio of the cub-GaN(311) and hex-GaN{20 $\bar{2}$ 1} reflections for different GaN layer thicknesses and growth conditions. It is noted, that due to different structure factors and scattering geometries of the investigated diffraction peaks, the intensity ratio is not identical to the cub-GaN/hex-GaN domain population ratio. In general, as-grown GaN layers prepared in the N-rich regime show higher cub/hex intensity ratio than films grown in the Ga-rich regime at comparable thicknesses. The ratio is also clearly dependent on the GaN layer thickness. For samples grown in N-rich regime, the cub/hex intensity ratio decreases from 0.3 for 30 nm layers to 0.036 for 900 nm films. For samples grown in the Ga-rich regime the ratio decreases from 0.029 at 470 nm to 0.011 at 800 nm. These results corroborate the in situ RHEED observations and prove that the cub-GaN inclusions are formed in the initial growth stage at the GaN/Sc₂O₃ interface and their formation is suppressed during further GaN growth. Probably, cub-Sc₂O₃(111) acts as nucleation seed for cub-GaN(111). Furthermore, the concentration of cub-GaN in the hexagonal matrix is higher for samples grown in N-rich regime than for those grown in Ga-rich regime. This behavior might be attributed to an interfacial reaction between the Sc₂O₃ and the impinging N and Ga atoms and the formation of N-O bonds in the interface region during growth. Such scenario was previously proposed to explain formation of cubic inclusions in hex GaN grown on ZnO and Al₂O₃.¹⁴⁹

The cub/hex intensity ratio can be influenced by RTA for samples prepared in both growth regimes (Fig. 3.16 c)). For example, for a 800 nm layer grown in Ga-rich regime the cub/hex ratio is reduced from 0.011 to 0.0006 after RTA at 900°C, suggesting that cub-GaN is partially transformed into hex-GaN. While the origin of the cub-GaN formation is still under investigation for the GaN/Sc₂O₃/Y₂O₃/Si(111) system it can be stated that based on EDX, it is not directly related to oxygen diffusion into the GaN layer as previously suggested.¹⁵⁰ Normalized concentration profiles of Si, O, Y, Sc, N and Ga were determined by EDX analysis before and after RTA of a 600 nm GaN

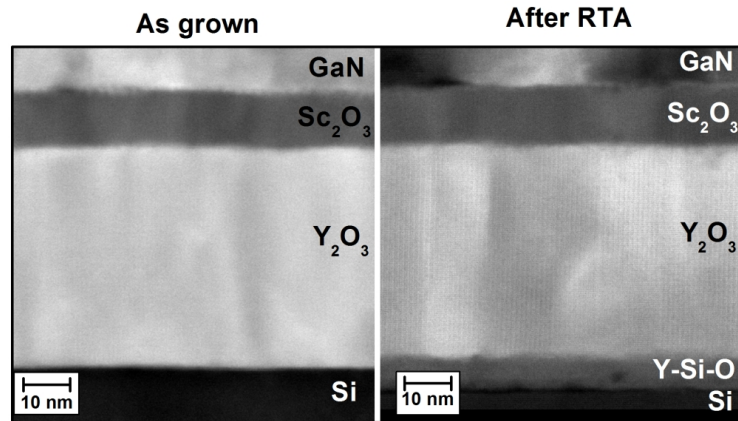


Figure 3.17: Cross-section HAADF STEM images of GaN/Sc₂O₃/Y₂O₃/Si(111) heterostructure before (left) and after RTA (right).

layer grown in the N-rich regime (Fig. 3.16 d), profiles of Sc, Y and N are not shown). The oxygen profile at the GaN/Sc₂O₃ interface is identical for the GaN layer before and after RTA. In addition, after RTA, formation of an amorphous Y-silicate at the Y₂O₃/Si interface is observed.¹⁵¹ The existence of around 5 nm-thick amorphous Y-silicate layer after RTA is confirmed by a cross-section HAADF images presented in Fig. 3.17. Note that the Si substrate is partially consumed by the interfacial Y-silicate layer. No further RTA-induced changes in the oxide buffer layer structure and the GaN/Sc₂O₃ interface are detected. Interestingly, using AlGaN buffer systems, Ga diffuses into Si substrate and creates a parasitic p-doping layer which is detrimental for high-frequency applications. Here, for the Sc₂O₃/Y₂O₃ buffer, this problem seems not to exist.

GaN polarity- inversion domain boundaries

Polarity of the GaN layers was determined based on the RHEED observations. A characteristic (3×3) surface reconstruction detected after GaN growth (Fig. 3.11 sample C and D) indicates that the GaN layers are N-polar. However, TEM investigations reveal that these films contain inversion domain boundaries (IDBs). IDBs are formed on the boundaries between the Ga- and N-polar GaN regions as shown in Fig. 3.18.

This type of defect has a huge impact on the properties of the GaN-based device e.g HEMT in which the layer polarity determines the direction of the polarization field. The discontinuity in the polarization field (mixture of the Ga- and N-polar regions) will cause a reduction in the mobility of the 2D electron

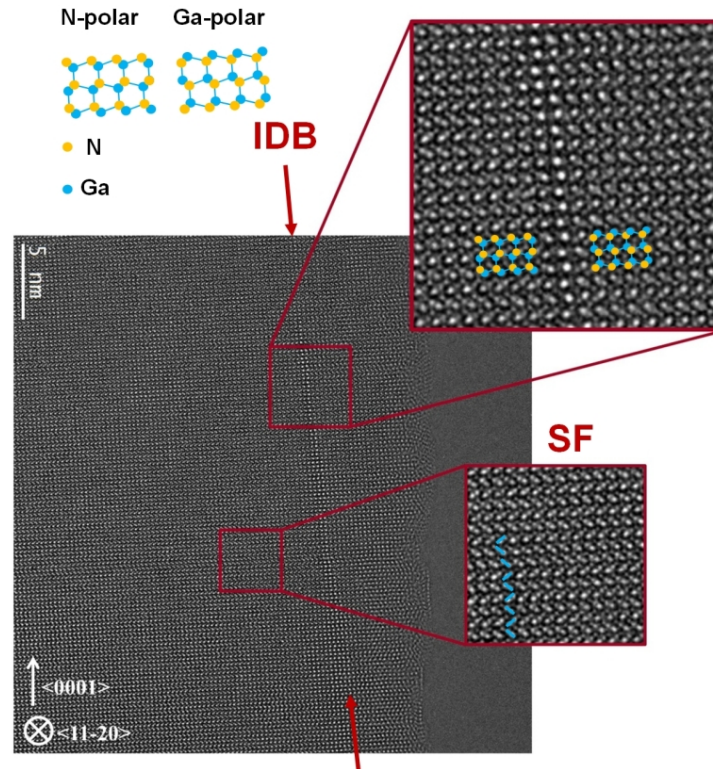


Figure 3.18: High resolution TEM image of the GaN layer grown under Ga-rich conditions. Inversion domain boundary (IDB) and stacking fault (SF) defects are indicated by the red squares in the image. *TEM images courtesy of D.Zengler and Prof. Lehmann from TU Berlin.*

gas.³¹

In addition, in the TEM image (Fig. 3.18) another type of structural defect, the so-called stacking fault (SF) defect, is visible. As discussed in the Introduction, GaN can crystallize either in the hexagonal closed-packed (hcp) or face-centered cubic (fcc) structure. The difference between them is just the stacking configuration. The hcp lattice is formed by the stacking sequence: AaBbAaBb... along the $[0001]$ direction and fcc cubic lattice by AaBbCcAaBbCc... along $[111]$ direction (with capital and small letters denoting Ga and N layers, respectively). SF can be considered as an error in the usual stacking sequence e.g. AaBb**AaBb**CcBbCc...(interruption in the zig-zag like structure in Fig. 3.18).

3.3.3 Optical properties

Figure 3.19 shows 10K PL spectra from the GaN films grown in N- and Ga-rich regimes. The spectrum for the 800 nm GaN layer grown under Ga-rich con-

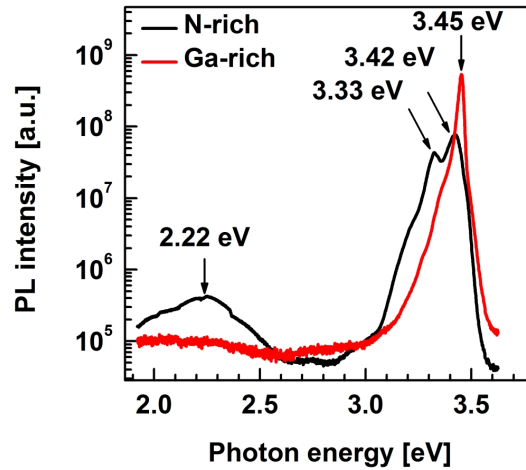


Figure 3.19: Low temperature (10K) PL spectra from thick GaN films grown in the N-rich (black) and Ga-rich regime (red).

ditions is dominated by a relatively sharp (FWHM of 22 meV) and relatively intense emission peak at 3.45 eV (donor bound exciton transition (D^0X)).¹⁵² Yellow luminescence (YL) usually detected at 2.22 eV is not clearly distinguishable for this sample. On the contrary, GaN samples grown under N-rich conditions (900 nm GaN film) exhibit broad defect-related YL and clear peaks at 3.42 eV (D^0X , FWHM of 77 meV) and 3.33 eV (probably due to overlapping emission spectra related to longitudinal optical phonon replica of the D^0X line, donor-acceptor pair transition, and excitons bound to structural defects). Shift in the D^0X line position between N-rich and Ga-rich samples is associated with the different donor/impurities incorporated in the samples grown in two different regimes.

3.3.4 Strain components in thick GaN layers

μm -thick GaN layers deposited on Sc₂O₃/Y₂O₃/Si(111) templates exhibit dense cracking (Fig. 3.20) due to the large tensile stress. Strain components in the GaN film were studied in-situ by means of high-temperature XRD technique. The results demonstrated by Zaumseil *et al.* (Ref. 153) reveal that the GaN layer grows at 720°C slightly tensile strained on top of the 8% larger Sc₂O₃ lattice and that this strain increases further during cooling down to the room temperature due to 56% difference in TEC between GaN and Si. This implies that the GaN layer as well as the oxide buffer is in-plane fixed to the Si substrate and that the in-plane lattice constant of both epilayers, oxide as well as GaN, follows the substrate's TEC. Therefore it is concluded that

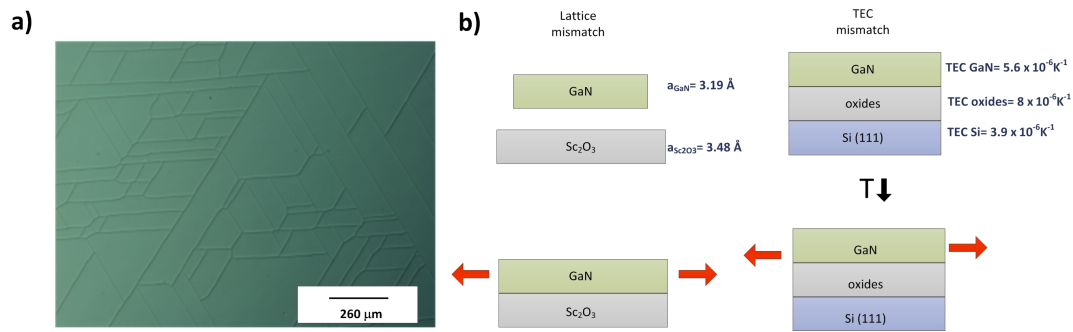


Figure 3.20: a) μm - thick GaN layers grown on Sc₂O₃/Y₂O₃/Si(111) template crack due to large tensile stress. b) Tensile stress has two components: 8% lattice mismatch between GaN and Sc₂O₃ buffer and thermal mismatch between GaN and Si substrate.

the Sc₂O₃/Y₂O₃ buffer system does not solve the TEC mismatch problems between GaN and Si.

3.3.5 Summary

In summary, the structural and optical quality of μm -thick GaN layers grown on Sc₂O₃/Y₂O₃/Si(111) templates was investigated. The GaN films were deposited in two growth regimes: N-rich and Ga-rich, close to the stoichiometric condition. Deposition under N-rich conditions results in a spotty RHEED pattern which indicates that GaN surface is very rough. On the other hand, GaN layers grown under Ga-rich conditions are composed of flat coalesced blocks. For both growth regimes, in the initial GaN growth stage the co-existence of cubic and hexagonal GaN domains is observed. As the growth proceeds, the formation of cubic GaN inclusions is suppressed and hexagonal GaN layers on Sc₂O₃/Y₂O₃/Si(111) are obtained. The existence of cubic inclusion at the GaN/Sc₂O₃ interface may be attributed to the formation of N-O bonds, which are more favored to form in the N-rich regime. Therefore, samples grown under N-rich conditions are characterized by a higher density of cubic inclusions than the layers grown under Ga-rich conditions. In addition, GaN layers deposited in the Ga-rich regime exhibit smaller TSD and TED densities on the order of 10^{10} cm^{-2} in comparison with 10^{11} cm^{-2} for the N-rich conditions. Better structural quality of the GaN films obtained in the Ga-rich regime is reflected in the improved optical properties of the layer.

It is concluded that optimization of the initial GaN nucleation behaviour on Sc₂O₃ is expected to provide further improvements in the GaN quality. How-

ever, this will not lead to the reduction of cracks in the μm -thick GaN film, which are formed due to the difference in TEC between GaN and Si.

3.4 GaN/Sc₂O₃ interface

In the proceeding sections, it was shown that μm - thick GaN films with threading dislocation density (TDD) of 10^{10} cm^{-2} and strong photoluminescence emission due to the donor bound exciton transition can be grown via Sc₂O₃/Y₂O₃ buffers on Si wafers. The structural and optical properties of epitaxial GaN on Sc₂O₃/Y₂O₃ are strongly influenced by the growth conditions with a very narrow processing window, enabling deposition of good quality GaN. To obtain further improvements in the crystalline quality of the layers, a deeper understanding of the initial stages of the GaN growth on Sc₂O₃ and in particular the nature of the atomic bonding at the GaN/Sc₂O₃ interface is required.

To achieve this goal, the atomic structure of the GaN/Sc₂O₃ interface was simulated by *ab initio* calculations performed in our research group by Dr. J. Dabrowski. The theoretical model was supported by experimental insights gained from *in-situ* RHEED and XPS studies. XPS measurements were performed at a photoelectron take-off angle θ of 45° with a MgK α (1253.6 eV) X-ray source and a Specs Phoibos 100 hemispherical energy analyzer. The photoemission peaks were fitted by Casa XPS software using mixed Gaussian-Lorentzian functions. The GaN surface topography was examined with Omicron atomic force microscope (AFM). The characterized GaN layers were deposited in the Ga-rich regime with the substrate temperature, T_{Ga} , N_{flow} and power of RF plasma source of 720°C , 960°C , 1 sccm, and 300W, respectively.

3.4.1 Experimental results

RHEED patterns

GaN growth was performed on a smooth, single crystalline, fully relaxed Sc₂O₃ buffer layer.¹⁵⁴ The typical RHEED pattern of the starting Sc₂O₃(111)-(4 \times 4) surface is shown in the top part of Fig. 3.21.¹⁵⁵ Smooth transition from the Sc₂O₃ to the GaN RHEED pattern (Fig. 3.21, 0 - 20 s) indicates a sharp interface between these two materials. The spotty RHEED pattern of the GaN nucleation layer obtained after 20 s of the deposition suggests that the growth of GaN is three-dimensional (3D). A characteristic complex RHEED image, visible between 20 s and 120 s, proves the presence of two GaN phases, namely the cubic and the hexagonal.^{156,157,149} Examples of cubic GaN reflections are indicated (by arrows) in the RHEED image

taken after 120 s of growth. After 240 s of deposition, the RHEED pattern associated to the cubic GaN phase disappears and only the hexagonal phase is detected. A gradual change of the RHEED pattern from spotty to streaky (15- 360 s) indicates progressing coalescence of the GaN islands. The clear streaky RHEED pattern obtained after 360 s of deposition provides indication that full coalescence is achieved. When the sample is cooled down to room temperature, a (3×3)GaN surface reconstruction shows up (RHEED not shown). This type of reconstruction is characteristic for N-polar GaN(0001) film surfaces.¹⁵⁸ According to the RHEED observations, the in-plane alignment of the GaN(0001)/Sc₂O₃(111) /Y₂O₃(111)/Si(111) heterostructure is GaN[10 $\bar{1}$ 0]||Sc₂O₃[11 $\bar{2}$] which is in agreement with our previous X-ray diffraction study.¹⁵⁴

To monitor the in-plane lattice parameters of Sc₂O₃ and GaN as well as the strain in the GaN film, the distance W between the (01) and (0 $\bar{1}$) diffraction spots/streaks was measured during growth. An example of such a line scan and the definition of W is shown in the sketch in the bottom part of Fig. 3.21. Figure 3.22 a) shows W/2 plotted as a function of the GaN deposition time. In the initial stages of the GaN growth, the distance W/2 increases from 69 pixels (tensile strained GaN) to 75.5 (after 30 s) pixels (fully relaxed GaN) and remains constant for longer deposition time. For better understanding of the RHEED pattern, the W/2 values were recalculated to the real *d* spacing between the lattice planes. The value of W/2 corresponds in a reciprocal way to the GaN *d*₁₀₋₁₀ spacing (Fig. 3.22 b)) and, before GaN growth, to three times Sc₂O₃ *d*₄₄₈(Fig. 3.22 c)). As shown in Fig. 3.22 c) three times Sc₂O₃ *d*₄₄₈ is also the distance between two oxygen atoms in the Sc₂O₃ crystal along $\langle 11\bar{2} \rangle$ direction. The calculated Sc₂O₃ lattice parameter *a*_{Sc₂O₃} of 9.85Å stands for the fully relaxed Sc₂O₃ layer. In case of GaN, the GaN *d*₁₀₋₁₀ spacing corresponds to the distance between two Ga atoms along $\langle 10\bar{1}0 \rangle$ direction. After 30 s of GaN growth, the GaN(10 $\bar{1}$ 0) lattice *d*-spacing of 2.75Å is reached. The corresponding lattice parameter *a*_{GaN} of about 3.18 Å agrees well within the experimental error with the value of bulk GaN (3.19 Å).¹⁴⁴ This result indicates that the GaN islands are fully relaxed before coalescence.

XPS

Figure 3.23 shows Sc 2p_{1/2}, Sc 2p_{3/2} and N 1s photoemission peaks after 0 s, 10 s, 30 s, 60 s and 360 s of the GaN growth. The Sc 2p_{1/2} (407.6 eV) and Sc 2p_{3/2} (403.3 eV) line positions for a clean Sc₂O₃ surface are attributed to the

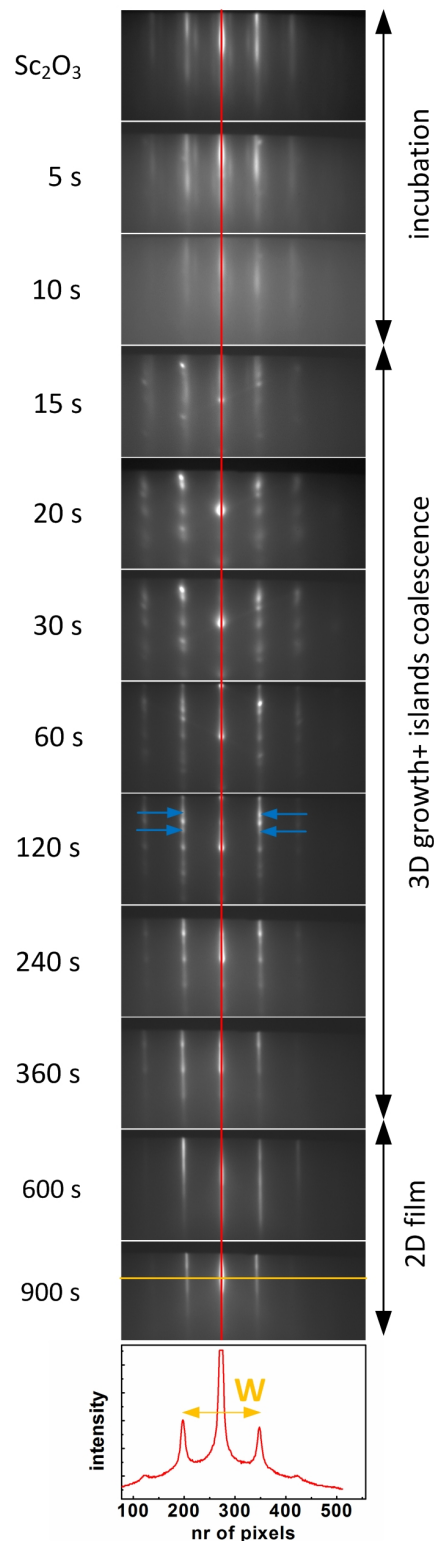


Figure 3.21: RHEED patterns of initial stages of the GaN deposition on Sc₂O₃/Y₂O₃ buffer. Images were taken *in-situ* at 720°C substrate temperature along Sc₂O₃ $[\bar{1}10]$ (GaN $[11\bar{2}0]$) direction. Arrows in the RHEED pattern recorded after 120 s indicate reflections associated with the cubic GaN inclusions.

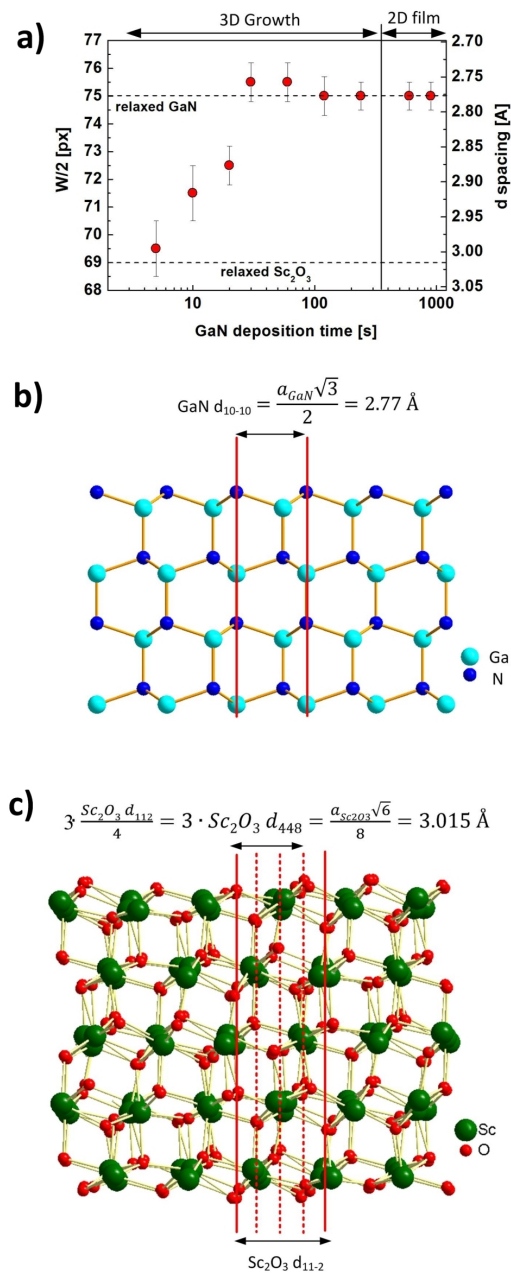


Figure 3.22: a) RHEED image line spacing $W/2$ as a function of the GaN deposition time b) GaN crystal structure viewed along $[11\bar{2}0]$ direction c) Sc_2O_3 crystal structure viewed along $[\bar{1}10]$.

O-Sc-O bonds.¹⁵⁹ Upon GaN growth (after 10 s), Sc 2p lines are shifted to

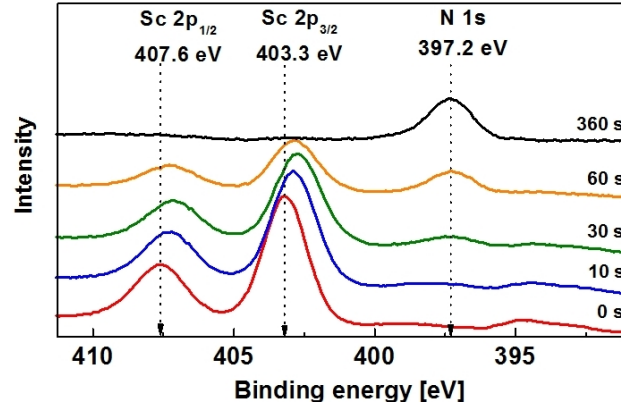


Figure 3.23: Sc 2p and N 1s XPS spectra taken after 0, 10, 30, 60 and 360 s of the GaN growth.

lower binding energies by about 0.4 eV and their position remains constant for longer depositions. This behavior can be related to: a) change of the chemical environment of the Sc atoms at the interface from Sc-O to Sc-O-Ga or/and b) band bending at the interface. Due to the overlap of the N 1s peak with the Sc 2p x-ray satellites, it is difficult to assign a chemical state of the N atoms in the first seconds of GaN growth. After 30 s of deposition, the N 1s peak is found at the position of 397.2 eV which can be clearly attributed to Ga-N-Ga bonding in GaN.¹⁶⁰ The position of this peak does not change upon further GaN growth.

As suggested by the RHEED data discussed above, the growth of GaN on Sc₂O₃ is initiated by the formation of 3D islands. The degree of coverage and the thermodynamic growth mode of GaN films on Sc₂O₃ buffer as a function of deposition time was investigated by XPS. The growth mode of the GaN was determined based on analysis of the progressively attenuated Sc 2p_{3/2} photoemission line ($E_B = 403.3$ eV). These results are summarized in Fig. 3.24 a). Following the approach proposed by Silar,¹⁶¹ for the 3D growth mode, the original substrate intensity I_0 during film deposition is attenuated to the intensity I_s :

$$\frac{I_s}{I_0} = (1 - \Theta) + \Theta \cdot e^{\frac{-t}{\lambda \cdot \cos \omega}} \quad (3.7)$$

where t is the average GaN island height (in nm), λ is the photoelectron mean free path (here $\lambda = 1.7$ nm), Θ is the Sc₂O₃ surface coverage by GaN islands ($\Theta=0$ and $\Theta=1$ for uncovered and fully covered layer, respectively) and ω is

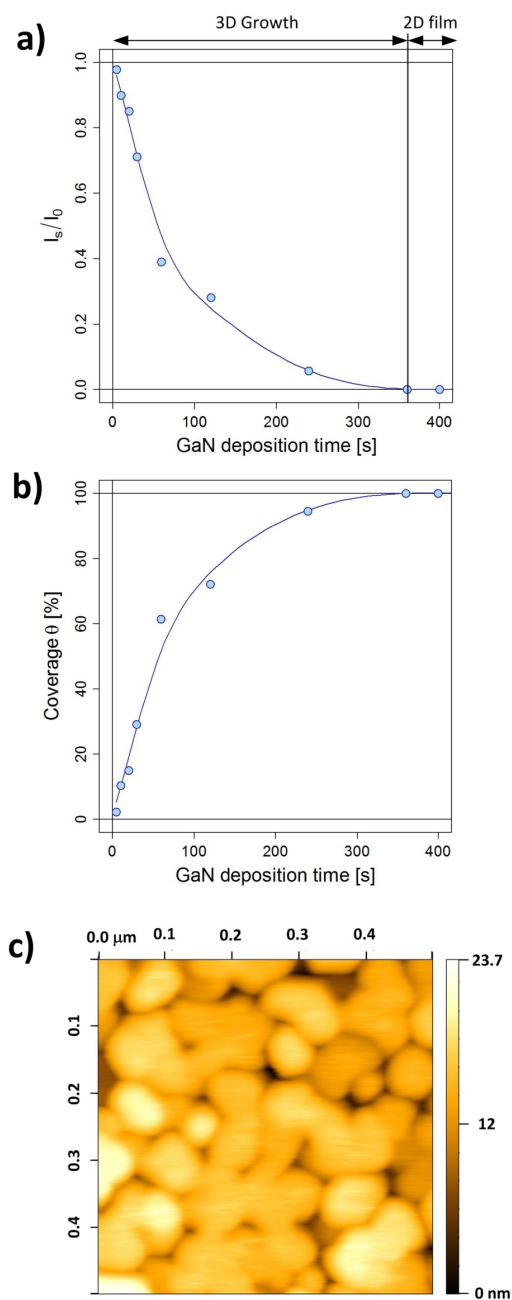


Figure 3.24: a) Attenuation curve of the Sc 2p_{3/2} XPS line and b) Sc₂O₃ surface coverage by the GaN islands as a function of the GaN deposition time c) AFM image of the GaN surface after 240 s of growth.

the angle between sample and analyzer ($\omega=45^\circ$). Based on Eq. 3.7 the experimental points were fitted (fitting parameters: Θ and t). The assumption for this calculation is that the GaN volume increases linearly with deposition time. The presented data suggests that the full coalescence of the GaN islands take place after about 360 s. After this time the Sc_2O_3 surface coverage is 100% (Fig. 3.24 b)) and the GaN island height is about 35 nm. An AFM image of the GaN surface just before island coalescence (after 240 s of the deposition) is shown in Fig. 3.24 c). Deep valleys are visible at the boundaries between partially coalesced islands. The islands (lateral) length to height ratio is estimated to be around 4. According to the investigation of Cheung *et al.*, relatively large and tilted GaN grains may lead to the creation of new defects which extend from the island boundaries into the growing GaN film on top.¹⁶² To probe the bonding chemistry at the GaN/ Sc_2O_3 interface, the x-ray photoemission peaks were monitored at various stages of the GaN growth. Figure 3.25 shows the evolution of Ga $2p_{3/2}$ peak shape. Fitting of these spectra reveals two contributions located at approximately 1116.9 eV and 1118.2 eV, which can be attributed to the presence of N-Ga-N and N-Ga-O-Sc bonds, respectively.¹⁶³ It is clearly seen in Fig. 3.25 that the N-Ga-O-Sc Ga $2p_{3/2}$ peak dominates up to 30 s of GaN growth (based on RHEED: up to 30s N-Ga-O-Sc interface layer is tensile strained). After this time, the intensity of the peak associated with GaN strongly increases suppressing gradually the N-Ga-O-Sc signal (based on RHEED: relaxation takes place). After 360 s, the N-Ga-O-Sc peak vanishes completely. This indicates that the interface region is not accessible anymore by XPS and implies full coalescence of the GaN islands. This is in line with the complete disappearance of the O 1s photoemission signal at this growth stage (data not shown) as well as with the XPS results presented in Figs. 3.23 and 3.24. Furthermore, after 900 s of growth a small signal at the position of 1116.3 eV is detected. This feature can be assigned to the presence of elemental Ga on the GaN film surface.¹⁶⁴

Figure 3.26 shows the integrated areas of the Ga $2p_{3/2}$ and N 1s peaks plotted as a function of GaN deposition time. Based on these data, two stages of the GaN growth can be distinguished.

During the first stage (up to 30 s) the Ga $2p_{3/2}$ N-Ga-O-Sc, Ga $2p_{3/2}$ N-Ga-N, and N 1s peak intensities gradually increase with GaN deposition time. The Ga $2p_{3/2}$ signal originating from N-Ga-O-Sc is about four times stronger than the corresponding signal caused by N-Ga-N bonding. This indicates that at the very beginning of the GaN growth numerous Ga-O bonds are formed. In

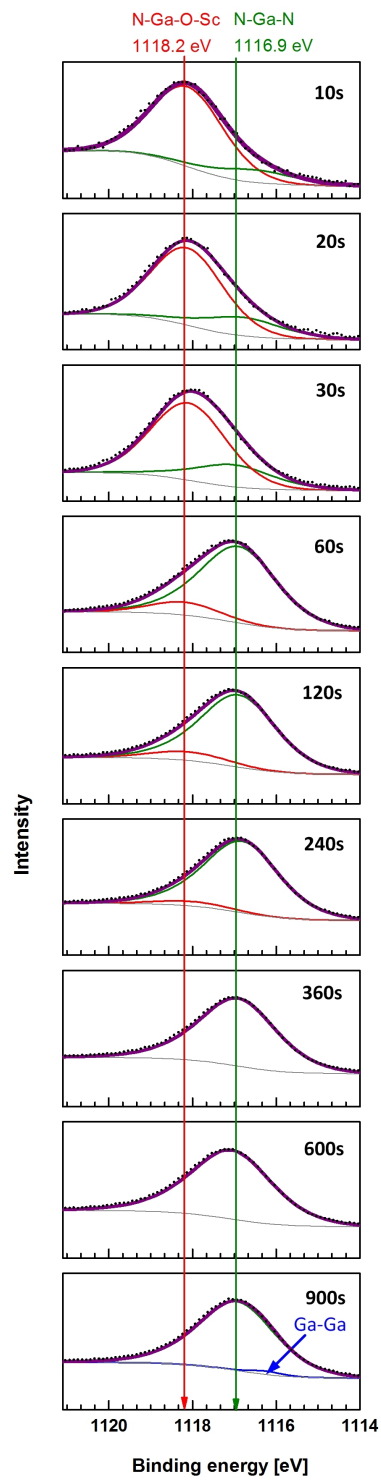


Figure 3.25: Evolution of the Ga 2p_{3/2} peak upon GaN growth.

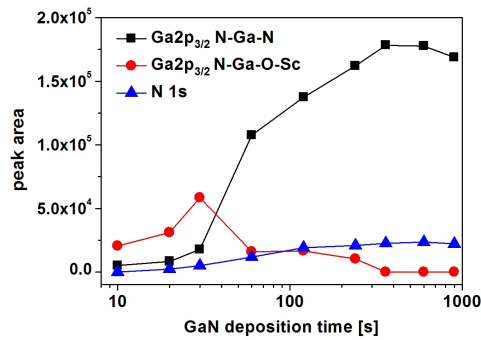


Figure 3.26: Integrated peak areas of the Ga $2p_{3/2}$ N-Ga-O-Sc, Ga $2p_{3/2}$ N-Ga-N and, N 1s signals plotted as a function of GaN growth time.

addition, formation of GaN islands takes place. Estimated coverage of the Sc_2O_3 surface by the GaN island after 30 s of the deposition is about 30% and the average islands height, calculated based on previously calibrated growth rate, is 6 nm.

In the second stage, the Ga $2p_{3/2}$ N-Ga-O-Sc signal quickly decreases, whereas N-Ga-N peak area increases. This is associated with increasing Sc_2O_3 surface coverage by GaN islands and increasing thickness of the islands. After 360 s of growth, the N-Ga-O-Sc Ga $2p_{3/2}$ signal is completely suppressed. The slight decrease in the Ga $2p_{3/2}$ N-Ga-N signal intensity observed after 900 s of the growth can be attributed to the attenuation caused by the presence of elemental Ga on the GaN surface. It is noted that the formation of a metallic Ga film on the GaN(0001) surface was reported to be beneficial for the growth of flat GaN layers.¹⁶⁵

3.4.2 Model of the GaN/ Sc_2O_3 interface

The atomic structure of the interface between GaN and Sc_2O_3 was addressed by *ab initio* calculations performed within the pseudopotential density functional theory (DFT) approach supported by the experimental insights reported in the previous sections. Exchange and correlation energy of electrons was described by the General Gradient Approximation (GGA) of Perdew, Burke and Erzenhof (GGA-PBE), as implemented in the Quantum Espresso package and the plane wave (pw.x) method. Since the interface unit cell of GaN(0001)/ Sc_2O_3 (111) contains many atoms, the ultrasoft form of the atomic pseudopotentials was used. Two approximations of Ga atoms were used: the sp pseudopotential with 4s and 4p electrons treated as valence electrons and

d electrons frozen in the core, and the spd pseudopotential with 4s, 4p and 3d electrons treated as valence electrons. In both cases the contribution of frozen core electrons to the exchange and correlation energy was accounted for by the nonlocal core correction. We verified that with cut-off energies of 30 Ry for the wave functions and 240 Ry for the electron density, both potentials provide a good description of the lattice parameters and bulk elastic modulus of wurtzite and zinc blende GaN (Tab. 3.2). Omission of d electrons from the valence shell results in a small (below 1%) shrinking of the lattice. As the usual GGA effect is a small (below 1%) expansion of the lattice, the sp pseudopotential of Ga reproduces the GaN lattice parameters with accuracy of about 0.2%. This is a fortuitous agreement due to error cancellation. The calculations approximate

Table 3.2: Properties of wurtzite and zinc blende GaN.

	Zinc blende		Wurtzite	
	a [Å]	B [GPa]	a [Å]	c [Å]
sp	4.49	179	3.188	5.179
spd	4.52	178	3.204	5.224
experiment	4.50	190	3.190	5.189
theory Ref. 166	4.46	200	-	-
theory Ref. 167	-	-	3.204	5.218

the "infinite" crystal by applying periodic boundary conditions to a finite unit cell. The numerical effort increases approximately as the third power of the number of atoms in this unit cell. In practice, the calculations are still efficient when the area of the interface unit cell is of the order of 100Å², but not much larger. In practice this means that, in order to be useful for the calculations, the interfacial models may encompass at most 1 or 2 surface unit cells of truncated bulk Sc₂O₃(111) or, correspondingly, 16 to 32 surface unit cells of truncated bulk GaN(0001); assuming a N-polar film, this translates into 16 or 32 interfacial Ga atoms.(Fig. 3.27 a)) This restriction excludes any direct and systematic treatment of interface misfit dislocations. The misfit strain can be arbitrarily distributed between the film and the substrate, with one extreme comprising of fully relaxed nitride on compressed oxide and the other extreme of tensile stressed nitride on fully relaxed oxide. Here, we discuss the results obtained for the intermediate case, in which the nitride is stretched by 4.4% and the oxide is compressed by 4.4%.

After having established the main assumptions of the interface model, we turn

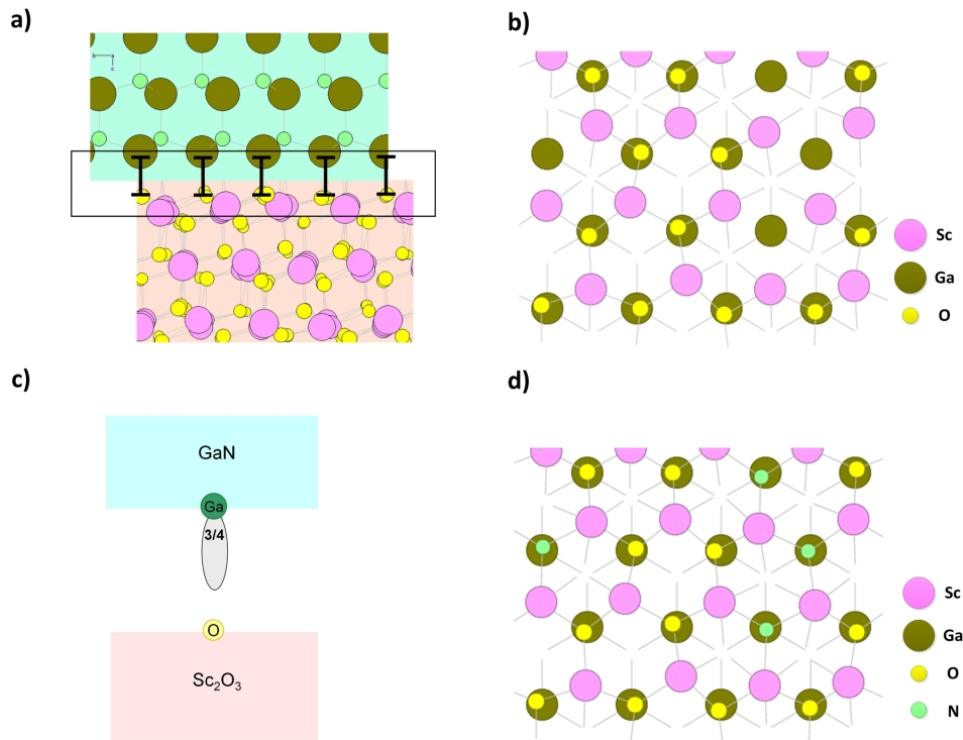


Figure 3.27: Model of the GaN/Sc₂O₃ interface. a) Nitride is stretched by 4.4% and the oxide is compressed by 4.4% to match Ga and O atoms. b) For the calculations 1 unit cell of truncated bulk Sc₂O₃(111) was taken which corresponds to 16 unit cells of truncated bulk GaN(0001). For each 16 atoms of Ga, 4 of them are without O partners (O vacancies in Sc₂O₃ crystal). c) Each interfacial Ga-O bonds donates $0.75e^{-1}$. This implies that for each 16 Ga atoms 12 electrons are donated ($16 \times 0.75e^{-1} = 12e^{-1}$). d) To keep the GaN/Sc₂O₃ interface neutral, O vacancies may be filled with N atoms. With $4 \times N^{3-}$ all donated electrons are retained at the interface. *Ab initio* calculations have been performed by J. Dabrowski, IHP.

attention to some more detailed but still general structural features of the interface. Although the structure of Sc₂O₃ is quite complicated, it can be rationalized in a simple way. Namely, it is akin to that of cubic calcium fluoride (CaF₂), which in turn can be viewed as anions (F) and cations (Ca) arranged in a zinc blende lattice having its all tetrahedral interstitial sites filled by cations (Ca). As far as stoichiometry is concerned, counting per each two cation atoms there is one anion atom less in Sc₂O₃ than in CaF₂. In the fluorite lattice this formally corresponds to one anion (O) vacancy per each two cation (Sc) atoms. The interface unit cell contains 16 interfacial cations on each side of the interface plane: 16 interfacial Ga atoms on the nitride side and 16 interfacial Sc atoms on the oxide side. These atoms constitute the cation part of the nitride interfacial atomic plane and the oxide interfacial atomic plane. The nitride interfacial plane is polar; each of its cations (Ga) has its anion neighbour (N) above itself, i.e., further away from the interface, on the film side. The oxide plane is non-polar; each cation (Sc) has, per average, 0.75 O atoms above it (closer to the interface) and 0.75 O atoms below it (further away from the interface). Let us now assume for a moment that the oxide has a strict fluorite structure. In this case, each cation of the oxide has one anion above and one anion below itself, meaning that the number of interface anions (O) in the oxide is equal to the number of interface cations (Ga) in the nitride. These atoms are in registry, that is, the Ga atoms are directly above the O atoms (Fig. 3.27 b)). In the real structure, a quarter of these O atoms is missing. It follows that the unit cell of a stoichiometric interface has 4 Ga atoms (out of 16) without an O partner; each of the remaining 12 Ga atoms can make a bond to the underlying O atom (Fig. 3.27 a)).

Let us now consider the expected distribution of electrons in the electron states. Since the (111)-oriented oxide is built of non-polar planes, a truncated bulk surface (i.e., the surface obtained by splitting of the bulk by a surface plane into two stoichiometric parts) is not charged: the charge transfer between cations and anions occurs without the formation of any dipole moment in the direction normal to the surface. In other words, the formation of the oxide surface does not produce any dangling bonds that are only partially occupied. One expects that the electronic structure of the surface is semiconducting, with an energy gap, as confirmed by *ab initio* calculations. This is in contrast to the situation in the nitride. The (0001)-oriented nitride is built of polar planes, each contributing a dipole moment in the direction normal to the surface. In other words, the formation of the nitride surface produces dangling

bonds which are only partially occupied unless charge is transferred between surfaces terminating both sides of the polar slab. Now, when the polar surface of the nitride is brought into contact with the non-polar surface of the oxide, the atoms terminating both surfaces tend to make bonds. However, only the atoms terminating the nitride surface have their valences unsatisfied; their partners from the oxide do not want any additional electrons and do not want to get rid of any electrons. As a result, the formation of bonds between these two surfaces requires additional charge to complete the bonding orbitals. This charge needs to be transferred from the outside, notably from the surface states or from defect states in the film or in the substrate. Charge transfer is associated with increased electrostatic energy; for sheet charges this energy grows linearly with the separation between the charges, as in a plate capacitor. One therefore expects that, if possible, the interface will try to adopt such a chemical composition - or generate such low-energy defects - that the bonding orbitals are completely filled without the need to transfer charge from distant places. It is straightforward to verify that the formation of complete bonds between the $\text{Sc}_2\text{O}_3(111)$ surface and the Ga-terminated $\text{GaN}(0001)$ surface donates 12 electrons per interfacial unit cell (i.e., per 16 interfacial Ga atoms)¹. At the same time, there are 4 structural oxygen vacancies in the oxide layer adjacent to the interfacial plane. This means that when these structural vacancy sites are filled with N atoms (Fig. 3.27 d)), the interface may remain electrically neutral. Indeed, each of the N interstitial atoms acts as a triple acceptor: an O atom in an oxide tends to be in double negative charge state, a N atom in a similar site tends to be in a triple negative state. With four N interstitials all donated electrons are thus retained at the interface and there is no need for charge being transferred over a large distance.

The resulting model of the interface (nitrogen interstitial model (NI)) is illustrated in Fig. 3.28 a) and b). In both cases the actual film consists of 4 monolayers of wurtzite GaN. The version shown in Fig. 3.28 a) is constructed to reflect the situation of a thick film: the upper surface of the film (facing vacuum) is saturated with pseudo-hydrogen atoms, which saturate the dangling bonds of surface N and simulate in this way the presence of further GaN layers. From the point of view of charge transfer to the interface states, the film depicted in Fig. 3.28 a) is thus infinitely thick: the charge transfer is practically forbidden and indeed it does not occur. On the other hand, the upper

¹Each interfacial Ga provides $0.75e^-$ (Fig. 3.28 c)), therefore for 16 atoms 12 electrons are donated ($16 \times 0.75e^- = 12e^-$)

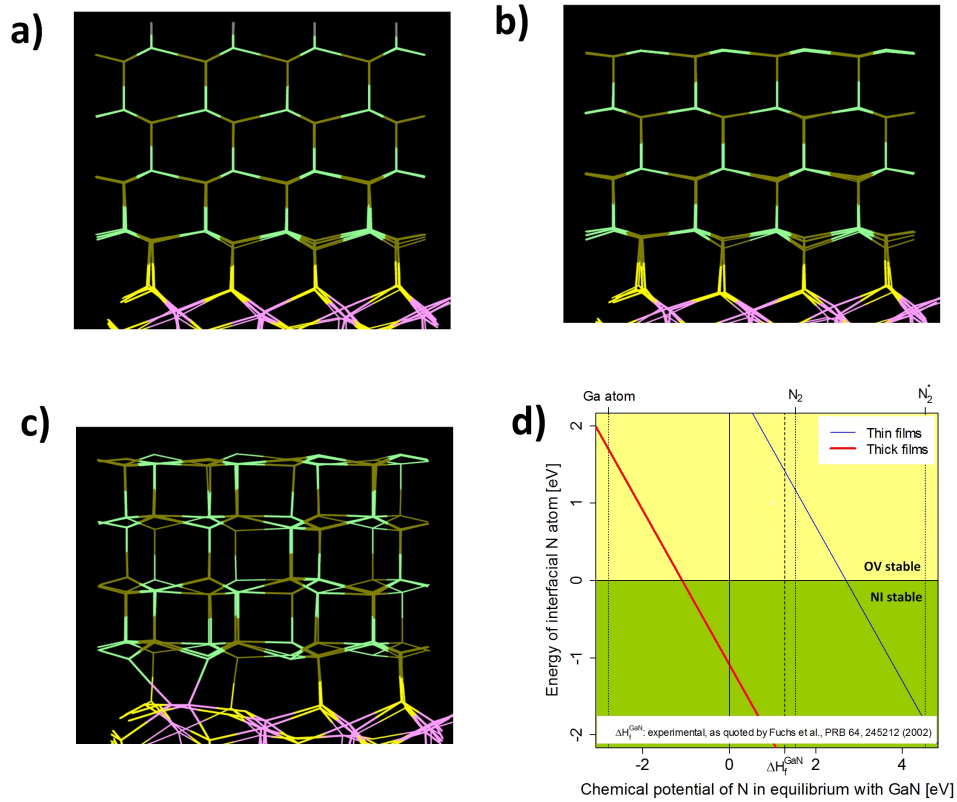


Figure 3.28: Interface models. Only bonds are shown. a) Interface with nitrogen interstitials: NI model. The outer surface of the nitride is saturated with pseudo-hydrogen atoms (blue bonds) to simulate a thick film. b) The same as in a), but without the pseudo-hydrogen atoms; this is a "true" thin film. c) Interface without nitrogen interstitials: OV model. The thin film version is shown (no termination of the outer surface by pseudo-hydrogen atoms). d) Energy of the interfacial nitrogen for a thin film (blue dashed line) and for a thick film (red solid line), as a function of N chemical potential. The chemical potential varies from Ga-rich regime (on the left, Ga atom) to N-rich regime (on the right, N₂ *) condition. The energy plotted is equal to the energy difference between the NI and OV structures, per N atom. ΔH_f^{GaN} : experimental, as quoted by Fuchs et al. Ref. 168. *Images courtesy of J. Dabrowski, IHP.*

surface of the GaN film in the version shown in Fig. 3.28 b) is the stoichiometric N-polar surface obtained by truncation of the bulk between the (0001) layers; it differs from that in Fig. 3.28 a) by the lack of any saturating atoms. The surface in Fig. 3.28 b) is metallic and it can be a source of charge to be transferred to the interfacial states. This is the situation as it is in thin films (small separation between the interface and the source of charge). It is evident that when the interface is of NI type, the structure of the film does not change when the film changes from thin to thick.

This structure is however different when the interface contains no nitrogen interstitials, as shown in Fig. 3.28 c) for a thin film (oxygen vacancy model (OV)). The major difference is that the thin film with OV interface has lost its polarity: in contrast to the films with NI interface, where all bonds point from N atoms to Ga atoms (which causes the polarity), half of the bonds in the film with OV interface point in the opposite direction, from Ga atoms to N atoms. Formally speaking, the film with OV interface is saturated with polarity type boundaries, and its surface is of mixed N- and Ga-polar type. As it was the case for the NI film, the electronic structure of the OV film is semiconducting, with forbidden energy gap; the difference is that the energy gap in the NI film opened due to charge transfer within the interface, while in the OV film it opened due to charge transfer between the interface and the GaN surface. One can therefore expect that the energy of the NI film is roughly independent on the film thickness (apart from the obvious accumulation of the strain energy due to the lattice misfit), while the energy of the OV film grows with thickness due to the increasing spatial separation between the sheet charges at the interface and on the surface.

Since the OV structure is stoichiometric, one may define the energy of interfacial nitrogen interstitial as the energy gained or lost when the vacancy sites in the OV interface are completely filled by N atoms taken from a reservoir of N atoms (where each N atom has the energy equal to the chemical potential of nitrogen); this energy is calculated per N atom transferred. Figure 3.28(d) shows the dependence of the resulting energy on the chemical potential μ_N of nitrogen. The latter is calculated assuming that N and Ga atoms are in equilibrium with relaxed bulk wurtzite GaN ($\mu_N + \mu_{\text{Ga}} = \mu_{\text{GaN}}$). The condition $\mu_N=0$ means here that the N atom built as N interstitial into the interface would be taken from perfect GaN and that the Ga atom produced in this reaction (by decomposition of a GaN unit) would go to a droplet of metallic Ga. Or conversely, that the N interstitial that would be removed from the

interface would ultimately combine with a Ga atom taken from a metallic Ga droplet to form a new GaN unit in a perfect GaN crystal. This is briefly described as equilibrium of N with GaN and metallic Ga droplets. Within this convention, $\mu_{\text{N}} = \Delta H_{\text{f}}^{\text{GaN}}$ corresponds to equilibrium of N with GaN and with N₂ molecules. Since μ_{N} cannot be increased in thermal equilibrium above the equilibrium with N₂ (nitrogen molecules or atoms would then convert into N₂ and μ_{N} would return to its N₂ equilibrium value) and, similarly, μ_{Ga} cannot increase in thermal equilibrium beyond the equilibrium with Ga droplets, the chemical potential of N is – in thermal equilibrium – limited to the range between 0 and $\Delta H_{\text{f}}^{\text{GaN}}$. In the diagram we included also the non-equilibrium extremes. In the Ga-rich extreme on the left, the N atom removed from the interface combines with a free Ga atom to form a new GaN cell in relaxed wurzite GaN. In the N-rich extreme on the right, the N atom arrives to the interface from a N₂^{*} molecule.

As expected, interfacial nitrogen interstitials are by far more stable in thick films than in thin films (the thick red line is far below in energy than the thin blue line). Moreover, even for thin films of nearly 1 nm (as in Fig. 3.28), the NI interface is unstable with respect to the OV interface (the energy of the interfacial N is positive) in the whole thermal equilibrium regime. The same holds for the whole Ga-rich regime and in most of the N-rich regime, even beyond the equilibrium with N₂. In thick films this is reversed: the OV interface becomes then unstable with respect to the NI interface in the whole thermal equilibrium regime, and can prevail only in strongly Ga-rich regime under non-equilibrium conditions.

The changing relative stability of the interface indicates that the growth begins without incorporation of N in the vacancy sites of the oxide surface. In this initial stage the film has a mixed polarity, although the bonds to the substrate are formed only with Ga atoms. As the film becomes thicker, N atoms are becoming incorporated into the interface and the semiconducting NI interface is eventually produced. We suppose that the transport of N proceeds by emission of N vacancies from the interface, which then bubble across the film towards the surface.

3.4.3 Discussion of the growth process

The results presented above suggest the following physical mechanism of the growth process.

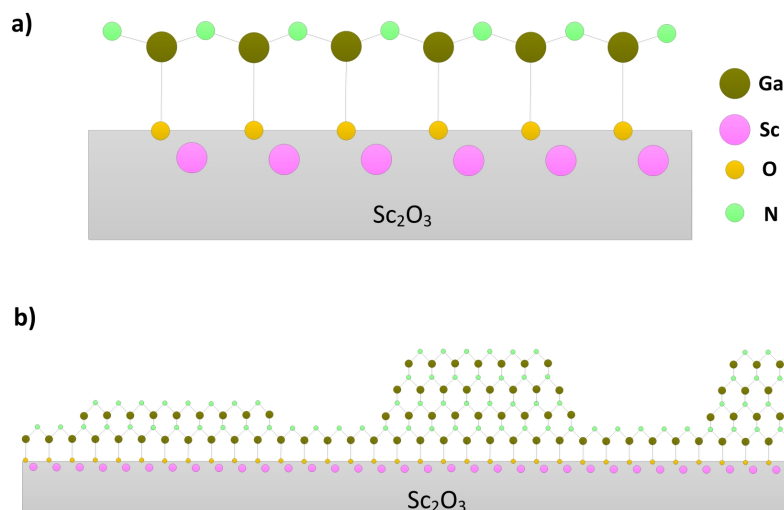


Figure 3.29: Initial growth stages of GaN on Sc₂O₃ buffer layer. a) Firstly, N-Ga-O-Sc bonds are formed at the GaN/Sc₂O₃ interface. b) When a complete monolayer is achieved the growth proceeds by the nucleation of 3D islands. The complete coalescence takes place when the GaN islands height is about 35 nm.

Initial stage. Incoming molecules (Ga atoms and N₂^{*} molecules) become attached to the substrate. The sticking coefficient of Ga is close to unity, since the calculations predict the energy gain by adsorption of isolated atom of Ga from vacuum on Sc₂O₃ to be about 2.2 eV. The sticking coefficient of N from N₂^{*} is expected to be below unity, because albeit the calculated energy gain by adsorption of isolated N atom from electrically neutral N₂^{*} in vacuum is about 2.5 eV or more (assuming the A³Σ_u⁺ state),¹⁶⁹ the adsorbed atomic N is unstable with respect to the formation of volatile N₂ in the ground state (3.4 eV per atom is gained when N escapes in form of N₂). The adsorbed atoms can diffuse on the surface. When Ga and N atom meet one another, they form a GaN dimer, gaining about 2.2 eV per dimer. The dimers tend to build bigger agglomerates, whereby the attachment of a dimer to the existing cluster is typically between 0.5 and 1 eV (meaning that the attachment reaction is reversible at typical growth temperatures, i.e., in spite of the clustering, the surface mobility of the material is retained). When a complete monolayer is formed most of Ga atoms are bonded to substrate O atoms (Fig. 3.29 a)). Ga atoms also form planar (sp²) bonds to N atoms. It is therefore expected to find the corresponding Ga 2p 3/2 XPS signal somewhere between the positions for GaN bulk and Ga₂O₃ bulk signals. One can thus interpret the observed N-Ga-O-Sc line as originating from surface region coverage by monolayer of GaN.

Inversion domains. According to the results of the *ab initio* calculations, the first few monolayers of GaN might grow in a sp²-bonded hexagonal phase (Fig. 3.28(c)). This structure can be viewed as a mixture of N and Ga polarities and it can be converted to either of them by a small vertical displacement of N atoms, so that the sp² electron configuration is changed to sp³. As film grows thicker, the N atoms indeed move upwards and the film transforms smoothly into N-polar sp³-bonded wurtzite structure (Fig. 3.28 (a) and (b)). However, if there is some perturbation that upsets the balance in the opposite direction, providing a driving force to move the N atoms downwards, an inversion domain (Ga polarity) can be produced. Such boundaries in GaN film have been observed in numerous systems.^{170, 149, 160, 171} For GaN films grown on Sc₂O₃ the presence of inversion domains was proved by transmission electron microscopy investigations.

Island growth. *In-situ* RHEED and XPS studies reveal that the growth of GaN on Sc₂O₃ proceeds by the nucleation of 3D islands (Fig. 3.29 b)). According to RHEED, at the very beginning these islands are tensile strained and their full relaxation is achieved already after 30 s of the deposition. Relaxation occurs by the formation of misfit dislocations at the GaN/Sc₂O₃ interface. At this growth stage the Sc₂O₃ surface coverage by GaN islands θ is about 0.3 and the average islands height t is about 8 nm. The complete coalescence takes place when the GaN islands height reaches about 35 nm as estimated by the analysis of the Sc 2p 3/2 and Ga 2p 3/2 photoemission peaks. After coalescence a (3×3) surface reconstruction is observed, which indicates that the growing GaN film is mainly N-polar. However, based on RHEED results the existence of a small amount of Ga inversion domains in a mainly N-polar material can not be excluded. Furthermore, in the initial growth stage the mixture of cubic and hexagonal GaN phases are detected by RHEED. The primary orientation between hexagonal(h) and cubic(c) GaN is (0001)_h{10 $\bar{1}$ 0}_h|| (111)_c{11 $\bar{2}$ }_c. When the full coalescence of the islands is accomplished the RHEED pattern associated with cubic GaN phase disappears completely. From this stage onwards the GaN film grows in a pure hexagonal phase without cubic inclusions.

3.4.4 Summary

The initial GaN growth stage on Sc₂O₃/Y₂O₃/Si(111) substrates was investigated experimentally and by *ab initio* calculations. The developed *ab initio* in-

terface model assumes the (0001)GaN/(111)Sc₂O₃ out-of-plane and (10 $\bar{1}$ 0)GaN ||(11 $\bar{2}$)Sc₂O₃ in-plane alignment of the heterostructure as derived from x-ray diffraction studies and N-polarity of the growing GaN films as pointed out by RHEED experiments. Theoretical investigations indicate that the GaN/Sc₂O₃ interface chemistry is determined by the N-Ga-O-Sc bonding. This result is in line with XPS measurements giving evidence for the formation of N-Ga-O-Sc bonds in the initial GaN growth stage.

Additionally, the experimental results show that the growth proceeds by the nucleation of 3D GaN islands. These islands are of poor crystalline quality; stacking fault defects and inversion domains are detected in the initial growth stage. Moreover, relatively fast relaxation of the islands indicates formation of misfit dislocations at the GaN/Sc₂O₃ interface. Threading screw dislocations detected in μm - thick GaN layers can arise from coalescence of the misaligned and twisted GaN islands.

Therefore, further optimization of the Sc₂O₃ surface treatment prior to GaN deposition is expected to provide better control of the nucleation behavior and thus improve the final quality of GaN layers deposited on large area Sc₂O₃/Y₂O₃/Si(111) substrates.

Chapter 4

Summary and Outlook

4.1 Summary

The preparation of GaN virtual substrates on large-scale Si wafers is intensively pursued as a cost-effective approach for high power/high frequency electronics (HEMT's etc.) as well as optoelectronics applications (LED, LASER). However, the growth of high quality GaN layers on Si substrates is hampered by several difficulties mainly related to the large lattice mismatch (17%) and huge difference in thermal expansion coefficient (56%). As a consequence, GaN epitaxial layers grown on Si show a too high number of defects (threading dislocations etc.), severely deteriorating the overall quality of the GaN films. To solve these integration problems different semiconducting (e.g. AlN, GaAs, ZnO, HfN) and insulating (e.g. Al₂O₃, MgO, LiGaO₂) buffer layers have been already applied.

In this thesis, a novel buffer approach for the integration of GaN on Si has been proposed and investigated. The new approach employs Sc₂O₃/Y₂O₃ bi-layer templates as a step-graded buffer to reduce the lattice mismatch between GaN and the Si(111) substrate.

An overview of the work performed in this thesis is depicted in Fig. 4.1. **At first**, the structural quality of the MBE grown Sc₂O₃/Y₂O₃ buffer system deposited on Si(111) substrates was investigated by means of RHEED, XRD, and TEM. **Secondly**, the GaN growth mechanism on Sc₂O₃/Y₂O₃/Si(111) template (under Ga-rich conditions) was studied *in-situ* by RHEED and XPS. The experimental results were complemented by *ab-initio* calculations. Moreover, the quality of the ~ 30 nm-thick GaN films was analyzed by XRR and XRD. **Finally**, the structural and optical properties of μm-thick GaN layers

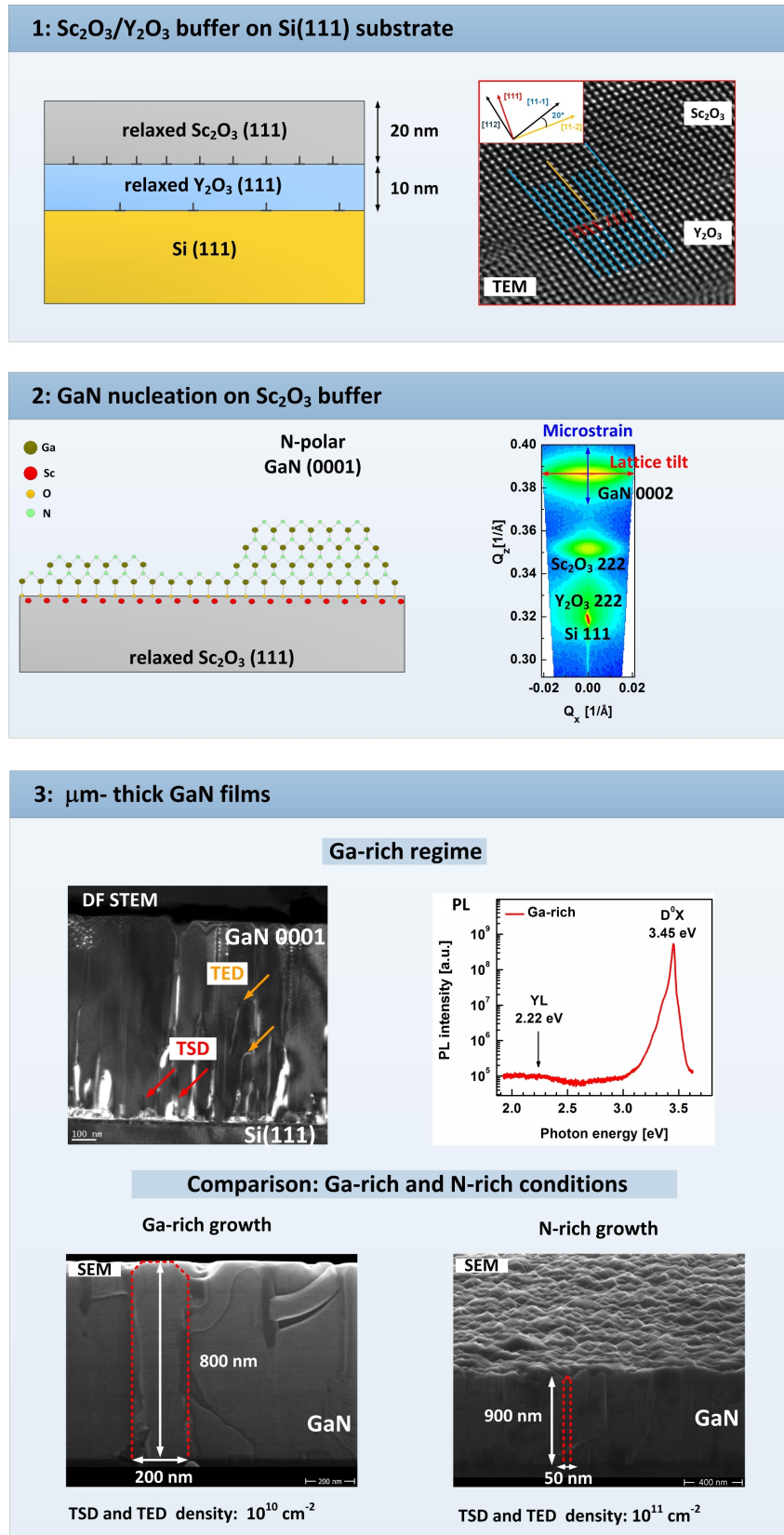


Figure 4.1: Overview of the most important results obtained in this thesis.

deposited in the Ga-rich regime were examined by XRD, PL, TEM, and EDX and compared with the quality of the GaN films grown in N-rich regime.

4.1.1 Growth characteristics of $\text{Sc}_2\text{O}_3/\text{Y}_2\text{O}_3$ buffers

The morphology and structure studies indicate that the $\text{Sc}_2\text{O}_3/\text{Y}_2\text{O}_3$ buffers on Si(111) are atomically flat, closed and single crystalline with (111) vertical orientation. The oxides are of type-B stacking with respect to the Si(111) substrate and fully relaxed for Sc_2O_3 and Y_2O_3 layer thicknesses as low as a few nanometers. Plastic relaxation of the oxide buffer was found by TEM to occur via formation of misfit dislocations at the $\text{Sc}_2\text{O}_3/\text{Y}_2\text{O}_3$ and $\text{Y}_2\text{O}_3/\text{Si}$ interfaces. A strain free Sc_2O_3 is highly desirable as it reduces the lattice mismatch to GaN to the smallest possible value. Furthermore, diffuse X-ray scattering studies using synchrotron radiation source proved that the density of the extended structural defects (e.g. stacking faults) on the preferred {111} glide planes orientation in the Sc_2O_3 layer is below the detection limit. Additionally, thermal stability tests show that the Sc_2O_3 and Y_2O_3 are stable at least up to 900°C which is sufficient for GaN growth by MBE.

These studies demonstrate that the novel engineered $\text{Sc}_2\text{O}_3/\text{Y}_2\text{O}_3$ buffer approach on Si(111) provides a template of high structural quality for GaN overgrowth.

4.1.2 GaN growth mechanism on $\text{Sc}_2\text{O}_3/\text{Y}_2\text{O}_3$ buffers

Investigations of the GaN growth on $\text{Sc}_2\text{O}_3/\text{Y}_2\text{O}_3$ buffer layers allow to derive the following growth mechanism. XPS analysis complemented by *ab-initio* calculations shows that the N-Ga-O-Sc interface bonding configuration is energetically favored at the GaN/ Sc_2O_3 interface (Fig. 4.2 stage 1.). This stacking sequence results in N-polar GaN films. It is however important to note that in particular the *ab-initio* analysis of the GaN/ Sc_2O_3 interface structure indicated a complex growth scenario so that the occurrence of Ga-polar GaN grains can not be excluded. This situation is indicated in Fig. 4.2 stage 2. Additionally, based on RHEED investigations it was found that such N-Ga-O-Sc wetting "layer" is tensile strained due to the higher lattice constant of Sc_2O_3 underneath.

The initial growth stage of GaN on Sc_2O_3 proceeds by the nucleation of 3D islands which are relaxed and relatively large before coalescence. The relaxation occurs by the formation of MDs at the GaN/ Sc_2O_3 interface (Fig. 4.2

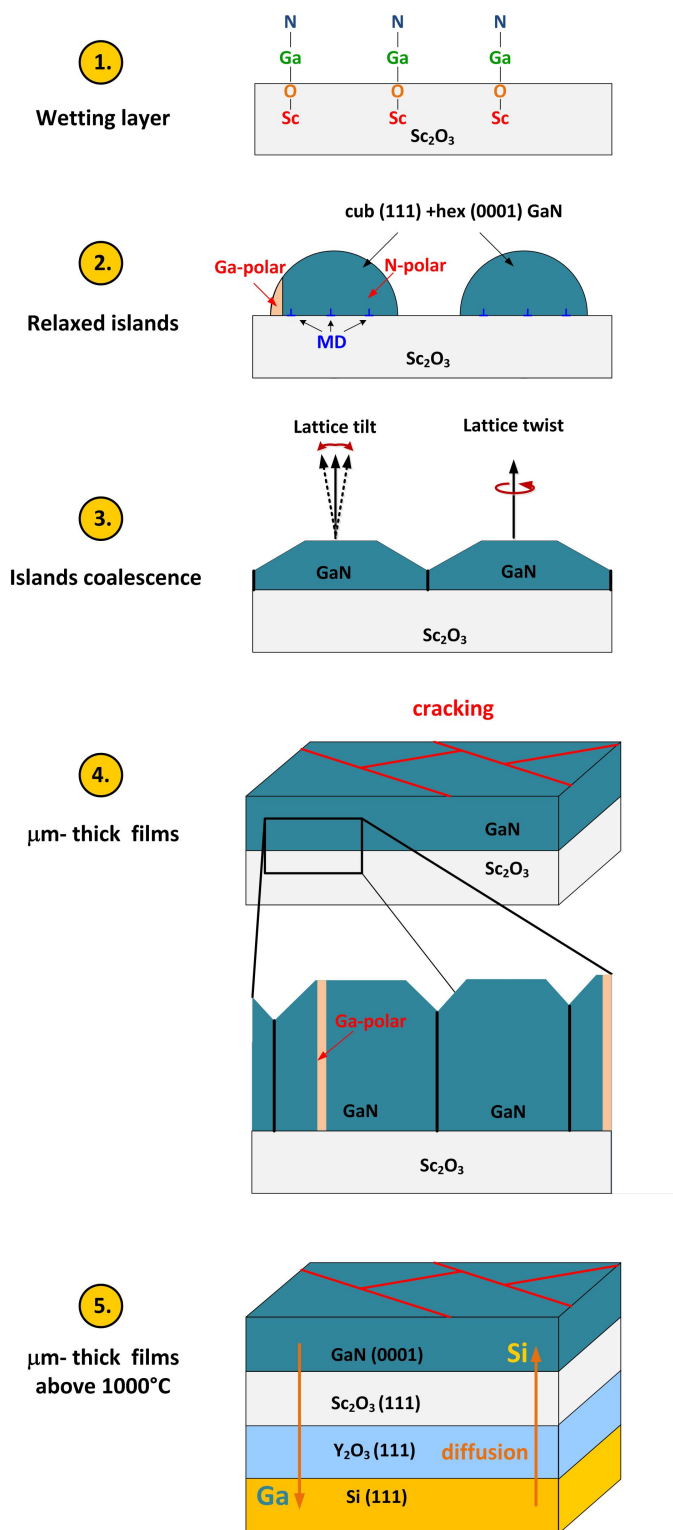


Figure 4.2: Summary of the GaN growth mechanism on $\text{Sc}_2\text{O}_3/\text{Y}_2\text{O}_3/\text{Si}(111)$ templates.

stage 2.). These islands are single crystalline and crystallize in the hexagonal phase. The epitaxial relationship along the growth direction is:

$$\text{GaN}(0001)/\text{Sc}_2\text{O}_3(111)/\text{Y}_2\text{O}_3(111)/\text{Si}(111)$$

and the in-plane alignment of the heterostructure is characterized by:

$$\text{GaN}[10\bar{1}0]||\text{Sc}_2\text{O}_3[2\bar{1}\bar{1}]||\text{Y}_2\text{O}_3[2\bar{1}\bar{1}]||\text{Si}[\bar{2}11]$$

However, it must be noted that in this growth stage the cubic inclusions (e.g. stacking fault defects) are detected by XRD. The formation of the cubic GaN phase may be a result of:

- the cubic stacking sequence of the Sc_2O_3 buffer
- a release of the tensile strain in the initial GaN growth stage.¹⁷²
- the rough, 3D GaN growth which promotes the simultaneous nucleation of hexagonal as well as cubic GaN islands.^{173,55,56,173}

As the growth of GaN proceeds, the GaN nucleation islands become bigger and form blocks with a smooth surface. The W-H analysis reveals that these GaN blocks are tilted and twisted due to the lattice mismatch with respect to the Sc_2O_3 which causes a high content of threading screw and edge dislocations in the coalesced GaN films, respectively (Fig. 4.2 stage 3). It is noted that the tilt and twist values of the GaN block are higher than those of the Sc_2O_3 buffer layer. The coalescence process of misaligned GaN islands is known to be decisive for the quality of μm -thick GaN layers.

4.1.3 Properties of μm -thick GaN on $\text{Sc}_2\text{O}_3/\text{Y}_2\text{O}_3$ buffers

Ga-rich regime

SEM and TEM results reveal that μm -thick GaN layers deposited under Ga-rich conditions are composed of 200 nm-wide, and flat coalesced blocks (Fig. 4.2 stage 3. and 4.). In addition, TEM investigations reveal that these films contain inversion domain boundaries, Ga-polar regions in the N-polar GaN films. Threading screw and edge dislocation densities estimated based on the XRD ω scans are both in the range of $3 \times 10^{10} \text{ cm}^{-2}$. Despite the large amount of threading dislocations, 10K PL spectra show relatively sharp donor bound exciton transitions and low intensity YL emission, which indicate that the GaN

layers grown on $\text{Sc}_2\text{O}_3/\text{Y}_2\text{O}_3/\text{Si}(111)$ templates are promising for future optoelectronic applications.

N-rich regime

The structural and optical properties of μm -thick GaN films deposited under N-rich conditions were investigated for comparison. GaN samples grown in the N-rich regime are characterized by closely-packed nanocolumns/nanowires. For these deposition conditions, the growth proceeds mostly in the vertical direction rather than laterally. Hence, the GaN columns are only 50 nm-wide and μm -high. The nanocolumns are single crystalline with the (0001) vertical growth orientation on $\text{Sc}_2\text{O}_3(111)/\text{Y}_2\text{O}_3(111)/\text{Si}(111)$ templates. The in-plane alignment of the heterostructure is exactly the same as for the structures grown in the Ga-rich regime. Furthermore, N-rich conditions result in a higher amount of threading screw and edge dislocations (of about 10^{11} cm^{-2}) as well as a higher density of stacking fault defects. This is reflected in the optical parameters of the GaN films. 10K PL spectra exhibit a broad defect-related YL and exciton bound to structural defects transitions.

Post-deposition treatments and cracking

The structural quality of the GaN films deposited under Ga-rich as well as N-rich regimes can be improved by annealing. However, the annealing temperature can not be higher than 900°C . Up to this temperature all interfaces remain stable and neither Si nor O diffuse into the GaN layer (nor Ga into the Si) during the annealing process. Application of higher substrate temperatures (e.g. during standard MOCVD GaN growth) results in the decomposition of the oxide buffer and uncontrolled diffusion of elements in the heterostructure (doping) (Fig. 4.2 stage 5.).

In addition, GaN films thicker than $1.2 \mu\text{m}$ exhibit dense cracking which is caused by a large tensile strain existing in the GaN material (Fig. 4.2 stage 4.). This strain is mainly attributed to thermal mismatch between GaN and Si and probably to the tensile strain introduced by island coalescence.¹⁷⁴ As the GaN nucleation islands are found to be fully relaxed before coalescence, lattice mismatch is believed to be not the origin of this biaxial tensile strain. Therefore, it is concluded that the $\text{Sc}_2\text{O}_3/\text{Y}_2\text{O}_3$ buffer plays a lattice match mediator role (lattice mismatch between GaN and Si (17%) is gradually re-

duced to $\sim 8\%$ (GaN/Sc₂O₃) and acts as a barrier against impurity diffusion but does not yet solve the tensile strain problem in the GaN heterostructure.

4.2 Outlook

For the fabrication of GaN-based devices on MBE grown GaN/Sc₂O₃/Y₂O₃/Si(111) templates, the following layer characteristics have to be achieved:

- GaN films should be deposited under Ga-rich conditions. Only for these growth parameters, closed and smooth layers can be obtained.
- Threading dislocation density must be reduced to the level of 10^9 cm⁻² and lower.
- Stacking fault defects and inversion domains have to be completely eliminated.
- Strain engineering approaches must be developed to achieve crack-free μm -thick GaN layers.

To satisfy the above requirements, further optimization concerning the growth of GaN layer must be performed. The next sections outline possible strategies which will be applied to improve the quality of GaN on Sc₂O₃/Y₂O₃/Si(111) substrates.

4.2.1 Next MBE experiments

GaN nucleation

Lattice mismatch between GaN and the buffer layer has a huge impact on the layer morphology (VW or SK mode) and the amount of structural defects. In highly mismatched epitaxy, the growth occurs by the formation of 3D islands. By controlling the GaN growth parameters (substrate temperature, III/V ratio, growth rate) the shape of the islands and the coalescence time can be tuned. The avoidance of large islands and hence fast islands coalescence dramatically improves the GaN surface smoothness and results in lower defect density such as dislocations and pits.^{175,173,52,53,54} To obtain fast coalescence, low temperature (LT) GaN nucleation layer can be used before high temperature deposition process. It was shown that, the temperature increase (from LT to the final deposition point) leads to coalescence of the nucleation layer into

continuous film.¹⁷⁶ In addition, the annealing process may cause reduction of cubic GaN inclusions, which are known to be embedded in the hexagonal matrix near the GaN/Sc₂O₃ interface. Such transformation, from cubic into hexagonal phase upon annealing, was already observed in GaN/Al₂O₃ system.^{177, 178, 179}

One could also consider the use of an additional buffer layer between GaN and Sc₂O₃ to further reduce the lattice mismatch. This may be crucial in order to obtain 2D films by improved GaN wetting behavior on the buffer template.

Reduction of threading dislocation density

The dislocation density in the 2D films can be decreased by applying porous SiN_x or ScN interlayers for defect filtering. Usually, SiN_x interlayer is deposited on an already existing GaN template and it causes inhomogeneous nucleation and lateral growth of the overgrowing GaN film. Such an interlayer effectively blocks a majority of threading dislocations from propagating vertically through the film leading to an order of magnitude reduction in the dislocation density in the top GaN layer.

GaN layer cracking

μm-thick GaN layers deposited on Sc₂O₃/Y₂O₃/Si(111) heterostructures exhibit dense cracking due to large tensile strain. These characteristic "mud cracking" patterns are due to the relaxation of biaxial tensile strain in the GaN films. This tensile strain can be reduced by applying a buffer layer which has a lattice constant smaller than GaN (e.g. AlN) so that the initial GaN grows under a certain compressive strain. An alternative approach to stress releasing is the engineering of the Si wafer. Concave wafer bowing (Fig. 4.3 a)) is characteristic for the tensile strained (e.g. Sc₂O₃ or GaN on Si) layers and convex (Fig. 4.3 b)) for the compressive strained (e.g. Pr₂O₃ on Si). Here, the critical issue is the thickness of the epifilm grown on Si.⁸ Convex wafer bow may be used as a template for GaN growth.¹⁸⁰ During GaN deposition on e.g. Pr₂O₃/Si(111), wafer curvature will decrease and for a characteristic GaN layer thickness it will change the direction from convex to planar (Fig. 4.3 c)). In this way, this technique allows theoretically to achieve thicker GaN layers without cracks in comparison to the standard approach. However, the application of a buffer layer which has a bigger lattice constant than Si results in

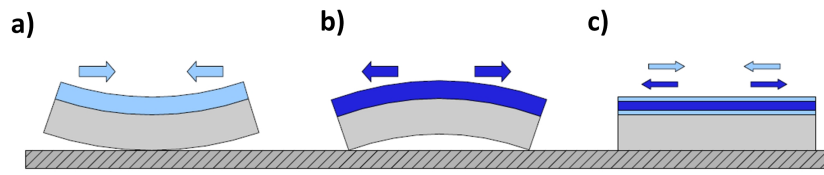


Figure 4.3: a) Concave and b) convex wafer bowing. c) Flat GaN films (curvature=0) may be achieved by application of convex bow templates.

an increase in the lattice mismatch between GaN and the buffer film. This may lead to the formation of a higher amount of dislocations in the GaN layer. Another method to obtain convex wafer bow is to use coating materials whose lattice constant is smaller than that of Si (or whose TEC is bigger than that of Si) on the back side of the wafer.

GaN layer polarity

GaN films grown on $\text{Sc}_2\text{O}_3/\text{Y}_2\text{O}_3/\text{Si}(111)$ templates are dominantly N-polar. N-polar layers usually show lower structural, optical and electrical quality in comparison with Ga-polar layers. In addition, films of N-polarity tend to exhibit higher concentration of inversion domains (in this case Ga-polar inclusions). Such structural defects are also observed in the $\text{GaN}/\text{Sc}_2\text{O}_3/\text{Y}_2\text{O}_3/\text{Si}(111)$ system. Mixture of polarity across the wafer leads to increased carrier scattering (reduced 2D electron gas mobility in HEMT) due to flipping of the polarization field. Therefore, the majority of GaN-based devices is built on Ga-polar films.

In order to achieve Ga-polar GaN films on $\text{Sc}_2\text{O}_3/\text{Y}_2\text{O}_3/\text{Si}(111)$ substrates, the following optimization paths could be applied:

- nitridation of the Sc_2O_3 surface. This method was already successfully used in the epitaxy of GaN on Al_2O_3 substrates^{177, 160, 149}
- deposition of few monolayers of Al on Sc_2O_3 buffer followed by the exposure to nitrogen plasma. In this way, a thin AlN seed layer terminated with N atoms is formed. This should enable nucleation of a Ga-polar GaN layer⁹⁷
- insertion of metal layers e.g. Al or Mg during MBE GaN growth. The inversion from the N-polar to the Ga-polar layer is achieved due to the

fact that at the GaN/Mg/GaN interface the Ga-N-Mg-N-Ga stacking sequence is obtained^{181,182,183}

4.2.2 Future MOCVD experiments

Industrial applications will require deposition of GaN by MOCVD techniques which are widely applied in mass production of GaN-based devices. In this respect, GaN/Sc₂O₃/Y₂O₃/Si(111) heterostructures could be used for example as templates for MOCVD GaN overgrowth. First growth experiments in this direction have been already performed in a collaboration with Wrocław University of Technology. These experiments were focused on the MOCVD GaN growth on 100 nm-thick MBE GaN layers deposited on 50 nm-thick Sc₂O₃/Y₂O₃/oxide buffers. Standard MOCVD GaN growth processes with substrate temperature well above 1000°C were used. At such high temperatures the Sc₂O₃/Y₂O₃/buffer starts to decompose and does not protect GaN against Si diffusion anymore, resulting in a local uncontrolled doping. The locally damaged oxide buffer also does not inhibit Ga diffusion into the Si substrate, resulting in interface reactions. This leads to a deterioration of the MOCVD GaN layers as shown in Fig. 4.4 a). Black spots visible in the plain-view SEM image (Fig. 4.4 a)) are identified as the etched parts of the GaN film. The etching extends from the Si substrate reaching the surface of the GaN film (Fig. 4.4 b)). As indicated by EDX (Fig. 4.4 c)), the reason of the etching is the diffusion of Ga through the oxide buffer into the Si substrate. Despite these local damages, the GaN layer formed between the etched regions is closed and smooth (Fig. 4.4 d)). The estimated threading screw dislocation density is on the order of 10¹⁰ cm⁻². To avoid the decomposition of the oxide buffer, the MOCVD process needs to be optimized. Furthermore, in order to avoid Ga reaction with the Si, also thicker oxide buffer layer can be used.

It is noted that a patent is currently filed by IHP and Siltronic to achieve epitaxial oxides in Si(111) by MOCVD. With such a breakthrough result, a full GaN/oxide/Si(111) heterostructure could be grown by MOCVD.

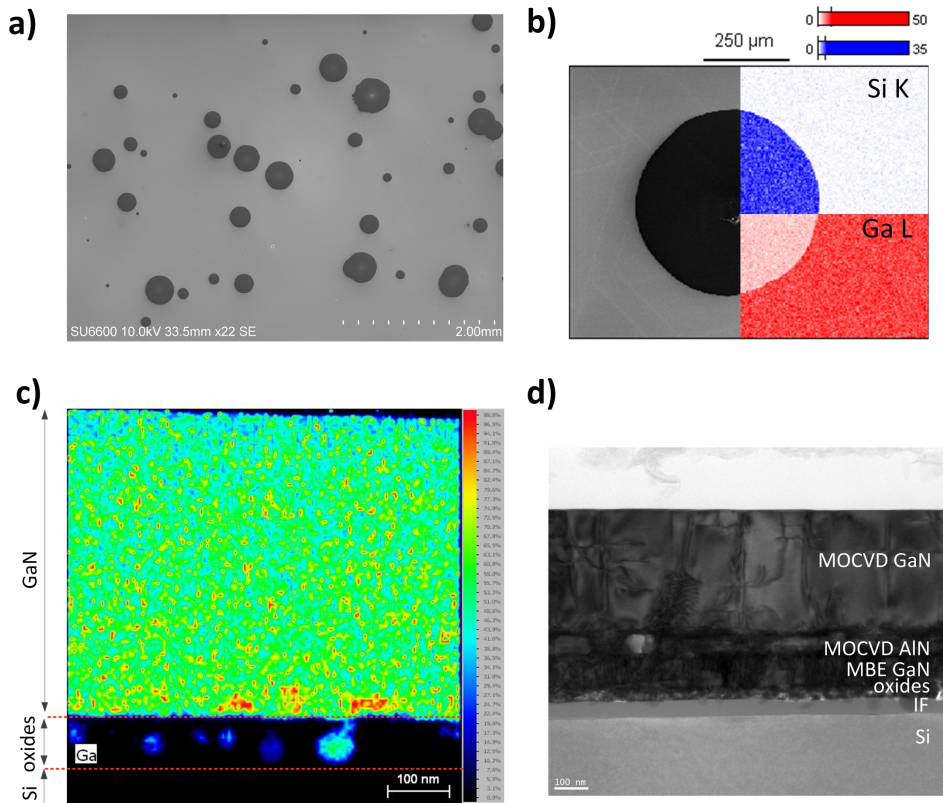


Figure 4.4: a) Plane-view SEM image of the MOCVD GaN layer grown on MBE GaN/Sc₂O₃/Y₂O₃/Si(111) templates. Black points are identified as destroyed parts of the GaN film. b) EDX measurements reveal that the layer is completely damaged up to the Si substrate c) Layer damage may be caused by the reaction of Ga with Si (etching). During high-temperature MOCVD process, the oxide buffer starts to decompose and therefore Ga diffuses to the oxide/Si interface. Locally, a high concentration of Ga is detected by EDX in the oxide buffer d) TEM cross section image of the MOCVD GaN/MBE GaN/Sc₂O₃/Y₂O₃/Si(111) heterostructure. GaN film between destroyed parts is closed and smooth. *Images courtesy of K. Idykiewicz and Prof. R. Paszkiewicz (WUT) and A.M. Schubert (IHP).*

Chapter 5

Scientific visibility

5.1 Publications in peer-reviewed journals

1. **L. Tarnawska**, J. Dabrowski, P. Storck and T. Schroeder, *Interface science of virtual GaN substrates on Si(111) via Sc₂O₃/Y₂O₃ buffer: Experiment and Theory*, Phys. Rev. B **to be submitted**
2. **L. Tarnawska**, P. Zaumseil, M. A. Schubert, S. Okur, U. Ozgur, H. Morkoc, R. Paszkiewicz, P. Storck, T. Schroeder, *Structural and optical quality of GaN grown on Sc₂O₃/Y₂O₃/Si(111)*, J. Appl. Phys. 111, (2012), 073509
3. **L. Tarnawska**, A. Giussani, P. Zaumseil, M. A. Schubert, R. Paszkiewicz, O. Brandt, P. Storck, T. Schroeder, *Single crystalline Sc₂O₃/Y₂O₃ heterostructures as novel engineered buffer approach for GaN integration on Si (111)*, J. Appl. Phys., 108, (2010), 063502
4. P. Zaumseil, **L. Tarnawska**, P. Storck, T. Schroeder, *High-temperature x-ray characterization of GaN epitaxially grown on Sc₂O₃/Y₂O₃/Si(111) heterostructures*, J. Phys. D: Appl. Phys. 44, (2011), 315403
5. F. Sanchez, R. Bachelet, P. de Coux, B. Warot-Fonrose, V. Skumryev, **L. Tarnawska**, P. Zaumseil, T. Schroeder, J. Fontcuberta, *Domain matching epitaxy of ferrimagnetic CoFe₂O₄ thin films on Sc₂O₃/Si(111)*, Appl. Phys. Lett., 99, (2011), 211910

5.2 Presentations at conferences

1. **L. Tarnawska**, P. Zaumseil, P. Storck, T. Schroeder, *Structural and optical quality of GaN films grown on Sc₂O₃/Y₂O₃/Si(111)*, DPG spring meeting, March 2012, Germany
2. **L. Tarnawska**, P. Zaumseil, P. Storck, R. Paszkiewicz, T. Schroeder, *X-ray diffraction study of GaN/Sc₂O₃/Y₂O₃/Si(111) heterostructures*, X-ray school, November 2011, Slovakia
3. **L. Tarnawska**, P. Zaumseil, P. Storck, R. Paszkiewicz, T. Schroeder, *Growth of single crystalline GaN on Si(111) platform via Sc₂O₃/Y₂O₃ buffer*, 7th Integrational Workshop "Advanced Nanaomaterials -synthesis, properties, characterization", October 2011, Poland
4. **L. Tarnawska**, A. Giussani, P. Zaumseil, T. Schroeder, *A bi-layer oxide buffer approach to the integration of single crystalline GaN on Si(111) platform*, 16th European Molecular Beam Epitaxy Workshop, March 2011, France
5. **L. Tarnawska**, P. Zaumseil, M. Kittler, P. Storck, R. Paszkiewicz, T. Schroeder, *Growth of single crystalline GaN on Si(111) platform via Sc₂O₃/Y₂O₃ buffer*, E-MRS spring meeting, January 2011, France
6. **L. Tarnawska**, A. Giussani, A. Schubert, P. Storck, T. Schroeder, *A novel oxide buffer approach for GaN integration on Si(111) platform through single crystalline Sc₂O₃/Y₂O₃ layers*, 16th International Conference on Molecular Beam Epitaxy, September 2010, Germany
7. **L. Tarnawska**, A. Giussani, P. Zaumseil, M. Wosko, R. Paszkiewicz, T. Schroeder, *Synchrotron based X-ray diffraction study of GaN/oxide/Si(111) heterostructures*, German Conference for Research with Synchrotron Radiation, Neutrons and Ion Beam at Large Facilities, February 2010, Germany
8. **L. Tarnawska**, P. Zaumseil, M. Wosko, R. Paszkiewicz, P. Storck, T. Schroeder, *MOVPE growth of GaN layers on Si (111) substrate via Al₂O₃ buffer systems*, III National Conference on Nanotechnology, NANO'2009, July 2009, Poland

Bibliography

- [1] P. PERLIN, C. JAUBERTHIE-CARILLON, J. ITIE, A. S. MIGUEL, I. GRZEGORY, and A. POLIAN, *Phys. Rev. B* **45**, 83 (1992).
- [2] H. MORKOC, *Handbook of nitrides Semiconductors and Devices; Volume 1*, Wiley-VCH, 2008.
- [3] A. SMITH, R. FEENSTRA, D. GREVE, M. SHIN, M. SKOWRONSKI, J. NEUGEBAUER, and J. NORTHRUP, *Appl. Phys. Lett.* **72**, 2114 (1998).
- [4] M. SUMIYA and S. FUKU, *MRS Internet J. Nitride Semicond. Res.* **9**, 1 (2004).
- [5] H. MORKOC, *J. Mat. Sci.: Materials in Electronics* **12**, 677 (2001).
- [6] E. YU, X. DANG, P. ASBECK, S. LAU, and G. SULLIVAN, *J. Vac. Sci. Technol. B* **17**, 1742 (1999).
- [7] A. HANGLEITER, *Phys. Stat. Sol. c* **0**, 1816 (2003).
- [8] T. LI, M. MASTRO, and A. DADGAR, *III-V Compound Semiconductors: integration with Silicon-based microelectronics*, CRC Press, 2011.
- [9] S. STRITE and H. MORKOC, *J. Vac. Sci. B* **10**, 1237 (1992).
- [10] *Physical Properties of Semiconductors*, <http://www.ioffe.ru/SVA/> .
- [11] *Siltronic*, <http://www.siltronic.com/> .
- [12] *Cree*, <http://www.cree.com/> .
- [13] *Monocrystal*, <http://www.monocrystal.com/> .
- [14] *Ammono*, <http://www.ammono.com/> .
- [15] H. MORKOC, *Handbook of nitrides Semiconductors and Devices; Volume 3*, Wiley-VCH, 2008.

- [16] P. SCHLOTTER, J. BAUR, C. HIELSCHER, M. KUNZER, H. OBLOH, R. SCHMIDT, and J. SCHNEIDER, *Material Science and Engineering: B* **59**, 390 (1999).
- [17] M. MASTRO, N. B. R. HOLM, C. EDDY, D. GASKILL, R. HENRY, and M. TWIGG, *Appl. Phys. Lett.* **87**, 241103 (2005).
- [18] F. NATALI, D. BYRNE, A. DUSSAIGNE, N. GRANDJEAN, and J. MASSIES, *Appl. Phys. Lett.* **82**, 499 (2003).
- [19] *Translucent*, <http://www.translucentinc.com/>.
- [20] *Osram Opto Semiconductors*, <http://www.osram-os.com/>.
- [21] G. HELD, *Introduction to Light Emitting Diode Technology and Applications*, CRC Press, 2009.
- [22] I. ICHIMURA, F. MAEDA, K. OSATO, K. YAMAMOTO, and Y. KASAMI, *Jpn. J. Appl. Phys.* **39**, 937 (2000).
- [23] K. SCHEP, B. STEK, R. VAN WOUDEBERG, M. BLUM, S. KOBAYASHI, T. NARAHARA, T. YAMAGAMI, and H. OGAWA, *Jpn. J. Appl. Phys.* **40**, 1813 (2001).
- [24] *Sony*, <http://www.sony.net/>.
- [25] P. RUTERAN, M. ALBRECHT, J. NEUGEBAUER, F. OMNES, and E. MONROY, *Nitride Semiconductors: Handbook on Material and Devices*, Wiley, 2006.
- [26] E. MONROY, E. MUNOZ, F. SANCHEZ, F. CALLE, E. CALLEJA, B. BEAUMONT, P. GIBART, J. MUNOZ, and F. CUSSO, *Smicond. Sci. Technol.* **13**, 1042 (1998).
- [27] E. MONROY, M. HAMILTON, D. WALKER, P. KUNG, F. SANCHEZ, and M. RAZEGHI, *Appl. Phys. Lett.* **74**, 1171 (1999).
- [28] G. PARISH, S. KELLER, P. KOZODOY, J. IBBETSON, H. MARCHAND, P. FINI, S. FLEISCHER, S. DENBAARS, and U. MISHRA, *Appl. Phys. Lett.* **75**, 247 (1999).
- [29] C. CHEN, S. CHANG, Y. SU, G. CHI, J. CHI, C. CHANG, J. SHEU, and J. CHEN, *IEEE Photonics Technology Letters* **13**, 848 (2001).

- [30] Q. CHEN, J. YANG, A. OSINSKY, S. GANGOPADHYAY, B. LIM, and M. ANWAR, *Appl. Phys. Lett.* **70**, 2277 (1997).
- [31] O. AMBACHER, *J. Phys. D: Appl. Phys.* **31**, 2653 (1998).
- [32] H. MORKOC, R. CINGOLANI, and B. GIL, *Solid-State Electronics* **43**, 1753 (1999).
- [33] C. ELSASS, I. SMORCHKOVA, B. HEYING, E. HAUS, P. FINI, K. MARANOWSKI, J. IBBETSON, S. DENBAARS, U. MISHRA, and J. SPECK, *App. Phys. Lett.* **74**, 3528 (1999).
- [34] D. LOOK, *Electrical Characterization of GaAs Materials and Devices, Design and Measurement in Electronic Engineering*, Wiley, 1989.
- [35] R. QUAY, *Gallium Nitride Electronics*, Springer, 2008.
- [36] X. XU, V. JINDAL, F. SHAHEDIPOUR-SANDVIK, M. BERGKVIST, and N. CADY, *App. Surface Science* **255**, 5905 (2009).
- [37] I. CIMALLA, F. WILL, K. TONISCH, V. LEBEDEV, G. KITTLER, and M. G. ABD O. AMBACHER, *Sensors and Actuators B: Chemical* **123**, 740 (2007).
- [38] S. ARULKUMARAN, T. EGAWA, H. ISHIKAWA, and T. JIMBO, *Appl. Phys. Lett.* **81**, 3073 (2002).
- [39] Y. CORDIER, F. SEMOND, P. LORENZINI, N. GRANDJEAN, N. VALLAS, B. DESSERTENE, S. CASSETTE, and S. DELAGE, *Phys. Stat. Sol.* **1**, 61 (2002).
- [40] J. BROWN, R. BORGES, E. PINER, A. VESCAN, S. SINGHAL, and R. THERRIEN, *Solid State Electronics* **46**, 1535 (2002).
- [41] H. SUN, A. ALT, H. BENEDICKTER, C. BOLOGNESI, E. FELTINI, J. CARLIN, M. GONSCHOREK, and N. GRANDJEAN, *Appl. Phys. Express* **3**, 094101 (2010).
- [42] D. MARTI, C. BOLOGNESI, Y. CORDIER, M. CHMIELOWSKA, and M. RAMDANI, *App. Phys. Express* **4**, 064105 (2011).
- [43] J. CHUNG, J. LEE, E. PINER, and T. PALACIOS, *IEEE Electron Device Lett.* **30**, 1015 (2009).

- [44] S. POROWSKI, *MRS Interner J. Nitride Semicond. Res.* **4S1**, G1.3 (1999).
- [45] I. GRZEGORY, *J. Phys.: Condens. Matter* **13**, 6875 (2001).
- [46] H. YAMANE, M. SHIMADA, T. SEKIGUCHI, and F. DISALVO, *J. Cryst. Growth* **186**, 8 (1998).
- [47] M. YANO, M. OKAMATO, Y. YAP, and M. YOSHIMURA, *Jpn. J. appl. Phys.* **38**, L1121 (1999).
- [48] H. YAMANE, T. KAJIWARA, T. SEKIGUCHI, and M. SHIMADA, *Jpn. J. Appl. Phys.* **38**, L1121 (1999).
- [49] R. DWILINSKI, R. DORADZINSKI, J. GARCZYNSKI, L. SIERZPUTOWSKI, A. PUCHALSKI, Y. KANBARA, K. YAGI, H. MINAKUCHI, and H. HAYASHI, *J. Cryst. Growth* **311**, 3015 (2009).
- [50] T. HASHIMOTO, F. WU, J. SPECK, and S. NAKAMURA, *Nature Materials* **6**, 568 (2007).
- [51] *ieee spectrum*, <http://www.spectrum.ieee.org/semiconductors/materials/the-worlds-best-gallium-nitride/>.
- [52] V. NARAYANAN, K. LORENZ, W. KIM, and S. MAHAJAN, *Appl. Phys. Lett.* **78**, 1544 (2001).
- [53] S. KELLER, B. KELLER, Y. WU, B. HEYING, D. KAPOLNEK, J. SPECK, U. MISHRA, and S. DENBAARS, *Appl. Phys. Lett.* **68**, 1525 (1996).
- [54] X. WU, D. KAPOLNEK, E. TARSA, B. HEYING, S. KELLER, B. KELLER, U. MISHRA, S. DENBAARS, and J. SPECK, *Appl. Phys. Lett.* **68**, 1371 (1996).
- [55] S. TANAKA, R. S. KERN, and R. DAVIS, *Appl. Phys. Lett.* **66**, 37 (1995).
- [56] B. SVERDLOV, G. MARTIN, H. MORKOC, and D. SMITH, *Appl. Phys. Lett.* **67**, 2063 (1995).
- [57] Y. HONDA, M. OKANO, M. YAMAGUCHI, and N. SAWAKI, *Phys. Stat. Sol. C* **2**, 2125 (2005).

- [58] J. LIANG, S. HONG, N. KOUKLIN, R. BERESFORD, and J. XU, *Appl. Phys. Lett.* **83**, 1752 (2003).
- [59] F. SHIMURA, *Semiconductor Silicon Crystal Technology*, Academic Press, 1989.
- [60] A. KROST and A. DADGAR, *Materials Science and Engineering B* **93**, 77 (2002).
- [61] A. DADGAR, M. POSCHENRIEDER, J. BLASING, O. CONTREEAS, M. KUNZE, J. CHRISTEN, E. KOHN, and A. KROST, *J. Cryst. Growth* **248**, 556 (2003).
- [62] J. AYERS, *Heteroepitaxy of Semiconductors: theory, growth and characterization*, CRC Press, 2007.
- [63] H. LIAW, R. VENUGOPAL, J. WAN, R. DOYLE, P. FEJES, and M. MELLOCH, *Solid-State Electronics* **44**, 685 (2000).
- [64] M. SOBANSKA, K. KLOSEK, Z. ZYTKIEWICZ, J. BORYSIUK, B. WITKOWSKI, E. LUSAKOWA, A. RESZKA, and R. JAKIEL, *Cryst. Res. Technol.* **47**, 307 (2012).
- [65] A. STRITTMATTER, D. BIMBERG, A. KROST, J. BLASING, and P. VEIT, *J. Cryst. Growth* **211**, 293 (2000).
- [66] A. STRITTMATTER, A. KROST, V. TURCK, M. STRASSBURG, D. B. ND J. BLASING, T. HEMPEL, J. CHRISTEN, B. NEUBAUER, D. GERTHSEN, and B. MEYER, *Materials Science and Engineering B* **59**, 29 (1999).
- [67] R. ARMITAGE, Q. YANG, H. FEICK, J. GEBAUER, E. WEBER, S. SHINKAI, and K. SASAKI, *Appl. Phys. Lett.* **81**, 1450 (2002).
- [68] M. MORAM, Y. ZHANG, M. KAPPERS, Z. BARBER, and C. HUMPHREYS, *Appl. Phys. Lett.* **91**, 152101 (2007).
- [69] R. PASZKIEWICZ, B. PASZKIEWICZ, M. WOSKO, A. SZYSZKA, L. MARCINIAK, J. PRAMOWSKA, W. MACHERZYSKI, M. TLACZALA, J. KOVAC, I. NOVOTNY, and D. HASKO, *J. Cryst. Growth* **310**, 4891 (2008).
- [70] V. LAZAROV, J. ZIMMERMAN, S. CHEUNG, L. LI, M. WEINERT, and M. GAJDARDZISKA-JOSIFOVSKA, *PRL* **94**, 216101 (2005).

- [71] A. WAKAHARA, H. OISHI, H. OKADA, A. YOSHIDA, Y. KOJI, and M. ISHIDA, *J. Cryst. Growth* **236**, 21 (2002).
- [72] C. MERCKLING, M. EL-KAZZI, G. SAINT-GIRONS, G. HOLLINGER, L. LARGEAU, G. PATRIARCHE, V. FAVRE-NICOLIN, and O. MARTY, *Appl. Phys. Lett.* **102**, 024101 (2007).
- [73] B. MAN, C. YANG, H. ZHUANG, M. LIU, X. WEI, H. ZHU, and C. XUE, *J. Appl. Phys.* **101**, 093519 (2007).
- [74] F. HAMDANI, A. BOTCHKAREV, W. KIM, H. MORKOC, M. YEADON, J. GIBSON, D. SMITH, D. LOOK, C. LITTON, and P. HEMENGER, *Appl. Phys. Lett.* **70**, 467 (1996).
- [75] H. LAHRECHE, P. VENNEGUES, O. TOTTEREAU, M. LAUGT, P. LORENZINI, M. LEROUX, B. BEAUMONT, and P. GIBART, *J. Cryst. Growth* **217**, 13 (2000).
- [76] N. BARON, Y. CORDIER, S. CHENOT, P. VENNEGUES, O. TOTTEREAU, M. LEROUX, F. SEMOND, and J. MASSIES, *J. Appl. Phys.* **105**, 033701 (2009).
- [77] E. FELTIN, B. BEAUMONT, M. LAUGT, P. DE MIERRY, P. VENNEGUES, H. LAHRECHE, M. LEROUX, and P. GIBART, *Appl. Phys. Lett.* **79**, 3230 (2001).
- [78] S. RAGHAVANA, X. WENG, E. DICKEY, and J. REDWING, *Appl. Phys. Lett.* **88**, 041904 (2006).
- [79] A. ABLE, W. WEGSCHEIDER, K. ENGL, and J. ZWECK, *J. Cryst. Growth* **276**, 415 (2005).
- [80] A. KROST, A. DADGAR, G. STRASSBURGER, and R. CLOS, *Phys. Stat. Solidi a* **200**, 26 (2003).
- [81] Y. HONDA, Y. KUROIWA, M. YAMAGUCHI, and N. SAWAKI, *Appl. Phys. Lett.* **80**, 222 (2002).
- [82] S. ZAMIR, B. MEYLER, and J. SALZMAN, *J. Cryst. Growth* **230**, 341 (2001).
- [83] Y. HONDA, Y. KAWAGUCHI, Y. OHTAKES, S. TANAKA, M. YAMAGUCHI, and N. SAWAKI, *J. Cryst. Growth* **230**, 346 (2001).

- [84] K. ZANG, Y. WANG, S. CHUA, and L. WANG, *Appl. Phys. Lett.* **87**, 193106 (2005).
- [85] N. KOBAYASHI, J. KOBAYASHI, X. ZHANG, P. DAPKUS, and D. RICH, *Appl. Phys. Lett.* **74**, 2836 (1999).
- [86] T. RIEMANN, T. HEMPEL, J. CHRISTEN, P. VEIT, R. CLOS, A. DADGAR, and A. KROST, *J. Appl. Phys.* **99**, 123518 (2006).
- [87] K. HIRAMATSU, K. NISHIYAMA, M. ONISHI, H. MIZUTANI, M. NARUKAWA, A. MOTOGAITO, H. MIYAKE, Y. IYEBIKA, and T. MAEDA, *J. Cryst. Growth* **221**, 316 (2000).
- [88] S. TANAKA, Y. HONDA, and N. SAWAKI, *Appl. Phys. Lett.* **79**, 955 (2001).
- [89] A. STRITTMATTER, S. RODT, L. REISSMANN, D. BIMBEG, H. SCHROEDER, E. OBERMEIER, T. RIEMANN, J. CHRISTEN, and A. KROST, *Appl. Phys. Lett.* **78**, 727 (2001).
- [90] T. LI, S. HSU, D. TWEET, and J. MAA, *U.S patent application 20080296616* (2008).
- [91] S. HAFFOUZ, A. GRZEGORCZYK, P. HAGEMAN, P. VENNEGUES, E. VAN DER DRIFT, and P. LARSEN, *J. Cryst. Growth* **248**, 568 (2003).
- [92] B. KIM, K. LEE, S. JANG, J. JHIN, S. LEE, J. BAEK, Y. YU, J. LEE, and D. BYUN, *Chem. Vap. Deposition* **16**, 80 (2010).
- [93] D. KIM, *J. Mater. Sci.: Materials in Electronics* **19**, 471 (2008).
- [94] R. DAVIS, T. GEHRKE, K. LINTHICUM, T. ZHELEVA, E. PREBLE, P. RAJAGOPAL, C. ZORMAN, and M. MEHREGANY, *J. Cryst. Growth* **225**, 134 (2001).
- [95] T. SCHROEDER, A. GIUSSANI, J. DABROWSKI, P. ZAUMSEIL, H.-J. MÜSSIG, O. SEIFARTH, and P. STORCK, *Phys. Status Solidi C* **6**, 653 (2009).
- [96] A. GIUSSANI, P. RODENBACH, P. ZAUMSEIL, J. DABROWSKI, R. KURPS, G. WEIDNER, H.-J. MÜSSIG, P. STORCK, J. WOLLSCHLÄGER, and T. SCHROEDER, *J. Appl. Phys.* **105**, 033512 (2009).

- [97] W. LEE, Y. LEE, J. KWO, C. HSU, C. LEE, S. WU, H. NG, and M. HONG, *J. Cryst. Growth* **311**, 2006 (2009).
- [98] M. HONG, J. KWO, S. CHU, J. MANNAERTS, A. KORTAN, H. NG, A. CHO, and K. ANSELM, *J. Vac. Sci. Technol. B* **20**, 1274 (2002).
- [99] T. SCHROEDER, P. STORCK, and H.-J. MUESSIG, United States Patent, US 7.785.706 B2, 2010.
- [100] V. AVRUTIN, N. IZYUMSKAYA, U. ÖZGÜR, D. SILVERSMITH, and H. MORKOC, *Proceedings of the IEEE* **98**, 1288 (2010).
- [101] M. CURIE, S. SAMAVEDAM, T. LANGDO, C. LEITZ, and E. FITZGERALD, *Appl. Phys. Lett.* **72**, 1718 (1998).
- [102] C. BORSCHEL, C. RONNING, H. HOFSSÄSS, A. GIUSSANI, P. ZAUMSEIL, C. WENGER, P. STORCK, and T. SCHROEDER, *J. Vac. Sci. Technol. B* **27**, 305 (2009).
- [103] H. FUKUMOTO, T. IMURA, and Y. OSAKA, *Appl. Phys. Lett.* **55**, 360 (1989).
- [104] M. HUNTER, M. REED, N. EL-MASRY, J. ROBERTS, and S. BEDAIR, *Appl. Phys. Lett.* **76**, 1935 (2000).
- [105] M. CHO, D. KO, Y. CHOI, I. LYO, and K. JEONG, *Appl. Phys. Lett.* **89**, 1647 (2001).
- [106] W. KERN, *Handbook of Semiconductor Wafer Cleaning Technology*, Noyes Publications Park Ridge NJ, 1993.
- [107] I. MARKOV, *Crystal Growth for Beginners*, World Scientific, 2003.
- [108] B. VANMIL, H. GUO, L. HOLBERT, K. LEE, T. MYERS, T. LIU, and D. KORAKAKIS, *J. Vac. Sci. Technol. B* **22**, 2149 (2003).
- [109] E. TARSA, B. HEYING, X. WU, P. FINI, S. DENBAARS, and J. SPECK, *J. Appl. Phys.* **82**, 5472 (2009).
- [110] B. HEYING, I. SMORCHKOVA, C. POBLEZ, C. ELSASS, P. FINI, S. D. BAARS, U. MISHRA, and J. SPECK, *Appl. Phys. Lett.* **77**, 2885 (2000).
- [111] B. HEYING, R. AVERBECK, L. CHEN, E. HAUS, H. RIECHERT, and J. SPECK, *J. Appl. Phys.* **88**, 1855 (2000).

- [112] S. FERNANDEZ, G. KOBLMULLER, E. CALLEJA, and J. SPECK, *J. Appl. Phys* **104**, 033541 (2008).
- [113] S. FERNANDEZ-GARRIDO, J. GRANDAL, E. CALLEJA, M. SANCHEZ-GARCIA, and D. LOPEZ-ROMERO, *J. Appl. Phys.* **106**, 126102 (2009).
- [114] J. NORTHRUP, J. NEUGEBAUER, R. FEENSTRA, and A. SMITH, *Phys. Rev. B* **61**, 9932 (2000).
- [115] G. KOBLMULLER, R. AVERBECK, H. RIECHERT, and P. PONGRATZ, *Phys. Rev. B* **69**, 035325 (2004).
- [116] G. MULA, C. ADELMANN, S. MOEHL, J. OULLIER, and B. DAUDIN, *Phys. Rev. B* **64**, 195406 (2001).
- [117] B. WARREN, *X-ray Diffraction*, Dover Publications, 1990.
- [118] M. BIRKHOLZ, *Thin Film Analysis by X-ray Scattering*, Wiley-VCH, 2006.
- [119] *European Synchrotron Radiation Facility*, <http://www.esrf.eu/>.
- [120] G. WILLIAMSON and W. HALL, *Acta Metall.* **1**, 22 (1953).
- [121] P. ZAUMSEIL, *J. Phys. D: Appl. Phys.* **41**, 135308 (2008).
- [122] P. ZAUMSEIL, A. GIUSSANI, and T. SCHROEDER, *Powder Diffraction* **25**, 92 (2010).
- [123] J. ALS-NIELSEN and D. MCMORROW, *Elements of Modern X-ray Physics*, Wiley, 2001.
- [124] P. ZAUMSEIL, Rocking and Reflectivity Simulation Software (RCRef-SimW) (IHP, Frankfurt (Oder)).
- [125] A. ICHIMIYA and P. COHEN, *Reflection High Energy Electron Diffraction*, Cambridge University Press, 2004.
- [126] W. BRAUN, *Applied RHEED: Reflection High-Energy Electron Diffraction During Crystal Growth*, Springer, 1999.
- [127] J. MAHAN, K. GEIB, G. ROBINSON, and R. LONG, *J. Vac. Sci. Technol. A* **8**, 3692 (1990).

- [128] M. DABROWSKA-SZATA, *Mat. Chem. and Phys.* **81**, 257 (2003).
- [129] J. VICKERMAN and I. GLIMORE, *Surface Analysis: The Principal Techniques*, Wiley, 2009.
- [130] T. ALFORD, L. FELDMAN, and J. MAYER, *Fundamentals of Nanoscale Film Analysis*, Springer, 2007.
- [131] J. WATTS and J. WOLSTENHOLME, *An Introduction to Surface Analysis by XPS and AES*, Wiley, 2003.
- [132] A. EINSTEIN, *Ann. Phys.* **17**, 132 (1905).
- [133] S. TANUMA, C. POWELL, and D. PENN, *Surf. Interface Anal.* **17**, 927 (2000).
- [134] J. GOLDSTEIN, D. NEWBURY, D. JOY, C. LYMAN, P. ECHLIN, E. LIFSHIN, L. SAWYER, and M. HEALY, *Scanning Electron Microscopy and X-ray Microanalysis*, Springer, 2002.
- [135] D. WILLIAM and B. CARTER, *Transmission Electron Microscopy: A Textbook for Materials Science*, Plenum Press, 1996.
- [136] G. GILLILAND, *Materials Science and Engineering: Reports* **18**, 99 (1997).
- [137] M. RESHCHIKOV and H. MORKOC, *Appl. Phys. Rev.* **97**, 061301 (2005).
- [138] A. WILKE, J. YANG, J. KIM, O. SEIFARTH, B. DIETRICH, A. GIUSSANI, P. ZAUMSEIL, P. STORCK, and T. SCHROEDER, *Surf. Interface Anal.* **43**, 827 (2010).
- [139] L. TARNAWSKA, P. ZAUMSEIL, M. SCHUBERT, U. O. S. OKUR, H. MORKOÇ, R. PASZKIEWICZ, P. STORCK, and T. SCHROEDER, *J. Appl. Phys.* **111**, 073509 (2012).
- [140] T. SCHROEDER, A. GIUSSANI, H.-J. MSSIG, G. WEIDNER, I. COSTINA, C. WENGER, M. LUKOSIUS, P. STORCK, and P. ZAUMSEIL, *Microelectron. Eng.* **86**, 1615 (2009).
- [141] T. SCHROEDER, P. ZAUMSEIL, O. SEIFARTH, H.-J. MSSIG, P. STORCK, D. GEIGER, H. LICHTER, and J. DABROWSKI, *New J. Phys.* **10**, 113004 (2008).

- [142] P. ZAUMSEIL, A. GIUSSANI, P. STORCK, and T. SCHROEDER, *J. Phys. D: Appl. Phys.* **42**, 215411 (2009).
- [143] U. PIETSCH, V. HOL, and T. BAUMBACH, *High-Resolution X-Ray Scattering*, Springer, 2004.
- [144] M. MORAM and M. VICKERS, *Rep. Prog. Phys.* **72**, 036502 (2009).
- [145] M. MORSE, P. WU, S. CHOI, T. KIM, A. BROWN, M. LOSURDO, and G. BRUNO, *Appl. Surf. Sci.* **253**, 232 (2006).
- [146] V. KAGANER, O. BRANDT, A. TRAMPERT, and K. PLOOG, *Phys. Rev. B.* **72**, 045423 (2005).
- [147] W. LI and A. LI, *J. Cryst. Growth* **227-228**, 415 (2001).
- [148] T. SCHROEDER, A. GIUSSANI, J. DABROWSKI, P. ZAUMSEIL, H. MÜSSIG, O. SEIFARTH, and P. STORCK, *Phys. Status Solidi C* **6**, 653 (2009).
- [149] G. NAMKOONG, W. DOOLITTLE, A. BROWN, M. LOSURDO, P. CAPEZZUTO, and G. BRUNO, *Appl. Phys. Lett.* **91**, 2499 (2002).
- [150] T. SUZUKI, C. HARADA, H. GOTO, T. MINEGISHI, A. SETIAWAN, H. KO, M. W. CHO, and T. YAO, *Appl. Phys. Lett.* **4**, 643 (2004).
- [151] V. IOANNOUS-SOUGLERIDIS, V. CONSTANTOUDIS, M. ALEXE, R. SCHOLZ, G. VELLIANITIS, and A. DIMOULAS, *Thin Solid Films* **468**, 303 (2004).
- [152] M. RESHCHIKOV and H. MORKOÇ, *J. Appl. Phys. Rev.* **97**, 061301 (2005).
- [153] P. ZAUMSEIL, L. TARNAWSKA, P. STORCK, and T. SCHROEDER, *J. Phys. D: Appl. Phys.* **44**, 315403 (2011).
- [154] L. TARNAWSKA, A. GIUSSANI, P. ZAUMSEIL, M. SCHUBERT, R. PASZKIEWICZ, O. BRANDT, P. STORCK, and T. SCHROEDER, *J. Appl. Phys.* **108**, 063502 (2010).
- [155] F. SÚNCHEZ, R. BACHELET, P. DE COUX, B. WAROT-FONROSE, V. SKUMRYEV, L. TARNAWSKA, P. ZAUMSEIL, T. SCHROEDER, and J. FONTCUBERTA, *Appl. Phys. Lett.* **99**, 211910 (2011).

- [156] X. WU, D. KAPOLNEK, E. TARSA, B. HEYING, S. KELLER, B. KELLER, U. MISHRA, S. DENBAARS, and J. SPECK, *Appl. Phys. Lett.* **68**, 1371 (1996).
- [157] A. KUZNETSOV, E. RAKOVA, S. LEE, and P. CHONG, *J. Cryst. Growth* **167**, 458 (1996).
- [158] A. SMITH, R. FEENSTRA, D. GREVE, M. SHIN, M. SKOWRONSKI, J. NEUGEBAUER, and J. NORTHRUP, *Appl. Phys. Lett.* **72**, 2114 (1998).
- [159] J. GIMZEWSKI, D. FABIAN, L. WATSON, and S. AFFROSSMAN, *J. Phys. F: Metal Phys.* **7**, L305 (1997).
- [160] M. LOSURDO, P. CAPEZZUTO, G. BRUNO, G. NAMKOONG, W. DOOLITTLE, and A. BROWN, *J. Appl. Phys.* **91**, 2508 (2002).
- [161] Z. SITAR, L. SMITH, and R. DAVIS, *J. Cryst. Growth* **141**, 11 (1994).
- [162] S. CHEUNG, L. ZHENG, M. XIE, and S. TONG, *Phys. Rev. B* **64**, 033304 (2001).
- [163] Y. CHANG, H. CHIU, Y. LEE, M. HUANG, K. LEE, M. HONG, Y. CHIU, J. KWO, and Y. WANG, *Appl. Phys. Lett.* **90**, 232904 (2007).
- [164] W. PRIYANTHA, G. RADHAKRISHNAN, R. DROOPAD, and M. PASSLACK, *J. Cryst. Growth* **323**, 103 (2011).
- [165] G. MULA, C. ADELMANN, S. MOEHL, J. OULLIER, and B. DAUDIN, *Phys. Rev. B* **64**, 195406 (2001).
- [166] H. TÛTÛNCÛ, S. BAĐCI, G. SRIVASTAVA, A. ALBUDAK, and G. UĐUR, *Phys. Rev. B* **71**, 195309 (2005).
- [167] V. TIMON, S. BRANDS, S. CLARK, and R. ABRAM, *J. Phys.: Condens. Matter* **16**, 531 (2004).
- [168] M. FUCHS, J. D. SILVA, C. STAMPFL, J. NEUGEBAUER, and M. SCHEFFKER, *Phys. Rev. B* **65**, 245212 (2002).
- [169] N. NEWMAN, *J. Cryst. Growth* **178**, 102 (1997).
- [170] J. NORTHRUP, J. NEUGEBAUER, and L. ROMANO, *Phys. Rev. Lett.* **77**, 103 (1996).

- [171] G. NAMKOONG, S. BURNHAM, K. LEE, E. TRYBUS, W. DOOLITTLE, M. LOSURDO, P. CAPEZZUTO, G. BRUNO, B. NEMETH, and J. NAUSE, *Appl. Phys. Lett.* **87**, 184104 (2005).
- [172] L. CHENG, K. ZHOU, Z. ZHANG, G. ZHANG, Z. YANG, and Y. TONG, *Appl. Phys. Lett.* **74**, 661 (1999).
- [173] E. CALLEJA, M. SANCHEZ-GARCIA, F. SANCHEZ, F. CALLE, F. NARANJO, M. MUNOZ, S. MOLINA, A. SANCHEZ, F. PACHECO, and R. GARCIA, *J. Cryst. Growth* **201/202**, 296 (1999).
- [174] S. SEEL and C. THOMPSON, *J. Appl. Phys.* **93**, 9038 (2003).
- [175] J. TERSOFF, A. D. VAN DER GON, and R. TROMP, *Phys. Rev. Lett.* **72**, 266 (1994).
- [176] V. LEBEDEV, K. TONISCH, F. NIEBELSCHUTZ, V. CIMALLA, D. CENGFER, I. CIMALLA, C. MAUDER, O. AMBACHER, F. MORALES, and D. GONZALEZ, *J. Appl. Phys.* **101**, 054906 (2007).
- [177] J. NARAYAN, P. PANT, A. CHUGH, H. CHOI, and J. FAN, *J. Appl. Phys.* **99**, 054313 (2006).
- [178] X. WU, L. BROWN, D. KAPOLNEK, S. KELLER, B. KELLER, S. DENBAARS, and J. SPECK, *J. Appl. Phys.* **80**, 3228 (1996).
- [179] F. PONCE, J. MAJOR, W. PLANO, and D. WELCH, *Appl. Phys. Lett.* **65**, 2302 (1994).
- [180] M. LEBBY, A. CLARK, and G. DING, *Compound Semiconductor Magazine* **18**, 37 (2012).
- [181] V. RAMACHANDRAN, R. FEENSTRA, W. SARNEY, L. SALAMANCA-RIBA, J. NORTHRUP, L. ROMANO, and D. GREVE, *Appl. Phys. Lett.* **75**, 808 (1999).
- [182] N. GRANDJEAN, A. DUSSAIGNE, S. PEZZAGNA, and P. VENNEGUES, *J. Cryst. Growth* **251**, 460 (2003).
- [183] M. WONG, F. WU, J. SPECK, and U. MISHRA, *J. Appl. Phys.* **108**, 123710 (2010).